Chapter 2: Phosphorescent Ir(III) complexes and their aggregation induced emission

This chapter is devoted to the study of phosphorescent Ir(III) complexes and their aggregation induced emission (AIE). The first section includes an extensive introduction to the AIE phenomenon, where several examples of organic molecules exhibiting AIE are discussed to illustrate how this field has evolved during the past years and what are the main controversies in the literature about the proposed mechanisms to explain this phenomenon. Moreover, the introduction of the AIE concept using organic systems is more straightforward than with Ir(III) complexes since population of the triplet manifold is usually negligible for the former. An introduction to the chemistry of Ir(III) complexes and spin-orbit coupling is also given in section 1. The general objectives of this chapter are given in section 2 and remarks on the computational modeling of Ir(III) compounds are made in section 3. These are followed by the discussion of our results in sections 4-8 and general conclusions in section 9.

1. Overview of the aggregation induced emission phenomenon

1.1 Aggregation induced emission

The term aggregation induced emission[1] (AIE) was coined by Professor Ben Zhong Tang and co-workers in 2001. They reported[2] the synthesis of a luminescent silole, namely 1-methyl-1,2,3,4,5-pentaphenylsilole, which presented a remarkable boost in the emission efficiency upon aggregation. This work represented a real breakthrough in the search of strong emitters in aggregated phase, since historically there had been the general belief that luminescence was quenched by concentration[3]. To emphasize the importance of their work, Professor Tang introduced a new term to describe the opposite phenomenon to their discovery, that is aggregation caused quenching[4] (ACQ).

A typical experiment illustrating the opposed ACQ and AIE effects[5] is shown in Figure 2.1. Dilute solutions of the chromophore of interest are prepared in a good organic solvent such as tetrahydrofuran (THF). Molecular aggregation is then prompted upon the addition of a poor solvent, generally water. As it is clear in Figure 2.1, perylene exhibits a strong blue emission in dilute solutions, while the luminescence is quenched when aggregates are formed, thus being a typical example of ACQ. On the other hand, hexaphenylsilole (HPS)

exhibits the opposite behavior, that is, a strong emission is only observed when aggregates are formed (AIE) in solutions with a high water fraction.

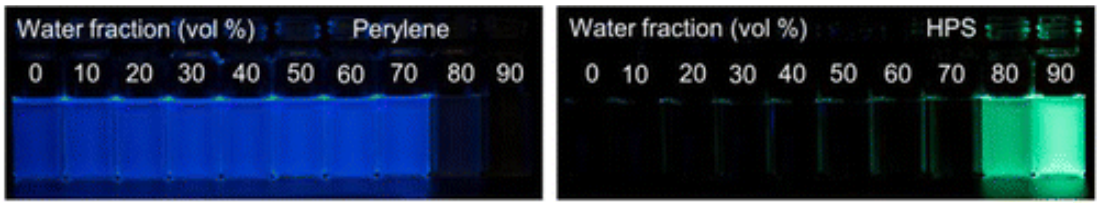

Figure 2.1 Fluorescence photographs of solutions or suspensions of (left) perylene (20 μM) and (right) HPS (20 μM) in THF/water mixtures with different fractions of water (f_w), with perylene and HPS showing typical ACQ and AIE effects, respectively. Taken from reference 5.

The enhancement of the emission intensity is not exclusive of aggregate samples in solution and, in the majority of cases, the same behavior is observed for thin films, crystals or powder samples[6]. Therefore, the AIE phenomenon is extremely suitable for a wide range of applications[5]. In the field of OLEDs for instance, the discovery of strong luminescent materials in the solid state has popularized the design of non-doped OLEDs, in which AIE active materials are used as the emitting-layer[7,8]. Moreover, the dependency of the emission intensity on the environment has lead molecules exhibiting AIE to be proposed as promising candidates for bioimaging[9-11] or chemeosensors[12-14]. In general, materials that are able to change their properties in response to an external stimulus have attracted in recent years a great deal of attention due to their potential applications as sensors[15]. A large variety of materials exhibiting AIE properties have been reported to behave as "smart" or "intelligent" materials since their luminescence properties may change in response to external stimuli or changes in their environment[16,17], such as mechanical forces, temperature, pH, fuming with vapors, photonic irradiation, solvent polarity, electric fields and so on. The interest towards this field is reflected in the number of reported AIE molecules, which has been growing at an exponential rate during the past decade.

Since the first report[2] in 2001, the AIE effect has been observed for a variety of compounds, ranging from purely organic molecules[18,19] to organometallic complexes.[20] Moreover, the structural pattern of these compounds is not unique, with some AIE compounds containing highly flexible parts, while in other cases they exhibit rather rigid structures. In many cases, the observed luminescences do not follow exactly the emission pattern shown in Figure 2.1. Concretely, some AIE compounds might already exhibit a

weak emission in dilute solution, and the intensity may increase gradually along the samples, but not abruptly as shown in Figure 2.1, or even more, the emission color may change gradually from the dilute solution to the case with increased water fractions. The discovery of these related phenomenologies has evolved into different terms connected to the original AIE acronym. Since we feel that the "zoo" of new terminologies and acronyms that have appeared in the literature to designate related phenomena has created some confusion rather than clarification, we will here briefly discuss some of the most used denominations explaining the differences and similitudes with the AIE effect.

As mentioned above, although in the original AIE experiment the molecules were strictly non-emissive in solution, it has been often found that the luminescence of a poorly emitting molecule can be strongly enhanced upon aggregation. To distinguish this behavior from the ideal AIE case, where the chromophores are not emitting at all in dilute solution, the term AIEE[21] (aggregation induced enhanced emission) is employed by some authors. Since most of the early efforts in the development of AIE systems was devoted to organic molecules such as HPS, where the emission is associated with fluorescence, no special distinction was used and the terms AIE and AIEE were used without further specification about the nature of the emitted radiation. With the quest for efficient organic or organometallic phosphorescent materials in the solid state, especially in the field of OLEDs, the term AIPE (aggregation induced phosphorescent emission) has been introduced also in the literature[22] to stress the phosphorescent nature of the emission. In some cases, when a special emphasis on the solid nature of the studied systems is made, the denomination EPESS[23] (enhanced phosphorescence emission in the solid state) is used instead of the more generic AIPE. In the special case that the emission or emission enhancement is observed only in crystalline samples, the terms CIEE[24,25] (crystallization induced emission enhancement) or CIP[26] (crystallization induced phosphorescence enhancement) have also been used to describe these phenomena. It is important to point out that the distinction of the different situations just reviewed is not systematic in the literature and the general AIE term is often used. However, the obvious tendency to label each specific phenomenological case does not seem to be very convenient. The overuse of adjectives describing each situation is very common in the AIE field and, in our opinion, the plethora of existing terms is not justified since, regardless of the specified details of each compound or experimental conditions, they all refer to the same physical phenomenon. It seems to me that, unfortunately, publishing reasons seem to be behind this

abuse of introducing new fancy terminology. To avoid confusion, we will therefore make use only of the more general AIE term throughout this thesis.

1.2 AIE working mechanisms

In this section, we will go through the most fundamental mechanisms that have been proposed to explain the AIE effect of prototypical molecules. Fluorescence quenching had historically been observed for "most aromatic hydrocarbons and their derivatives" in concentrated solutions, as summarized by Birks in his classical monograph *Photophysics of Aromatic Molecules*[27]. Such quenching is linked to the planar structure of typical aromatic molecules, for which excimer formation is favored[28]. Excimers can be understood as an electronically excited dimer that is stabilized by CT interactions (not present in the ground state) between the two constituting monomers when these are close together and adequately orientated for efficient electronic coupling. Non-radiative electron transfer processes are usually associated with the formation and deactivation of excimers. Typically, excimer formation results either in a complete suppression of luminescence or in the appearance of a broad and weak red-shifted band in the photoemission spectrum[29]. Perylene (Figure 2.1, left) is a classical example of excimer formation, and the excimeric emission band has been observed[3] both in concentrated solutions and in the solid state (α- and β-perylene crystals).

The historical use of the *concentration quenching* term referred to quenching of the monomer's emission for a particular class of aromatic molecules, despite excimer emission may arise in some cases. However, this important detail is not usually included in Prof. Tang's interpretation of the ACQ phenomenon, and the term is often used with a broader meaning than just the historical concentration quenching phenomenon. In particular, many scientists working in the AIE field, including Prof. Tang, employ the ACQ term for systems in which the quenching of the luminescence is not necessarily due to excimer formation. Moreover, as it will be discussed below, excimer formation is sometimes given as an explanation to the observed AIE. Thus, the general way in which the ACQ denomination is used in the modern AIE-related literature can certainly be a source of confusion.

Turning back our attention to the working mechanism behind the observed AIE in the prototypical HPS molecule, it is important to highlight its structural differences with

respect to perylene (Figure 2.2). In the HPS molecules a silole core is surrounded by six phenyl rings, attached to it through single C-C or Si-C bonds, allowing a high conformational flexibility and large amplitude molecular motions. In the crystal structure, HPS molecules adopt a propeller-like conformation that prevents π–π stacking interactions between neighboring molecules that could lead to excimer formation, as in the case of perylene. According to Prof. Tang, in diluted solution, the internal rotation of the six phenyl rings around the single-bond axes provide an efficient non-radiative pathway for the excited molecule to decay to the ground state, suppressing its luminescent emission. In the crystal, however, intermolecular C–H···π interactions between adjacent HPS molecules stabilize the crystal packing and restrict the rotational motion of their phenyl rings, blocking the non-radiative relaxation channel while the radiative one remains open, giving rise to a bright photoluminescence. Since a similar behavior is observed for HPS in water/ THF mixtures with high water fractions, one can deduce that similar intermolecular interactions that block non-radiative decay pathways will be present in the aggregates of HPS that form in a poor solvent. Hence, the origin of the AIE in HPS was initially attributed to the restriction of internal rotations[30] (RIR). The RIR mechanism has lead to the successful rational design of new AIE molecules, such as tetraphenylethylene[31] (TPE). In TPE, an ethylene unit is substituted with four highly mobile phenyl rotors, who's restricted rotation in aggregate phases gives rise to AIE.

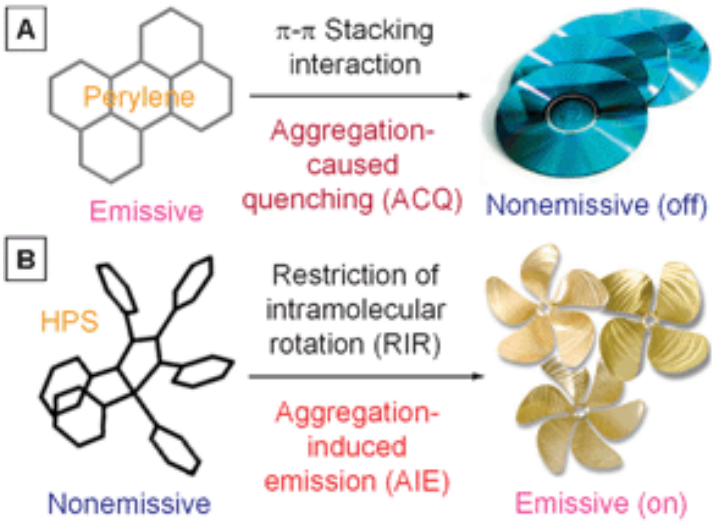

Figure 2.2 (a) Planar chromophores such as perylene tend to aggregate as discs pile up, due to the strong π–π stacking interactions between the aromatic rings, which commonly turn "off" light emission. (b) Non-planar molecules such as HPS behave oppositely, with their light emissions turned "on" by aggregate formation, due to the RIR mechanism. Figure taken from reference 19.

As extensively reviewed[5], different experiments have been designed to support the RIR mechanism[32,33], including changes in the viscosity of the solvent, in the temperature, pressure, or chemical substitution to block all or some of the internal rotations in the molecule. Although most of the results of these experiments were compatible with the RIR hypothesis (like in the HPS and TPE molecules), it was soon observed that AIE was also present in some molecules where the RIR mechanism does not hold as a plausible origin for this phenomenon. This is the case of 10,10′,11,11′-tetrahydro-5,5′-bidibenzo[a,d][7]-annulenylidene (THBA), where all possible internal rotations of phenyl rings are blocked by the formation of covalent links between them[6] (Figure 2.3). The presence in this case of low frequency vibrational modes implying large amplitude motions of the molecular framework led to the proposal of a restriction of internal vibrations[34] (RIV) mechanism, in which the molecular environment in the aggregates imposes a higher structural rigidity blocking the non-radiative decay of the excited states via low frequency modes. Experiments with different molecules and theoretical work,[35-39] mainly by the group of Prof. Shuai, has shown that both the RIR and RIV mechanisms may be present in some cases and that they are just particular versions of a more general mechanism, the restriction of internal motion[5,34] (RIM), in which no differentiation is made on the detailed nature of the low frequency, large amplitude motions that quench the luminescence in solution via internal conversion, but lead to AIE upon aggregation when this non-radiative channel gets blocked by the rigidification of the molecular environment via the establishment of intermolecular interactions.

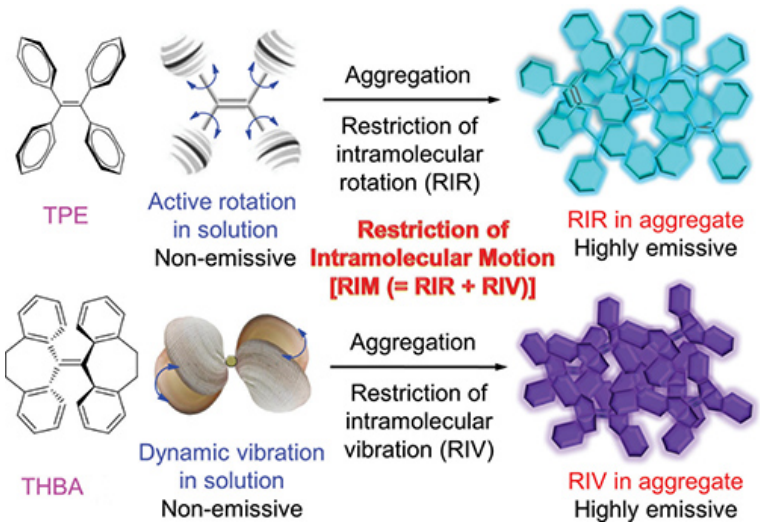

Figure 2.3 Propeller-shaped TPE is non-luminescent in a dilute solution, but becomes emissive upon aggregation due to the RIR of its phenyl rotors against its ethylene stator in the aggregate state. Shell-like THBA behaves similarly, due to the RIV of its bendable vibrators in the aggregate state.Figure taken from reference 6.

Guided by the idea of RIR as the cause of AIE, the first AIE active organic molecules contained many flexible, highly mobile fragments, but since later on many systems also exhibited AIE when the mobility of such fragments was restricted, mentions to the RIV or RIM mechanisms started to appear in the literature. This is again an example of over-classification in the AIE field introducing new terms for slightly different phenomena. From the physical point of view, either in TPE or in THBA, the origin of the observed AIE is the same: interactions in the aggregates or crystals not present in dilute solution constrain certain nuclear motions that are related to non-radiative decay. Although the restriction of rotations is a very visual concept for experimentalists that has guided a rational design of AIE molecules, one should not think that these are pure rotations of the phenyl rings in HPS or TPE, but combinations of low-frequency normal modes which may be different for every specific case. For this reason, we recommend the use of the more general RIM concept for all cases.

Although the RIM mechanism provides a general guiding mechanism to explain most of the observed phenomena related to AIE, let us note that nevertheless it is not incompatible with the existence of other possible causes. Since the AIE behavior arises from a complex equilibrium between radiative and non-radiative relaxation pathways, which is further complicated in most organometallic compounds in which strong SOC allows the population of excited triplet states via intersystem crossing, it should not come as a surprise that in some cases mechanisms alternative to RIM might be at the origin of the observed AIE behavior. Apart from RIM, several alternative mechanisms have been proposed to explain AIE[6], among them the restriction of intramolecular charge transfer[40], twisted intramolecular charge transfer[41-43] (TICT), E-Z isomerisation[44-47], formation of J-aggregates[48-50], intramolecular planarization[51-53], dual mode of assembly[54], excited state intramolecular proton transfer[55-57] (ESIPT) and excimer formation[58-61]. Although these mechanisms have been successfully applied to explain AIE for some particular cases, none of them is however applicable to a broad class of materials as in the case of RIM, and from this point of view their influence in the design of new materials has been limited to some families of related compounds with special structural features.

Although there has been certain consensus in the literature about the role of the phenyl ring torsions being responsible of the observed AIE in TPE, other authors claimed that the non-radiative decay in solution could be interpreted as an internal conversion mediated by an

ethylenic twist, as in the case of deactivation of ethylene from its first excited state that can relax back to the ground state via a conical intersection seam[29]. In order to identify the ultrafast deactivation mechanisms responsible for fluorescence quenching of TPE in the gas phase, a recent study[62] has explored its excited state dynamics using a mixed quantum-classical formalism based on trajectories that represent the motion of the molecular system upon photoexcitation. In this study the authors found that, although excited TPE molecules can deactivate via an ethylenic twist as suggested earlier in the bibliography,[63-65] about 75% of the trajectories proceed through photocyclization. These results explain, for instance, why ortho-terphenyl does not fluoresce, while the meta- and para- isomers do. From the experimental point of view it is, however, quite difficult to unambiguously differentiate this deactivation path from a RIM mechanism since both are linked to the motion of the phenyl rings. In the case of RIM the restriction of internal rotations would block a non-radiative channel, while in the case of photocyclization, phenyl-ring torsions are needed to bring the S_1 and S_0 PESs close together. In this case restricting the torsional motion would, in principle, prevent the system of reaching the CI and block the non-radiative decay promoting the radiative pathway.

Another relevant work trying to explain AIE from a theoretical and computational point of view of non-adiabatic transitions is that by Prof. Blancafort. In a first paper[66] the AIE of diphenyldibenzofulvene (DPDBF) was addressed by modeling a cluster from the crystal structure within a QM/MM framework, where one excited molecule was embedded in the crystal environment, and the results were compared to the case of the isolated molecule in solution. The DPBDF molecule is very similar to TPE, where two of the phenyl rings are fused so that only the remaining two are “free to rotate”. For the isolated molecule, a CI seam was found, providing an efficient relaxation channel back to the ground state after photoexcitation, resulting in poor emission. In the solid state however, the CI seam was not accessible since the rotation around the exocyclic fulvene ring, which was the main decay coordinate in solution, was blocked by the environment, thus too high in energy to be accessed after photoexcitation. It is worth to point out that the minimum of the CI seam of DPDBF in the solution very much resembles that of prototypical ethylene, both characterized by a 90º twist of the exocyclic fulvene and ethylenic bond respectively. In a following work[67], the same authors studied dimethyl tetraphenylsilole (DMTPS), a molecule closely related to HPS where two phenyl rings are replaced by methyl units. They followed a similar computational procedure as in the preceding paper and coined a new term, restricted access to a conical intersection (RACI), to describe the mechanism

behind the AIE of DMTPS. Similarly to DPDBF, DMTPS in solution can relax to the ground state via an energetically available CI. The nuclear motion leading to the intersection for DMTPS in solution was found to mainly involve a twist of the silole ring and a flapping motion of the phenyl substituents. Again, inaccessibility of the CI seam in the rigid crystal environment due to steric effects was proposed to explain the AIE. From these results, the authors concluded that RACI must be quite a general model to explain AIE in medium sized molecules. Moreover, they realized that the vast majority of organic molecules exhibiting AIE have typical subunits which are known to relax via CIs, hence the AIE for most cases must be due to inaccessibility to the state crossings that relax the molecule back to the ground state. Prof. Blancafort and co-workers concluded their paper by highlighting that the RACI mechanism is consistent with the earlier proposed RIM, since in the solid state there is a restriction of the intramolecular motions that lead to the intersection.

Besides blocking an effective non-radiative deactivation pathway by rigidification upon aggregation, an alternative, but not mutually excluding, possibility is to achieve efficient AIE inducing a change in the nature of the emitting state when bringing the isolated molecules into contact. If emission from this new state is more efficient than from the original state from which molecules were emitting in solution, an enhancement of the luminescence should be observed. Of course, this reasoning implies that the probability of non-radiative de-excitation should be smaller, or at least equal to that in the isolated molecules. A nice example of this case can be found in reference 60 where in contrast to the general observation that excimer formation quenches the light emission of aromatic hydrocarbons, two derivatives of TPE, containing one and two pyrene units, respectively, exhibit efficient excimer emissions in the solid state with fluorescence quantum yields up to 100%. According to the authors, in this case, the the π–π intermolecular interactions between the pyrene rings, which typically lead to the ACQ effect, when coupled with multiple C–H···π hydrogen bonds arising from the TPE units to the pyrene aromatic system, lead to more rigid excimers in which the non-radiative energy decay channel is blocked, making the dye molecules highly emissive in the solid state. This example was described by the authors as a novel phenomenon called aggregation enhanced excimer emission (AEEE).

In 2011, Prof. Kim and coworkers reported the observation of very efficient phosphorescence at room temperature for purely organic crystals.[68] Their work represented

a great advance in the field of organic room temperature phosphorescence and illustrates the potential complexity behind the solution/solid-state relative PL. In their work they studied the photophysical properties of a bromobenzaldehyde derivate in solution and in the solid state. In solution, this molecule is fluorescent, while in crystalline samples, the fluorescent band intensity decreases and a phosphorescent band appears. By clever crystal design, the authors achieved a phosphorescent quantum yield at ambient temperature of 55% for cocrystals of bromobenzaldehyde and dibromobenzene derivatives. Their design strategy consisted in combining the "heavy atom effect" of bromine with the well-known SOC present in n,π* and π,π* singlet and triplet states of the cabonyl unit, as extensively studied[69] by El-Sayed. These two characteristics were merged in the co-crystal by strong halogen bonding C-O···Br between neighboring molecules, leading to high phosphorescent efficiencies. Similar photophysical properties have been observed in substituted benzophenones,[19,26] and they were ascribed to restricted rotation of aromatic rings bonded directly to the carbonyl units. In my opinion, the enhanced phosphorescence is most probably due to a combination of factors. Certainly, molecular motions, which are related to non-radiative channels, are hindered in the crystals due to a rigid environment, but other factors must have a major role. In particular, the halogen bonding boosts SOC at the carbonyl unit, increasing the rate of ISC to the triplet manifold and the radiative emission from the triplet state.

Up to now, only examples of the AIE phenomenon in organic molecules have been discussed, although there are many examples in the literature[5,20,70] of d-block metal complexes exhibiting AIE. In particular, Cu(I), Au(I), Zn(II), Re(I), Ru(II), Ir(III), Os(IV), Pd(II), and Pt(II) compounds have been investigated due to their AIE properties. Organometallic complexes based on Pt(II) and Ir(III) are the most studied ones, the latter will be discussed in the following section. Changes in the nature of the emitting state are especially frequent for the d^8 and d^{10} metal complexes, where the presence of metallophilic interactions[71] (such as Pt···Pt and Au···Au interactions) can significantly influence the excited state properties of complexes, such as the formation of triplet metal-metal to ligand charge transfer (MMLCT) or ligand to metal-metal charge transfer (LMMCT) excited states.[72] Besides an enhancement of the luminescent emission upon formation of these M···M contacts in the aggregates, the change in the nature of the emitting state is usually accompanied with a change in the color of the emission that can be exploited in the design of chemosensors[14] or other stimuli responsive materials.

1.3 Fermi golden rule approach to non-radiative decay

Fermi's Golden rule[73] was derived from time-dependent perturbation theory to estimate transition rates between quantum states subject to a perturbation. The transition probability per unit time, in other words, the rate constant, from an initial state *i* to a final state *f* is usually expressed as

$$\Gamma_{i\to f} = \frac{2\pi}{\hbar}\left|\langle f|\hat{H}'|i\rangle\right|^2 \delta(E_f - E_i) \qquad (2.1)$$

where Ĥ' is the perturbation operator and the Dirac delta function represents energy conservation. It is important to note that this rule is only applicable to a continuum of final states, since the delta function requires an integral over one of its arguments to be meaningful.

In the field of molecular photophysics, within the Born-Oppenheimer and Franck-Condon approximations, the non-radiative rate between the lowest vibrational level of the initial excited electronic state (*i,0*) to a continuum of isoenergetic levels of the final electronic state (*f,n*) is usually expressed as

$$\Gamma_{i,0\to f,n} = \frac{2\pi}{\hbar}\left|\langle \Psi_f|\hat{H}'|\Psi_i\rangle\right|^2 \sum_n \prod_j^{3N-6}\left|\langle \chi_{f,n_j}|\chi_{i,0_j}\rangle\right|^2 \delta(E_{f,n} - E_{i,0}) \qquad (2.2)$$

where Ψ correspond to electronic wave functions, χ to harmonic oscillator wave functions and N to the number of atoms. The summation of the delta function over *n* is what gives rise to the density of final states, usually encountered in some Fermi golden rule expressions. Basically, the rate depends on the squared modulus of the electronic couplings and of the vibrational overlaps (FC factors). For the case of internal conversion, the adiabatic electronic states are coupled via the kinetic energy operator, giving rise to terms of the form

$$\left\langle \Psi_f\left|\frac{\partial}{\partial Q_m}\right|\Psi_i\right\rangle \qquad (2.3)$$

which are know as derivative couplings where Q_m represents a normal mode.

To get further insight into the origin of AIE in organic compounds, some authors have focused on the non-radiative decay rate from a Fermi golden rule approach. Especially, the group of Prof. Shuai has investigated in detail which normal modes contribute to internal conversion for several organic AIE active molecules.[35-39,74-80] According to his work, the

relevant modes will be those with large Huang-Rhys (HR) factors,[81] also known as electron-phonon couplings. However, the explanation as to why these will be the important modes for non-radiative decay is not clearly given in his papers. In the following lines, we will explain what these HR factors are and give an interpretation of their relationship with non-radiative decay.

Under a displaced harmonic oscillator model, where the ground and excited states are represented by two parabolas with the same frequency ω_i along a normal mode distortion, the HR factor of each mode is related to the displacement (ΔQ_i) between the minima of both states by

$$HR_i = \frac{\omega_i (\Delta Q_i)^2}{2\hbar} \qquad (2.4)$$

These factors were named after Huang and Rhys because they first appeared in their famous 1950 paper devoted to a theory of light absorption and non-radiative transitions in F-centers[82]. Their derivation of the non-radiative rate however is quite involved and difficult to follow, and it is not straightforward to identify there what nowadays are known as the HR factors. It is worth to mention that at that time, other authors were interested in non-radiative transitions of trapped electrons in crystal lattices. In particular, Ryogo Kubo[83], who is the author of the well-known "Statistical Mechanics" book used worldwide in graduate courses. A decade later, in the late 60's and beginning of 70's, Jortner did significant work on the theory of intramolecular radiationless transitions together with Bixon and Englman.[84,85] Jortner's most relevant contribution is probably the energy gap law[**86**], which states that the rate of radiationless transitions decreases exponentially with increasing energy gap between the involved electronic states. He applied Kubo's previous work on the generating function method[83] to non-radiative decay expressions based on Fermi's Golden rule. This allowed him to handle complicated expressions that contained intractable summations of products of electronic terms (derivative couplings) and FC vibrational overlap integrals. Something that is usually ignored in the literature when reference is made to the energy gap law is that it was derived under the weak coupling limit, in which the relative displacement of the multidimensional PES corresponding to the two electronic states is "small". This energy gap corresponds to the energy difference between the excited and ground states at the excited state minimum (ΔE in Figure 2.4a). In his paper, the strong coupling limit was also considered, where the relative horizontal shift between both PES is large and these surfaces are expected to cross or intersect in the

vicinity of the minimum of the excited state PES. For this strong coupling scenario, Jortner arrived to the conclusion that the radiationless transition probability decays exponentially with the energy gap of the crossing of both surfaces with respect to the minimum energy of the excited state (E_A in Figure 2.4b). Due to the formalism employed by Jortner in the derivation of the energy gap law, the influence of the energy gaps ruling radiationless transitions in both coupling limits on the electronic and vibrational terms of the rate constant could not be traced back. However, the effect of the energy gaps in both limiting cases on the FC factors may be qualitatively grasped. In the weak coupling limit, the overlap between the v = 0 vibrational wave function of the excited state with a vibrational wave function of the ground state at the same energy will be larger as ΔE decreases, since for low vibrational quantum numbers, the ground state vibrational wave functions will be more localized on the center of the well. For the strong coupling limit, the energy gap between the crossing and the excited state minimum is much smaller than the energy gap between both states at the excited state minimum ($E_A << \Delta E$). Therefore, the v = 0 vibrational wave function of the excited state will overlap with wave functions of high vibrational quantum number. Since for this situation the vibrational wave function spills over the edges of the well, the overlap will be larger as the energy gap between the crossing and the excited state minimum is reduced. Regarding the electronic coupling term of the non-radiative rate for the case of the strong-coupling limit, the closer the crossing is to the excited state minimum (i.e. smaller E_A), the lower the energy gap between both states will be at the excited state minimum (ΔE). Hence, due to the inverse dependence of the derivative couplings with the energy gap, the electronic term will be important for non-radiative decay.

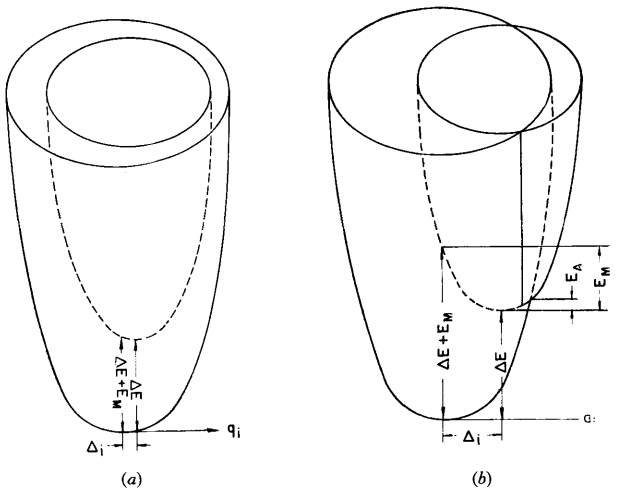

Figure 2.4 Schematic representation of the two adiabatic potential surfaces (ground and excited state) in two-dimensional vibrational space. (a) The weak coupling limit. (b) The strong coupling case. Taken from reference 86.

Although the current understanding of radiationless transitions in molecules is usually attributed to Jortner's work, another scientist derived[87] equivalent expressions to those of Jortner some years before. Sheng Hsien Lin published a paper[88] in 1966 entitled "Rate of interconversion of electronic to vibrational energy". In his work, the vibrational term of the radiationless transition probability is given in terms of the HR factors. However, even if an approximation at low temperatures is made, the expression is still too complex (equation 45 in reference 88) to conclude unambiguously that the larger the HR factors are, the more they contribute to the rate.

The HR factor will certainly influence the derivative couplings and the FC factors, and of course, if a mode is to be responsible for the non-radiative rate, the electronic and vibrational contributions must be non-vanishing for this mode. So in view of the previous discussion, the argument that those modes with large HR factors will be responsible for non-radiative decay holds in the case of states that are well energetically-separated at the FC region, so that the vibrational overlap increases with increasing separation between the minimum of both PES. Within this picture, the derivative couplings are not considered and assumed to be non-vanishing for modes with large HR factors. However, some wave-handing interpretation may be done in this sense. For the case just discussed of states who's energy separation at the FC region is significant, the larger the HR factor of a mode, the closer the crossing between both surfaces will be to the excited minimum, thus, the smaller the energy gap with the ground state at the excited state minimum, which may lead to increased derivative couplings because of their inverse relationship. It is important to stress that the limiting case of largest HR factor (displacement between PES) in the above arguments is when the surfaces cross at the minimum of the excited states PES. Otherwise, relaxation on the PES after excitation would already encounter a crossing between states before reaching the excited state minimum, and within this framework, non-radiative decay from the minimum of the excited state is assumed.

1.4 Ir(III) complexes

Hexacoordinated complexes of Ir(III) have attracted a lot of interest in recent years because of their phosphorescent emission that can be of benefit for many applications.[89-91] The Ir(III) cation has a $[Xe]4f^{14}5d^{6}$ electronic configuration, and like the rest of metals belonging to period 6 of the periodic table, their d-orbitals present a rather large octahedral crystal-field splitting. The most popular complex in this family is certainly $[Ir(ppy)_3]$,

where three 2-phenylpyridine ligands (ppy) coordinate to the metal center yielding an octahedral coordination structure. This complex has been extensively studied, from experimental[92-94] and theoretical[95] viewpoints, in particular its optical properties, which are controlled by the frontier molecular orbitals. The highest occupied MOs of this complex consist of the t_{2g} set and π-type orbitals from the ppy ligands, while the lowest unoccupied MOs are of π*-type from the ppy ligands. The triplet emitting state (T_1) has been assigned to be of MLCT character,[92] with some admixture of ligand-centered (LC) π,π* transitions on the ppy ligands. Because of the presence of strong SOC, [$Ir(ppy)_3$] exhibits a very bright green phosphorescence in solution with almost a 100% quantum yield at room temperature.[92] A part from boosting phosphorescent emission, SOC in this complex is responsible for the degeneracy breaking of the three components of the triplet state. In particular, the energy gap between the lowest and highest energy component of T_1 is known as the zero-field splitting (ZFS), and for the case of [$Ir(ppy)_3$] it takes a large value of 170 cm^{-1}. Because of the loss in degeneracy, emission has been detected[92] from the three substates of T_1 in [$Ir(ppy)_3$].

To understand why Ir(III) complexes can hold strong SOCs that allow very efficient phosphorescence, it is important to recall from a qualitative point of view what SOC is. SOC describes the process by which the magnetic moment associated to the spin angular momentum of an electron interacts with the magnetic moment due to its orbital motion. The net result of this coupling between spin and orbital angular momenta is that the spin magnetic moment can be reversed.[96] Hence, within this context, transitions between different spin multiplicity states can take place. The magnetic field created by the orbital motion of the electron serves as a magnetic torque which reverses the spin magnetic moment, but since the total angular momentum must be conserved during the process, a change in the orbital angular momentum occurs simultaneously to the spin flip. In other words, among other factors which will determine the strength of the spin-orbit interaction, a transition between spin-pure singlet and triplet states will only be possible if it can be accompanied by a change in the orbital angular momentum of the electron, i.e. the spin flip must be compensated by an orbital change. As Lionel Salem said,[97] the spin flip and the momentum change which creates it occur simultaneously.

Rayleigh-Schrödinger first order perturbation theory can be used to illustrate in a more rigorous fashion how a “spin-impure” state Ψ_T is constructed from the mixing of a spin-

pure triplet state, Ψ_T^0, with pure singlet states Ψ_{Si}^0 via the SOC operator[98] (equation 2.5). The mixing coefficient is given by the SOC matrix element divided by the energy difference between the coupled states, hence, efficient SOC will be important only when the energy difference between the mixed states is small and the magnitude of the SOC matrix element is significant.

$$\Psi_T^{SOC} = \Psi_T^0 + \sum_i \frac{\left\langle \Psi_{S_i}^0 \middle| \hat{H}_{SOC} \middle| \Psi_T^0 \right\rangle}{(E_T - E_{S_i})} \Psi_{S_i}^0 \qquad (2.5)$$

The first order correction to the energy vanishes since $\hat{H}_{SOC}$ cannot couple a state with itself. In order to see the effect of SOC on the energy of the coupled state, one must resort to the second order correction:

$$E_T^{SOC} = E_T^0 + \sum_i \frac{\left| \left\langle \Psi_{S_i}^0 \middle| \hat{H}_{SOC} \middle| \Psi_T^0 \right\rangle \right|^2}{(E_T - E_{S_i})} \qquad (2.6)$$

The assumption that the SOC operator, $\hat{H}_{SOC}$ can be expanded as a sum of one-electron phenomenological operators (equation 2.7) provides a qualitative description of the coupling between states. The SOC parameter ζ, which appears next to the dot product between the orbital and spin angular momenta, is a collection of physical constants and increases roughly with the fourth power of the nuclear charge, Z^4.

$$\hat{h}_{SOC} = \xi \hat{\boldsymbol{l}} \cdot \hat{\boldsymbol{s}} \qquad (2.7)$$

If we attempt to evaluate the SOC matrix element between a singlet and a triplet state with the one-electron SOC operator, several rules of thumb can be easily deduced.[98] First of all, due to the Slater Condon rules for one-particle operators,[99] two states will only couple if they differ at most in one spin-orbital. Moreover, a "heavy atom" type effect[96] must be present if efficient SOC is desired, due to the dependence of the SOC constant with the atomic number. As a consequence of the one-center nature of the phenomenological operator, the coupled spatial orbitals must be located in the same region in space, and have metal contribution in order to obtain reasonable magnitudes for the SOC matrix elements. Finally, for two spatial orbitals to couple, they must possess different magnetic quantum number m_l.

In the context of Ir(III) complexes, SOC between ^{1}MLCT and ^{3}MLCT states involving a different d orbital and the same LUMO can be rather significant, and due to the large atomic number of Ir, efficient SOC takes place. After the spin-pure triplet is mixed with

singlet states by SOC, a radiative transition can take place to the ground state since intensity is borrowed from the coupled singlet states. There is a very nice and illustrative chapter[98] by Prof. Yersin, in which SOC matrix elements are evaluated from molecular orbitals of Ir(III) organometallic complexes.

Many efforts have been made by organometallic synthetic chemists to obtain new Ir(III) complexes with tunable photophysical properties.[100-102] Ir(III) complexes may be classified according to the ligands. For instance, $[Ir(ppy)_3]$ is said to be an homoleptic complex because there is only one kind of ligand, which is referred to as cyclometalating in this case. If one of the ppy ligands is replaced by some new ligand, then the complex is called heteroleptic, and this new ligand is usually referred to as ancillary ligand. Despite some definitions of an ancillary ligand state that it is not directly involved in the photophysics of the complex, this is not always true.[103,104] By wisely choosing the ancillary ligand, its MOs may combine with the occupied d metal orbitals, and the empty orbitals from the ancillary ligand may lie quite below the e_g-type orbitals, since these are rather high in energy for Ir(III). In this new scenario, states originating from many mixtures may arise, as for instance, metal-ligand to ligand charge transfer (MLLCT), in which electron density is transferred from the metal and one of the ligands, to another ligand.

1.5 AIE in Ir(III) complexes

There is some controversy in the literature regarding the origin of AIE in several Ir(III) complexes. In a first paper by Huang and co-workers,[22] they reported AIE in two complexes, namely Ir-DBM and Ir-SB (Figure 2.5). By comparison to a closely related complex (Ir-acac) with intense photoemission in solution, they arrived to the conclusion that excimer formation was behind the AIE observed for Ir-DBM and Ir-SB. The authors modeled the Ir-DBM complex using periodic calculations, simulating the situation in solution and in the solid state with unit cells of different size, and arrived to the conclusion that the emissive state in the two situations has a different electronic nature. According to their calculations, in solution the LUMO corresponds to a π^* orbital located on the DBM ligand, while in the solid state it also delocalizes on the ppy ligands. Based on these results, they proposed the triplet emitting state of Ir-DBM to be of LC character on the DBM, thus not phosphorescent, while in solid state, due to π-stacking interactions between ppy ligands of neighboring molecules, the emitting state would have MLLCT character, where electron charge transfers from the metal to all the ligands. Although these calculations bring a

valuable information regarding the differences in the electronic structure of the Ir-DBM complex in different environments, my experience in the computational study of similar compounds indicates that the HOMO-to-LUMO excitation is not always the lowest electronic transition of Ir(III) hexacoordinated complexes. Hence, it might not be appropriate to extrapolate the emission properties of these compounds by only considering the two frontier orbitals, since lower and higher orbtials, e.g. HOMO-1 or LUMO+1, might play a major role. This situation is even more delicate when relaxation on the excited state PESs is taken into consideration.

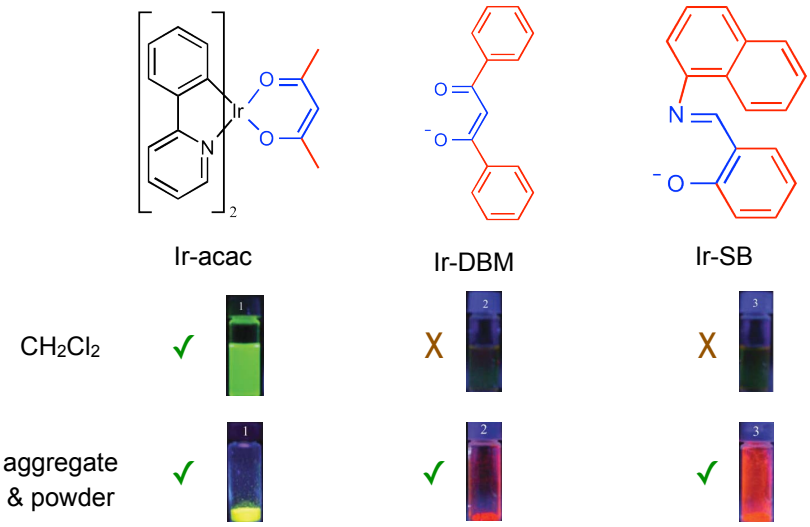

Figure 2.5 Complexes Ir-acac, Ir-DBM and Ir-SB together with their emission pictures, taken from reference 22.

Despite the vertical intermolecular separation between coplanar ppy ligands in the crystal structure of Ir-DBM (~3.4 Å) might suggest the presence of potential π-interactions, the overlap between π-electron clouds is poor, limited to one carbon atom. In fact, the Ir-DBM ligands are arranged in chains interacting via the π-systems of the ppy ligands, and by analyzing the crystal structure of the other two complexes (Ir-acac and Ir-SB), we found analogous chains in their respective crystals. It is worth to mention that, although the authors based all their study in the comparison to the Ir-acac complex (which does not present AIE), they did not mention that similar π-stacking interactions are also present in its crystal structure.

A "*Comment on*" paper was published shortly after by Soo Young Park and co-workers,[105] claiming that the most plausible explanation for AIE in Ir(III) complexes is the restriction of intramolecular motion and not the formation of intermolecular excimers. They studied

four Ir(III) complexes (Figure 2.6) which exhibit AIE and are closely related to Ir-DBM and Ir-SB. They investigated the impact of different substituting units on the iminic nitrogen and the effect of fluorination of the ppy ligands on the AIE properties. The authors stated that if excimers were responsible for the emission in the solid state, then the emission energies of Ir-R_1 and Ir-R_2 should be the same. The emission wavelength of both complexes however are quite different, and so by performing additional experiments they discarded the formation of excimers being responsible for AIE. They also performed TDDFT calculations for different structures along the rotation path of the aryl substituent on the iminic nitrogen and found that, close to the torsion angle of the crystal structure, the energies of the two lowest excited triplet states cross. They concluded that this rotation can be thermally activated and that the nature of the emitting triplet state changes leading to non-radiative decay in solution. In other words, the RIR of the N-aryl bond would suppress a non-radiative decay pathway in solution. However, the nature of these triplet states is not very clear from their explanation. In order to clarify this issue, in section 8 we have studied a complex very similar to Ir-R_1, with N-pyridine instead of N-phenyl.

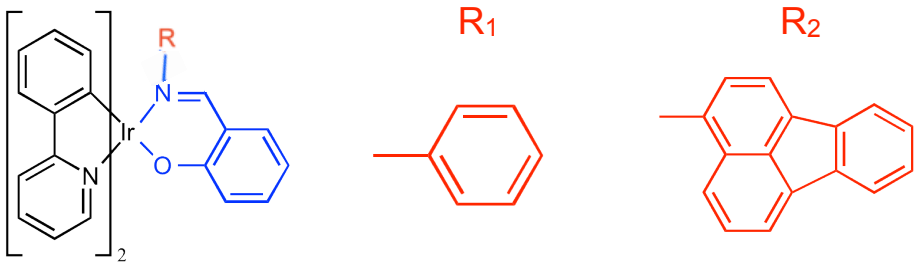

Figure 2.6 Complexes Ir-R_1 and Ir-R_2 studied in reference 105.

A third paper by Huang,[106] replying to the comment of Soo Young Park, explored the AIE of Ir(III) complexes closely related to the previous ones in which the free rotation of ligands in two of the complexes was not possible (Figure 2.7). The paper started by noticing that the authors of the "*Comment on*" paper "ignored the presence of π-π stacking of the adjacent pyridyl rings of their single crystals". Indeed, in the crystal structure of Ir-R_2 with fluorinated ppy ligands, the molecules pack forming dimers facilitating intermolecular π-interaction between the ppy ligands. The authors of this study observed that AIE is also present when intramolecular rotational motion is blocked, and concluded that "the formation of excimers by π–π stacking of adjacent pyridyl rings of ppy ligands plays a key role in EPESS". Again, relevant π-stacking interactions are present in the crystal structure of the two complexes for which free rotation of the ligands is not possible.

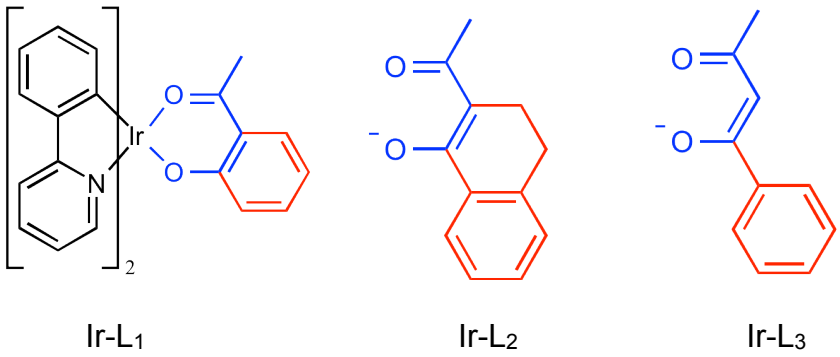

Ir-L_1 Ir-L_2 Ir-L_3

Figure 2.7 Complexes Ir-L_1, Ir-L_2 and Ir-L_3 studied in reference 106.

In my opinion, the underlying common problem among these studies is the search for an ultimate and general explanation for the origin of AIE in all Ir(III) complexes. Although all the complexes in these three papers are closely related, the origin of the AIE emission may not necessarily be the same or even unique. In this direction, some years after the publication of these papers, a new report appeared[107] in which all the complexes from the previous papers were investigated in detail together with a new series of closely related Ir(III) AIE active complexes. In this study the authors performed several experiments in order to univocally support or rule out the formation of excimers and the presence of a RIR mechanism. They also complemented their studies with DFT calculations. From these results, they arrived to the conclusion that the ancillary ligand in these complexes suffers an important geometric distortion when the T_1 state relaxes in solution. However, this distortion is smaller in the solid state since the complexes are closely packed. According to the authors of this study, the larger geometrical distortion between S_0 and T_1 in solution would lead to enhanced FC factors, increasing the non-radiative decay rate. The authors did not comment further on this point, but these enhancement of FC factors would be related to larger HR factors in solution, as discussed in the previous section.

An important point that many authors exploring the AIE in Ir(III) complexes do not comment on is whether the non-radiative decay back to the ground state, responsible for the weakness or absence of emission in solution of AIE complexes, takes place on the singlet or triplet manifold. For several Ir(III) complexes it is well known that ISC between these two spin manifolds is quite fast,[90] leading to efficient population of the triplet state. Moreover, in dilute solutions of AIE complexes phosphorescence is already observed in many cases, meaning that the triplet state is populated. Then, it is plausible to expect that non-radiative decay on the T_1 state leads to population of the ground state in solution.

Therefore, for this case, in the Fermi golden rule approach the electronic coupling terms would be SOC and / or vibronic SOC since non-radiative decay would operate ISC.

From this discussion it is clear that the origin of AIE in Ir(III) complexes is still controversial, and that a lot of knowledge still lacks on the competition between the different photophysical pathways. The study of these complexes with advanced experimental techniques complemented with electronic structure calculations appears to be a suited way to gain a deeper insight into the photophysics of Ir(III) complexes.

2. General objectives

The work presented herein was motivated by a collaboration with the group of Prof. Inamur Rahman Laskar at the *Birla Institute of Technology and Science* in Pilani, India. They synthesized and characterized all the studied Ir(III) complexes, investigated their photophysics using diverse experimental techniques and explored their potential practical applications. Our main goal was to rationalize their experimental observations taking into account the details of the electronic structure of the complexes. We were mainly interested in how the nature of the ligands affects the character of the emitting state, as well as what is the most plausible explanation for the observed AIE of the investigated Ir(III) complexes.

3. Computational modeling

3.1 Methods and states

Because of the size of the investigated complexes, we have chosen to use the KS formulation of DFT[108] for geometry optimizations of the ground and lowest energy triplet states, in its spin restricted and unrestricted forms, respectively. Since the complexes from this chapter are phosphorescent, and according to Kasha's rule,[29] this radiative process should take place from the lowest triplet (T_1) state, DFT is an adequate choice since it will, in principle, yield the lowest energy state of a given spin and spatial symmetry. The calculation of vertical excitations has been carried out with TDDFT from either the optimized S_0 or T_1 structures, depending on whether we were interested in the absorption or emission process.

An alternative choice to obtain the T_1 state would have been to optimize it with TDDFT.[109] In this case, the m_s=0 component is calculated instead of the m_s=1, as obtained from a single determinant KS-DFT calculation. In absence of SOC or external magnetic fields, the three components of T_1 are degenerate. However, the optimization of T_1 with DFT or TDDFT does not handle the state on the same footing, and usually the energies won't be degenerate, although we expect them to qualitatively hold the same spatial electronic nature (this is not the situation for some pathological cases). In the m_s=1 DFT triplet, the spin-orbitals are those optimizing the energy of the T_1 KS determinant, while within TDDFT, the optimization runs through the amplitude space of single excitations while keeping the orbitals optimized for the S_0 ground state. Although these two optimization spaces are somehow related[110] they technically correspond to different electronic structure approximations to the triplet state, which is the reason why the computed DFT and TDDFT T_1 energies differ.

In general, the geometry optimization on an excited state PES might be rather troublesome, since different states may cross (i.e. switch their ordering) along the minimization procedure. Such computational issue might be specially relevant in the case of organometallic complexes. These compounds have a relatively dense set of low-lying states (compared to small organic molecules), and calculations may diverge or oscillate between two or more solutions. In some cases it can be difficult to follow the target triplet state, contrary to singlet states, since the oscillator strength cannot intuitively guide us in this sense because it is null. Moreover, triplet states calculated with TDDFT usually comprise several amplitudes, and the order of the MOs may also change along the optimization process, making the track of the target state even more difficult. Some codes however include an algorithm that tries to follow the eigenvector of the target state, which can alleviate the problem when the target state crosses with another state.

Optimization of T_1 with DFT presents other advantages with respect to TDDFT, namely that it is computationally less demanding and that the optimized space is more flexible (spin-orbital vs. amplitude). DFT optimization is even more justified when we are interested in calculating frequencies for the T_1 minimum, since analytical derivatives are widely available for DFT but not always for TDDFT.

The B3LYP hybrid functional[111,112] has been systematically employed in geometry optimizations, except for the complexes in section 5, for which we used the B97-D functional[113] since its geometrical structure suggests that dispersion interactions, due to the presence of triphenylphosphine ligands, might be important in this case. Comparison between B97-D and B3LYP geometries in this case does not highlight any relevant differences between their structural parameters, hence, for the sake of consistency, geometry optimizations for the rest of studied Ir(III) compounds have been done at the B3LYP level. Moreover, the optimized structures with B3LYP compare reasonably well with the experimental ones. The M06-2X functional[114] was used when studying weak interactions between complexes and the CAM-B3LYP functional[115] was used to study a charge transfer transition in one of the ligands from an Ir(III) complex.

3.2 Basis sets and pseudopotentials

The size of the Ir(III) complexes studied in this chapter has limited us to the use of relatively small basis sets. Since in all the studies of this chapter we were interested in relative excitation energy differences between very similar complexes, we expect that the error introduced by the size of the basis set is in principle of the same order of magnitude for the complexes we have compared, and thus it is mostly cancelled when comparing relative values.

For the calculation of excited states, polarization functions are mandatory and diffuse functions are also desirable, thus the Pople double-ζ quality 6-31G(d) and 6-31+G(d) basis sets[116-119] have been generally used for light elements when carrying out geometry optimizations or excited state calculations. However, the computational times, specially for optimization calculations, increase notably when diffuse functions are added. Moreover, for extended systems, the use of diffuse functions sometimes leads to unwanted linear dependencies of the atomic orbital basis set.

Iridium is a heavy atom belonging to the 6th period of the periodic table. Because of the large number of electrons and since relativistic effects start to be non-negligible, a pseudopotential (also known as effective core potential, ECP) has been systematically employed to model the core electrons. This has been done by using the LANL2DZ basis set[120] (Hay and Wadt from Los Alamos), which is a combination of an ECP for the core electrons while the valence electrons are treated with a double-ζ quality basis set.

3.3 Structures

The proper characterization of the structural properties of the studied complexes has a central role in our investigations, since their photophysical properties are strongly linked to structural patterns. In this sense, the ground state molecular geometry of Ir(III) complexes in the the crystal structure has been refined by optimizing the position of the hydrogen atoms bonded to the Ir(III) center with respect to the X-ray structures, since the exact crystallographic positions of hydrogen atoms bonded to heavy metals are usually not well resolved by X-ray crystal diffraction. The restricted optimizations of these hydrogen atoms were performed by keeping the rest of the atoms frozen at the experimentally determined crystal structure. When modeling the complexes in the vacuum or in solution, full optimizations were performed for the monomer. Some of the studied complexes contain very flexible diphosphine ligands, therefore, the ground state PES has probably several local minima. Since preliminary calculations indicate that these flexible ligands were not actively involved in the low-lying excited states, we did not pursue a thorough exploration of the ground state PES.

3.4 Excited states

3.4.1 Computation of excited states

Although the low-lying excited states of the studied Ir(III) complexes have a certain degree of CT character, it is important to notice that this is very different with respect to the long-range CT states of the dyes investigated in the previous chapter. In general, the low-lying states of the studied Ir(III) complexes have predominantly MLCT character with some ligand to ligand charge transfer (LLCT) and LC admixtures. Because of the octahedral coordination environment of the metal center, the CT separation is much smaller than in the D-π-A dyes, and has a different spatial distribution, i.e rather radial from the metal to the ligands, in comparison to the more linear CT from the D to the A fragment in the D-π-A dyes. The strong electron/hole separation in the studied push-pull organic dyes forces the computational use of LRC functionals in order to properly recover the physical nature of the electronic transitions. Typically, the LRC functionals have been parametrized for the computation of strong CT excitations in organic systems, and thus their use in the study of organometallic complexes might not be the best computational option. Indeed, in a paper by Yersin and co-workers,[121] devoted to the analysis of charge-transfer excited states in phosphorescent organo-transition metal compounds, the authors showed that excitation

energies calculated with LRC functionals are systematically overestimated with respect to experimental data. Moreover, they found that the B3LYP functional performed very well for the excited states of these systems, and that the CT character is not very pronounced. It is worth to point out that these authors concluded their report by saying that the CT present in the studied metal compounds does not pose a significant challenge for TDDFT, opposed to what happens with long-range CT. Since according to the authors B3LYP provides a balanced treatment of MLCT and LC states and mixtures among them, we have employed this functional to study the excited states of Ir(III) complexes in this chapter.

As it will be shown in the results section, our calculations of vertical absorption energies agree very well with the experimental bands of Ir(III) complexes. However, when we compute vertical emission energies from the optimized T_1 state, the experimental values are significantly underestimated, although we capture the relative differences between complexes. In the paper by Yersin,[121] they got a very good agreement with experimental 0-0 emission energies by calculating triplet emission energies with B3LYP (average 0.05 eV error). They computed the 0-0 emission energies from the vertical ones including zero-point energy corrections. They were able to compare their values to 0-0 energies from highly resolved optical spectra in the range of the electronic 0-0 transition. Our collaborators unfortunately could not record highly resolved spectra, therefore, we compared their emission values with our vertical emission energies.

3.4.2 Characterization of excited states

The excited states of the studied Ir(III) complexes have been characterized in several ways. The most straightforward being direct analysis of the amplitudes of the computed excited states in order to identify and quantify those MOs involved in the electronic transition. For the emitting T_1 state, the singly occupied spin-orbitals have been checked, but its nature has then been analyzed by performing a TDDFT calculation at its minimum geometry. Since in all the cases the character of the emitting state is analogous to the first triplet state at the FC geometry, for simplicity, most of the discussions in this chapter are based on the S_0 MOs from the TDDFT calculation. In several cases, specially for triplet states, several amplitudes account for the vertical transition from the ground state, complicating such analysis. Therefore, in some cases, electronic density difference plots between the state of interest and the ground state have been useful to assign the nature of the state. For example, by visualizing the MOs it may seem that there is some LC character mixed to the

main MLCT nature of the transition, but density difference plots may allow one to see if the LC admixture is larger or less than presumed just by orbital inspection.

To get a semiquantitative measure of the amount of MLCT character of the electronic transitions, Mulliken population analysis for the ground and excited states electronic densities has been performed. The %MLCT of the transition is then estimated as the difference of the atomic Mulliken charges on the iridium atom from the ground and excited state.

Natural transition orbitals[122] (NTOs) can also be quite helpful to visualize the nature of excited states. For the case of the triplet states with many contributing amplitudes however, they were not very useful since there was not a single dominant hole-particle pair. In the characterization of electronic transitions in molecular dimers, NTOs improved the description with respect to the amplitude analysis, identifying two main hole-particle pairs.

3.5 Spin-orbit coupling

The phosphorescence observed for the Ir(III) is possible due to non-vanishing SOC, since the electric dipole moment cannot couple states of different spin multiplicity. However, the inclusion of such relativistic effects in large systems such as the complexes studied herein is not yet something done routinely and widely available in standard quantum chemistry packages. However, since I started my PhD studies, there has been a notable improvement in this sense and new and updated quantum chemistry codes have appeared able to perform TDDFT calculations including SOC.

When should one consider SOC in the calculations? Well, it depends on what you are interested in. Taking SOC into account allows to obtain spin-mixed states from which phosphorescence transition probabilities can be calculated, and in turn estimate the life-time of the spin-mixed "T_1" emitting state. The ZFS can also be calculated, since the three components of the triplet loose their degeneracy. The absorption spectrum may also be simulated in the basis of the spin-mixed states.

For most chemical systems, the full relativistic machinery is not necessary,[123] in other words, a relativistic molecular theory where the four-component Dirac equation is reduced to a two component form[124,125], is usually sufficient to account for the leading relativistic

corrections at a molecular level. One technique to do this is to decouple the large from the small components (the large components acquire significant values for the matter solutions while the small ones do for the antimatter ones) by finding a relationship between both components that eventually eliminates the small ones. Depending on the expansion used to relate both components, different approximate Hamiltonians are available. Amongst them, the Zero Order Regular Approximation[126] (ZORA) represents a very good compromise between accuracy and computational cost, and substantially improves the historically well-known Breit-Pauli Hamiltonian[123] by including an expansion which avoids most of the disadvantages present in the latter one.

A well know quantum chemistry program that includes SOC through ZORA and within TDDFT calculations is ADF[127,128]. In the following lines, the methodological approach available in this code will be briefly outlined. The KS-DFT equations solved in the ADF program are collected in equation 2.8, where T is the kinetic energy operator, V^{KS} stands for the local KS potential, while φ_i and ε_i represent the one-electron MOs and the corresponding orbital energies respectively.

$$\left[T + V^{KS}\right]\varphi_i = \varepsilon_i \varphi_i \tag{2.8}$$

If the ZORA kinetic energy operator shown in equation 2.9 is used (where σ is the vector of the Pauli matrices), two-component relativistic calculations will be performed. When equation 2.9 is expanded (equation 2.10), it is clearly seen that the ZORA operator can be split into two distinguished terms, the scalar relativistic (SR) and the SOC one, since it is the second term that involves coupling between the spin (represented by σ) and momentum.

$$T^{ZORA} = (\vec{\sigma}\cdot\vec{p})\frac{c^2}{2mc^2 - V^{KS}}(\vec{\sigma}\cdot\vec{p}) \tag{2.9}$$

$$T^{ZORA} = T^{SR} + T^{SOC} = \vec{p}\cdot\frac{c^2}{2mc^2 - V^{KS}}\vec{p} + \frac{c^2}{\left(2mc^2 - V^{KS}\right)^2}\vec{\sigma}\cdot\left(\vec{\nabla}V^{KS}\times\vec{p}\right) \tag{2.10}$$

Solving equation 2.8 with T^{ZORA} is a two-component calculation in which SOC is included self-consistently in the TDDFT calculations. These calculations however are rather computationally demanding, specially for large systems like the Ir(III) complexes studied herein. A further approximation may be done by neglecting the SOC term in equation 2.10,

thus doing a one-component calculation. Then, SOC can be introduced perturbatively around the SR calculation, making the computation much more tractable.

As an example of such calculations, here we show the simulated absorption spectrum for three complexes studied in section 4.1 (Figure 2.8). In the simulations, spin-orbit coupling effects were computed pertubatively. The simulated absorption profile matches quite satisfactorily with the experimental spectrum, and the absorption of triplet states can be seen at the long wavelength tail of the main absorption band.

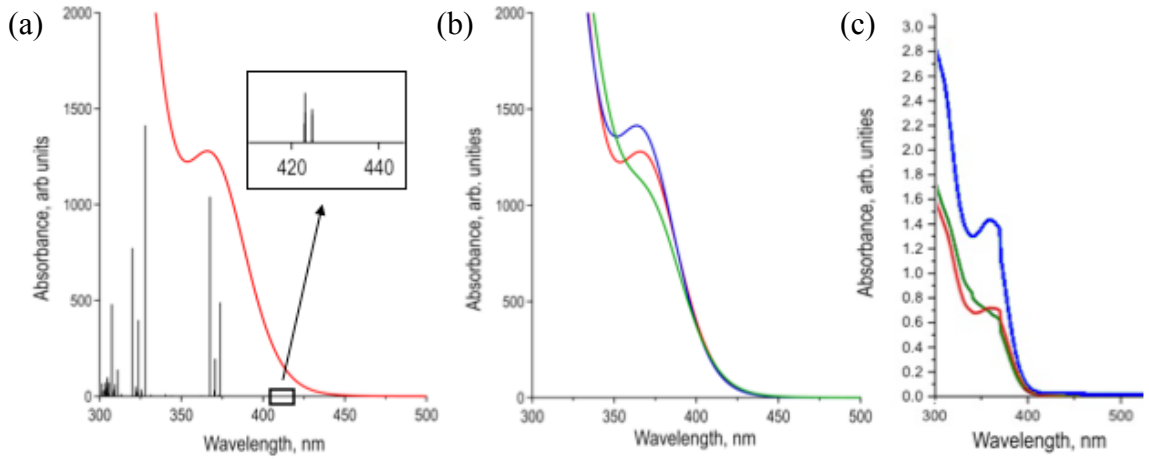

Figure 2.8 Absorption spectrum of Ir(III) complexes studied in section 4.1: **PP2** (red), **PP3** (green), **PP2'** (blue). Simulated (a) and (b) computed with one-component ZORA TDDFT with the B3LYP functional and the following basis set: iridium (TZP and frozen core), light atoms (DZP). Experimental spectra (c) in DCM.

In Figure 2.9 the peaks corresponding to singlet and spin-mixed states after SOC inclusion are shown. As it can be seen, SOC does not have a significant impact on the energy of the states, while the intensities are somewhat modified. However, when one simulates the absorption profile, the inclusion of SOC does not modify the overall shape, and the only noticeable difference is that there is absorption from spin-mixed triplets at low energies (Figure 2.8).

From these results we conclude that the perturbative SOC correction has a very small effect on the computed excitation energies to the low-lying states. The estimated ZFS of low-lying triplets is also quite small. Moreover, the optimized geometries of T_1 were not altered by the inclusion of SR effects. Our goal in this chapter is the interpretation of experimental results, and this is more straightforward with spin-pure states than spin-

mixed ones. Moreover, the experimental emission spectra of several studied complexes exhibit a vibrational structure, so one can afford not to include SOC since the FC factors are the relevant parameters and not the oscillator strengths of the transitions. Taking into account all these points and considering the preliminary results discussed above, we decided no to include SOC effects in our calculations.

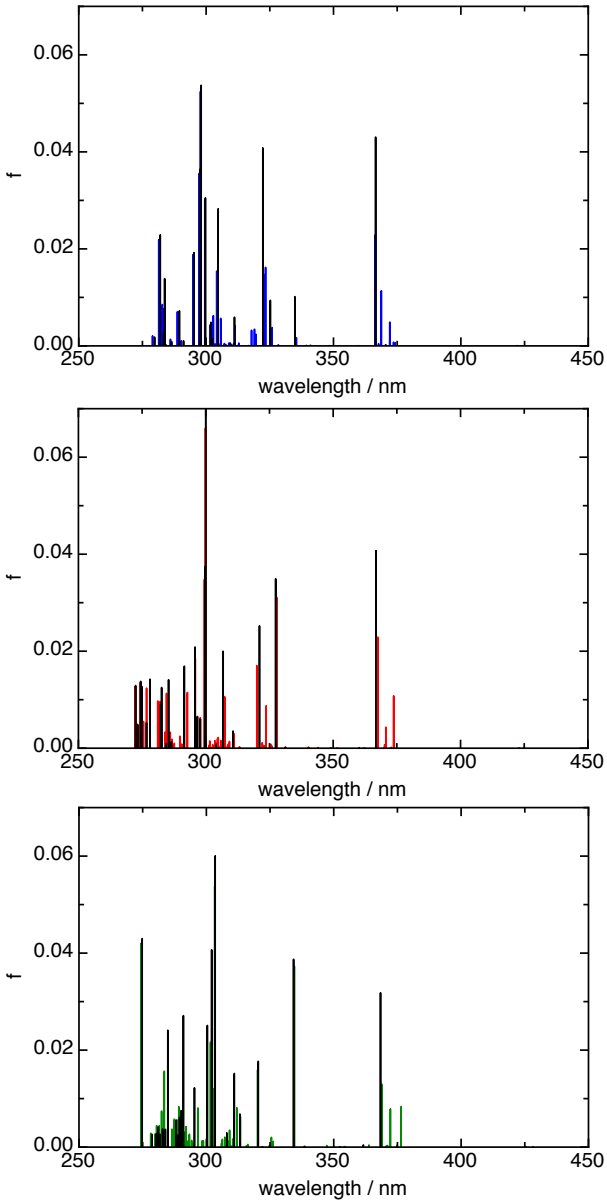

Figure 2.9 Stick absorption spectrum of Ir(III) complexes studied in section 4.1: **PP2** (red), **PP3** (green), **PP2'** (blue). Black sticks correspond to pure singlet excited states while colored ones correspond to SOC spin-mixed states computed with one-component ZORA. All calculations were done with the B3LYP functional and the following basis set: iridium (TZP and frozen core), light atoms (DZP).

3.6 Emission color

The emission color of a molecule is a direct consequence of the overall shape and position of the emission band in the visible region of the spectrum and the sensibility of the observer's vision to visible radiation at different wavelengths. From an emission spectrum, the colors perceived by the human eye may be estimated following a very simple procedure that uses three color matching functions (CMFs) that describe the chromatic response of a standard observer in a given color space. The values of these CMFs may be found tabulated in the literature.[129] In the standard CIE (2º) 1931 color space,[130] a specific color is described by two numerical values, the *x* and *y* chromaticity coordinates that are obtained combining the values of three intermediate X, Y, Z coordinates (equation 2.11). These are calculated by the overlap integral (equation 2.12) between the emission spectrum, ε(λ), and the corresponding CMFs $\overline{x}(\lambda)$, $\overline{y}(\lambda)$ or $\overline{z}(\lambda)$ in the visible range. For the numerical evaluation of the integrals in equation 2.12, a 1 nm increment is sufficient to attain accurate results.

$$x = \frac{X}{X+Y+Z} \qquad \mathrm{y} = \frac{Y}{X+Y+Z} \tag{2.11}$$

$$X = \int_{visible} \overline{x}(\lambda)\varepsilon(\lambda)d\lambda \tag{2.12}$$

The two *x*, *y* coordinates can then be plotted on a chromaticity diagram to compare the emission color of different complexes.

3.7 Vibrationally resolved emission spectra

In section 7, the vibrationally resolved emission spectrum of a series of Ir(III) complexes has been simulated with the Gaussian package.[131] Herein I will briefly discuss the approximations employed to simulate these spectra.[132]

The intensity of an electronic transition depends on the modulus squared of the transition dipole moment

$$Intensity_{\substack{abs \\ em}}(\omega) \propto \sum_{''} \left|\langle \Psi' | \boldsymbol{\mu} | \Psi'' \rangle\right|^2 \delta(E'' - E' \mp \hbar\omega) \tag{2.13}$$

where Ψ' and Ψ'' correspond to the initial and final vibronic states, respectively, and the conservation of energy is expressed by the Dirac delta function.

Within the Born-Oppenheimer and FC approximations, the transition dipole moment[29] is given by

$$\langle \Psi' | \boldsymbol{\mu} | \Psi'' \rangle = \boldsymbol{\mu}_{if} \langle \chi_v' | \chi_v'' \rangle \qquad (2.14)$$

where $\boldsymbol{\mu}_{if}$ corresponds to the electronic transition dipole moment at the equilibrium geometry of the initial state and χ_v' and χ_v'' correspond to the vibrational wave functions of the initial and final states, respectively. By adopting the harmonic approximation, the multidimensional vibrational wave functions χ_v may be expressed as a product of monodimensional wave functions $\chi_{vi}(Q_i)$, where Q_i is one of the N normal modes, describing the *i-th* vibration mode of the molecule.

$$|v\rangle = |\chi_v\rangle = \left| \prod_{i=1}^{N} \chi_{v_i} \right\rangle \qquad (2.15)$$

Since we are interested in the phosphorescence emission, SOC should be taken into account to evaluate the electronic transition dipole moment. However, here we are specially interested in the vibrational resolution of the spectrum. Therefore, the electronic transition dipole moment is not considered in our simulations because within the FC approximation, it is only a multiplicative factor and the shape of the vibrationally resolved spectrum will be governed by the FC integrals $\langle v' | v'' \rangle$.

However, the vibrational wave functions of each state are expressed in a different set of normal coordinates, those corresponding to S_0 and T_1, respectively. Therefore, to evaluate the FC factors, the Duschinsky transformation[133] (equation 2.16) is invoked. This is a linear transformation proposed long ago (1937), which allows to express the normal coordinates of one state (Q') in terms of the ones of the other state (Q'').

$$Q' = \boldsymbol{J}Q'' + K \qquad (2.16)$$

In equation 2.16, $\boldsymbol{J}$ is the Duschinsky matrix representing a rotation and K is the shift vector that accounts for the geometry changes between the initial and final states. This transformation is generally a good approximation if the two geometries are not very different from each other. The HR factors discussed in section 8 correspond to the K vector, in which the Duschinsky rotation effects are included.

Although the calculation of the $\langle 0'|0'' \rangle$ integral is rather simple, this is not the case for $\langle v'|v'' \rangle$. The computational procedure used to evaluate $\langle v'|v'' \rangle$ is similar to the one given by Sharp and Rosenstock,[134] but employing recursive formulae[135] to express $\langle v'|v'' \rangle$ in terms of $\langle 0'|0'' \rangle$, the latter one being calculated exactly.

Since we are particularly interested in the emission spectrum, we assume that emission takes place from the lowest vibrational level of T_1, i.e. we are not taking temperature effects into account, so the integrals which in the end are evaluated to simulate the spectrum are all of the kind $\langle 0'|v'' \rangle$. Although there are many integrals to evaluate, most of them correspond to transitions of negligible intensity. The algorithm implemented in Gaussian[132] takes advantage of such sparsity by employing a pre-screening scheme to select the most relevant transitions and reduce computational costs.

3.8 Environment effects

3.8.1 Solvent effects

In our initial studies of Ir(III) complexes solvent effects were considered via the implicit IEF-PCM method.[136-138] For the following studies we however decided to neglect solvent effects in the calculations for different reasons. One being that the solvent used by our experimental collaborators is dichloromethane (DCM), which has a moderate polarity, with a dielectric constant ε=8.93. Secondly, the absorption and emission spectra recorded by our collaborators are barely affected by the solvent polarity.

Moreover, since we are mostly interested in comparing similar Ir(III) complexes for which the nature of the states is analogous, the (small) solvent effects will probably be equivalent for all of them. For these exposed reasons, we have only included the effects of the solvent in our calculations when they can have an important influence on the properties we were interested in, for example, in section 7, where an Ir(III) complex with a Schiff base ligand presented a solvatochromatic emission band.

3.8.2 Crystal structure

In the search for the potential causes of the observed AIE for the Ir(III) complexes studied in this chapter we have performed investigations in two complementary directions: (i)

detailed analysis of the crystal structures and (ii) computational simulations of the crystal environment through cluster and QM/MM calculations.

Regarding the analysis of the crystal structures, on one side, we searched for interactions between π-systems of the complexes that could lead to excited states delocalized over more than one complex. This would result in a change of the nature of the emitting state with respect to the case of dilute solution. Also, to see if the RIM mechanism could be a plausible explanation for AIE, we looked for specific interactions between monomers in the crystal that could restrict the motion of flexible ligands, depriving non-radiative decay paths. In particular, we found weak noncovalent C-H···π interactions[139,140] in their crystal structures for several of the studied Ir(III) complexes. These are attractive interactions largely ruled by dispersion and to a less extent, by charge-transfer and electrostatic forces. Also, C-H···Cl interactions were found,[141,142] which are considered to be hydrogen-bonding type and highly directional.

In the solid state, two main environmental effects may modify the photophysics of the studied complexes. One would be interactions between monomers at an electronic level. Depending on how the molecules are packed in the crystal, cluster models may be used to tackle with these problems. In this thesis we present the computation of molecular dimers to explore the possibility of electronic communication between neighbors in the crystal. Another environment effect would be the restriction of certain molecular motions due to the presence of nearby molecules. In this case, the description of the intermolecular interactions does not require the use of quantum mechanics and we have modeled these effects by performing ONIOM calculations,[143,144] in which a central complex is treated at the QM level and the immediate surrounding environment at the MM level.

4. Influence of ancillary ligands on the low-lying excited states of cyclometalated Ir(III) complexes

4.1 Bischelating ancillary phosphine ligands

4.1.1 Introduction

Heteroleptic cyclometalated Ir(III) complexes have become more attractive as emitter materials than their homoleptic counterparts, mainly due to their facile and versatile derivatization.[101] In particular, modulation of the ancillary ligand allows to tune the photophysical properties of Ir(III) phosphors, broadening the scope of their applicability. Although the ancillary ligand is sometimes referred to as non-chromophoric, it can indeed play an active role in the properties of the low-lying states of the complex. For instance, a convenient route to obtain different emission colors is by tuning the ancillary ligands in heteroleptic Ir(III) complexes.[103]

To achieve efficient full color RGB display systems, it is essential to obtain high efficiencies and color purities for the three primary blue, green, and red emitting materials. While there have been many reports on efficient pure green and red light-emitting complexes, the search for true blue emitters is more difficult.[145,146] Based on previous reports,[102,103] the incorporation of a strongly π-accepting PPh_2 unit in the coordination sphere of an Ir(III) complex should increase the HOMO–LUMO separation, opening the way to the synthesis of new blue-emitting complexes. Furthermore, the strong bonding of a P-donor ligand to Ir(III) increases the energy of d–d* excitations on the metal ion, minimizing their interference with the radiative transition from low-lying excited states. Motivated by these two features, our experimental collaborators aimed for new blue-emitting Ir(III) complexes using Ph_2PLPPh_2 type ancillary ligands. They synthesized and characterized three new cationic cyclometalated Ir(III) complexes (Figure 2.10) with general formula $[Ir(ppy)_2Ph_2PLPPh_2]PF_6$. They all consisted on an Ir(III) center coordinated with two ppy ligands and with three different P-coordinated phenylphosphine (Ph_2PLPPh_2) quelating ligands with L=ethane (**PP2**), propane (**PP3**) and ethylene (**PP2'**).

It is worth to point out that the majority of heteroleptic Ir(III) complexes have traditionally been synthesized by a lengthy two step process.[101] For the present study, the group of Prof. Laskar employed a microwave (MW) irradiation technique, which reduces the synthesis

time drastically as compared to conventional routes.[147] With this facile and expeditive synthetic approach, they synthesized the heteroleptic Ir(III) complexes studied herein.

Our goal in this study focused on the characterization of the low-lying excited states of the synthesized phosphorescent Ir(III) complexes (Figure 2.10), paying special attention to the influence of the ancillary Ph_2PLPPh_2 ligands.

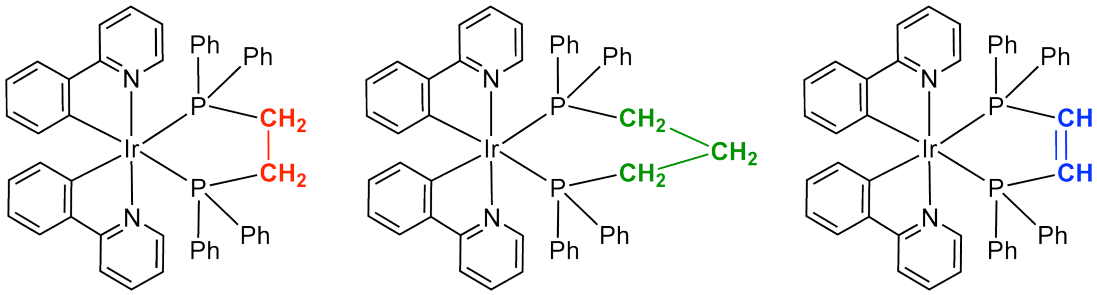

PP2 **PP3** **PP2'**

Figure 2.10 Investigated complexes with general formula $[Ir(ppy)_2Ph_2PLPPh_2]^+$.

4.1.2 Ground state geometries

Optimization of the ground state molecular structures of the three Ir(III) complexes in DCM solution yields very similar coordination environments for the iridium atom (Figure 2.11) in all three cases. They all have a distorted octahedral geometry with a *cis*-C,C-*trans*-N,N configuration. The optimized values for the Ir–X distances (Table 2.1) are in good agreement with those obtained for similar complexes,[148] both from X-ray diffraction studies and theoretical calculations. The most significant differences in the geometry of the coordination environment of iridium in the three complexes is the simultaneous opening of the P–Ir–P angle and closing of the C–Ir–C angle in **PP3** in order to fit the larger propane bridge between the two phosphorus atoms. This also leads to a slightly larger Ir–P distance in this case. There is, however, practically no difference between the other two cases with two-carbon bridges (**PP2** and **PP2'**). Of these two structural differences, the most important one is the opening of the P–Ir–P angle by almost 6°. The Ir–P bond lengths for **PP3** are somewhat larger than those reported for similar complexes of Ir(III),[149] an elongation that can be rationalized considering the strong *trans*-effect exerted by the C atom in *trans*-coordination position to the P one.

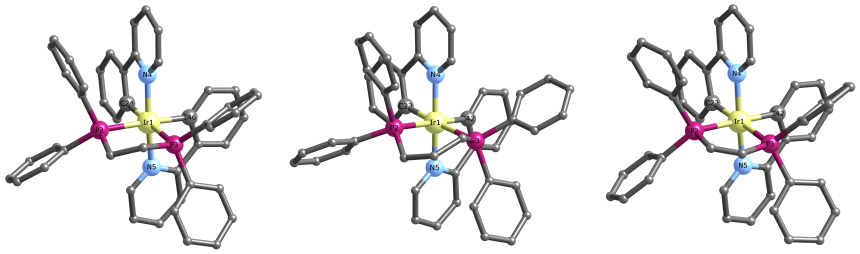

PP2 **PP3** **PP2'**

Figure 2.11 Molecular structures obtained for the optimized ground state of the three studied Ir(III) complexes (hydrogen atoms are not displayed for the sake of clarity).

Table 2.1 Geometrical parameters for the coordination environment of iridium in the three optimized ground state structures.

	Bond distances[a], Å			Angles (º)		
Complex	Ir-N	Ir-P	Ir-C	N-Ir-N	P-Ir-P	C-Ir-C
PP2	2.106	2.499	2.059	168.7	83.0	84.8
PP3	2.110	2.539	2.061	169.6	88.9	82.8
PP2'	2.109	2.479	2.059	168.6	82.9	86.2

[a]Average value of the two Ir-X distances in each compound.

4.1.3 Frontier molecular orbitals

A detailed picture comparing the HOMO and the LUMO for the three complexes is given in Figure 2.12. As it is evident from this picture, while there is a significant participation of d orbitals on the iridium atom together with π-type orbitals of the phenyl rings of the ppy ligands in the HOMO, the LUMO is, on the contrary, dominated by π*-type orbitals of the pyridine rings of the ppy ligands. The phosphine ligands are not involved in any of these two orbitals, and thus the calculated HOMO-LUMO gap is approximately the same for all of three complexes, with a value of ~4.1 eV.

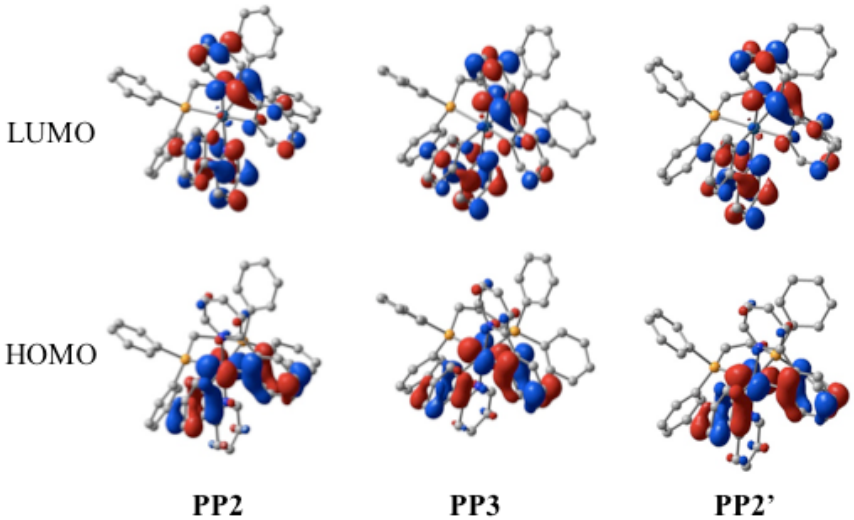

Figure 2.12 HOMO and LUMO of the studied complexes.

A representation of the MOs with significant participation in the low-lying excitations of complex **PP2** is shown in Figure 2.13. The composition of these orbitals can be understood in terms of linear combinations of fragment MOs. For instance, the LUMO and LUMO+1 correspond to in- and out-of-phase combinations of the LUMO of each pyridine fragment of the ppy ligand. For the occupied MOs, setting aside the d orbitals of the Ir(III) center that mix with the π-type orbitals of the cyclometalating ligand, the HOMO and HOMO-1 are a result of the combinations of the HOMO of each phenyl fragment of the ppy ligand, while the HOMO-2 and HOMO-3 are due to combinations of the HOMO-1 of the phenyl fragment. There is no significative participation of the phosphine ligands to any of the orbitals involved in the low-lying excitations for any of the three complexes. The MO diagrams for **PP3** and **PP2'** molecules are analogous to that shown in Figure 2.13.

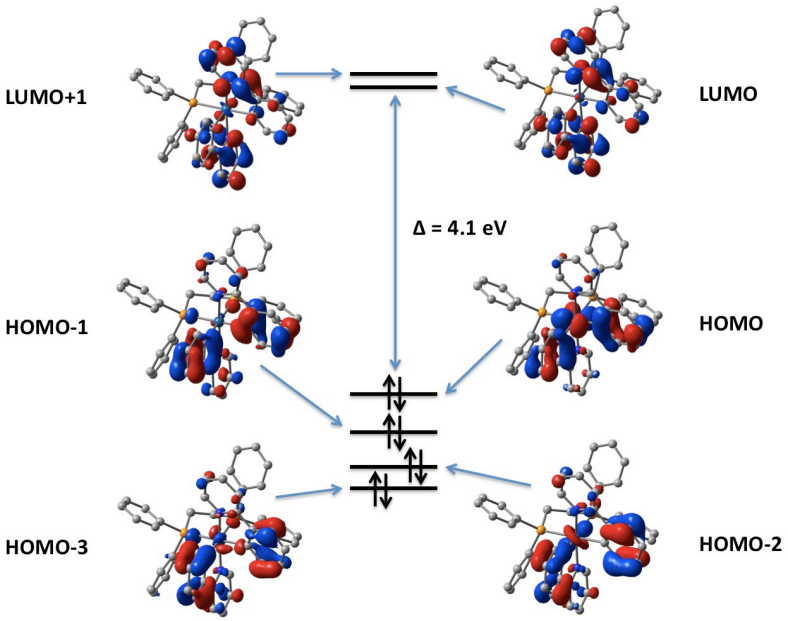

Figure 2.13 Frontier MO diagram for **PP2**.

4.1.4 Low-lying excited states at the Franck-Condon region

When calculating excited states of Ir(III) complexes, we are interested in the low-lying ones, which are responsible for the low and moderate intensity bands in the experimental UV/Vis absorption spectrum because these states are those populated when recording PL spectra. Computation of the electron excitation from the ground state to the first excited singlet state S_1 (Table 2.2) indicates that, for all three complexes, the electronic transition can be considered basically as a simple HOMO to LUMO electron promotion. According to this finding and considering the representation of the MOs involved in the transition (Figure 2.12), it can be deduced that this transition has significant MLCT character from the d orbitals of the iridium atom to the π system of the coordinated ppy ligands, mainly to

π* orbitals of the C_5N pyridine rings. It is also worth noting the existence of some degree of π to π* transition on the ppy ligand, with electronic charge being transferred from the π system of the C_6 phenyl ring of the ppy ligand to π* empty orbitals of the C_5N pyridine ring. As expected, the calculated vertical excitation energies are practically identical for all three compounds, in good agreement with the band at ~360 nm of the experimental absorption spectra.[147] Our calculations show that the oscillator strength is very similar for **PP2** and **PP2'**, the two complexes involving two-atomic bridges between the phosphine atoms, while it is predicted to be significantly lower for **PP3**, the complex with the propane bridge.

Table 2.2 Vertical excitation energies, oscillator strengths (*f*), and HOMO-to-LUMO contributions calculated for the S_1 state of the three studied complexes. HOMO and LUMO energies (in eV) are also given.

Complex	ΔE, eV (nm)	*f*	% H→L	E_H	E_L
PP2	3.39 (366)	0.072	97	-6.30	-2.21
PP3	3.39 (365)	0.058	97	-6.33	-2.22
PP2'	3.39 (366)	0.076	97	-6.28	-2.19

In order to interpret the emission spectra, we have also calculated vertical excitation energies to the two lowest lying triplet states (T_1 and T_2 in Table 2.3). The computed vertical transition energies to T_1 at the FC region are close to 435 nm for the three complexes, in agreement with the experimentally observed low-intensity tail that extends from 400 nm up to 450 nm. The experimental PL spectra[147] present two well-defined emission peaks at ~460 and ~490 nm, approximately separated by ~1400 cm^{-1}. Our calculations show for the three complexes the existence of two practically degenerate triplet states in the 430 nm region. Here, we can safely consider that geometry relaxation on the PES of one of these triplet states would lead to a lower energy gap with respect to the ground state, as well as to a loss of degeneracy. Such extrapolated behavior seems to be in fair agreement with the presence of two emission peaks in the experimental emission spectra. However, this structured emission profile has been described in previous studies on similar iridium compounds, and has been attributed to vibronic progressions related to the stretching of C–C double bonds at the aromatic ligands.[98] Indeed, simulation of the vibrationally resolved spectra for similar complexes discussed later in section 7 suggests that, most probably, the two peaks in the emission spectra of the complexes studied herein are due to vibronic progressions on the ppy ligand and not to emission from two close-lying triplet states.

Table 2.3 Vertical excitation energies calculated for the lowest lying singlet and triplet states for the three studied complexes.

Complex	States	ΔE, eV (nm)	Assignments
PP2	T_1	2.85 (435)	H-3→L+1 (7%), H-2→L (12%) H-1→L+1 (21%), H-1→L+3 (2%), H→L (42%)
	T_2	2.86 (434)	H-3→L (10%), H-2→L+1 (9%), H-1→L (27%), H→L+1 (35%),
	S_1	3.39 (366)	H→L (97%)
PP3	T_1	2.84 (437)	H-3→L+1 (6%), H-2→L (10%), H-2→L+1 (3%), H-1→L (4%), H-1→L+1 (15%), H→L (35%) H→L+1 (10%)
	T_2	2.85 (435)	H-3→L (9%), H-3→L+1 (3%), H-2→L+1 (6%), H-1→L (22%), H-1→L+1 (7%), H→L (7%) H→L+1 (28%)
	S_1	3.39 (365)	H→L (97%)
PP2'	T_1	2.85 (434)	H-3→L+1 (6%), H-2→L (12%) H-1→L+1 (22%), H-1→L+3 (2%), H→L (44%)
	T_2	2.86 (433)	H-3→L (9%), H-2→L+1 (10%), H-1→L (29%), H→L+1 (36%),
	S_1	3.39 (366)	H→L (97%)

The character of the transitions from the ground state (S_0) to the lowest excited singlet (S_1) and triplet (T_1) states has been analyzed by comparing the atomic Mulliken populations for each fragment in the molecule. The results, shown in Table 2.4, indicate a significant MLCT character for the $S_0 \rightarrow S_1$ excitation, which is similar for all three molecules, although it is interesting to note that the MLCT character is significantly lower in the case of the complex with an unsaturated carbon bridge, namely **PP2'**. According to this analysis, the MLCT character of the FC T_1 state is rather small, of ~10%, compared to the ~40% MLCT character of the S_1 state. These results clearly illustrate that the nature of the lowest excited singlet and triplet states of these complexes is indeed not comparable, as already hinted by the different amplitudes contributing to each state (Table 2.3). This is in contrast to some simplified models were these lowest exited states are believed to be purely of MLCT character, and equivalent for both spin multiplicities.[90]

Table 2.4 MLCT character for the transitions from the ground state (S_0) to the lowest excited singlet (S_1) and triplet states (T_1).

Complex	$S_0 \rightarrow S_1$	$S_0 \rightarrow T_1$
PP2	38%	11%
PP3	42%	10%
PP2'	34%	8%

The nature of the MLCT character of these transitions can be easily visualized by plotting the difference between the charge densities of the two states involved in the transition. This analysis is rather useful for the T_1 state, since compared to the S_1 counterpart which is mainly an HOMO-to-LUMO transition, several amplitudes account for the T_1 state. In Figure 2.14 the density difference plots for complex **PP2** are shown. From this representation, it can be seen that, the charge transfer in the $S_0 \rightarrow S_1$ excitation occurs mainly between the iridium atom and the two pyridine rings that are directly coordinated to it. An equivalent charge-transfer is obtained for the $S_0 \rightarrow T_1$ transition. For both S_1 and T_1 states, the LC π-π^* character on the ppy ligands plays a minor role than what could be inferred from a visual inspection of the molecular orbitals involved in the transition. Also, from this type of representation it becomes evident that the ancillary phosphine ligands do not play a direct role in the electronic transitions to the low lying excited states of these complexes, thus, equivalent density differences plots are obtained for the three complexes.

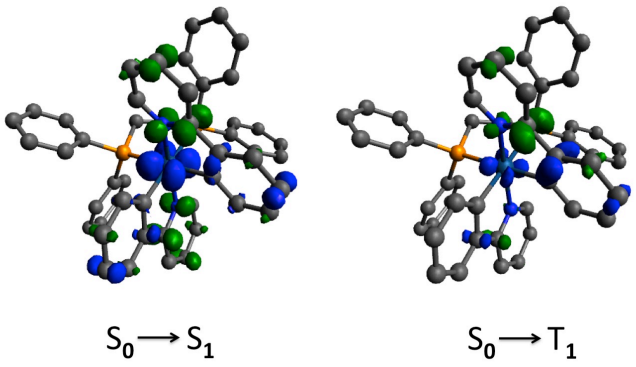

Figure 2.14 Electron density differences between the S_1 and S_0 states (left) and between the T_1 and S_0 states (right) for **PP2'**. Blue corresponds to negative values (higher electron density in the ground state) while green corresponds to positive ones (higher electron density in the excited state).

4.1.5 Conclusions

The inclusion of a strong π-acceptor chelating ligand (Ph_2PLPPh_2) in Ir(III) ppy complexes induces wide shifts of the maximum emission wavelength (λ_{max}) towards the blue-region of the spectrum, compared to emission of the archetypical [$Ir(ppy)_3$] homoleptic complex. This is in line with the fact that phenylphosphine ligands are strong field ligands within the

spectrochemical series. Although they are not directly involved in the electronic transition of the emitting state, the replacement of one ppy ligand by the bidentate phosphine ligand blue-shifts the emission band due to the loss of delocalization of the LUMOs on the cyclometalating ligands. The value of λ_{max} however remains almost constant when changing the ancillary ligand. Our calculations show that the nature of the emitting triplet state is mainly of MLCT character.

4.1.6 Computational details

Geometry optimizations for complexes **PP2**, **PP2'** and **PP3** in their ground state were carried out using quantum chemical calculations based on DFT with the B3LYP hybrid functional.[111,112] A basis set of double-ζ quality (LANL2DZ) and the ECP of Hay and Wadt[120] were used for iridium. For all other atoms, all-electron 6-31+G(d) basis sets have been used. The optimized ground state geometries were used to calculate vertical excitation energies to the low lying singlet and triplet excited states via TDDFT using the same functional and atomic basis sets. All ground state geometry optimizations and excited state calculations were performed in DCM solution. Solvent effects were taken into account via the IEF-PCM method.[136-138] All calculations have been done using the Gaussian 09 suite of programs.[131]

4.2 Monochelating ancillary phosphine ligands

4.2.1 Introduction

Inspired by the Ir(III) complexes studied in the previous section, we wondered how would the photophysical properties be affected by the coordinating mode of the ancillary phosphine ligand to the metal center. The group of Prof. Laskar synthesized by their MW technique three new neutral biscyclometalated Ir(III) complexes[150] (Figure 2.15) with appended diphosphine ligands as those previously studied. The general formula for this complexes is [Ir(F_2ppy)$_2$(Ph_2PLPPh_2)(Cl)], with F_2ppy=2-(2',4'-difluoro) phenylpyridine and L=ethane (**P2**), propane (**P3**) and ethylene (**P2'**). All the complexes exhibit blue phosphorescent emission, just like the complexes discussed in section 4.1. In contrast to the ancillary ligands from the previous section, herein the phenyl-substituted diphosphines have only one phosphorus atom coordinated to Ir(III), while the other one remains non-coordinated to the metal center and can, thus, be potentially utilized for selective sensing of metal ions. Moreover, **P2** exhibited AIE, a feature that is rather desirable for the application as a chemeosensor, in order to improve the detection limit of a species. Our collaborators carried out several experiments and found that the free phosphorus donor atom present on the appended diphosphine of **P2** provided selective binding to the mercuric ion (Hg^{2+}). The selective binding ability of the probe molecule towards Hg^{2+} resulted in a detectable signal due to complete quenching of its AIE properties. Hence, **P2** was shown to act as a promising Hg^{2+} sensor.

Our goal herein was to characterize the low-lying excited states of the synthesized complexes, and specially, to find out if the phosphine ancillary ligand participates actively in the excited states of the complexes, since now it binds monodentally to the metal center. Also, we wanted to identify the similarities and differences with the preceding bidentate ancillary ligands.

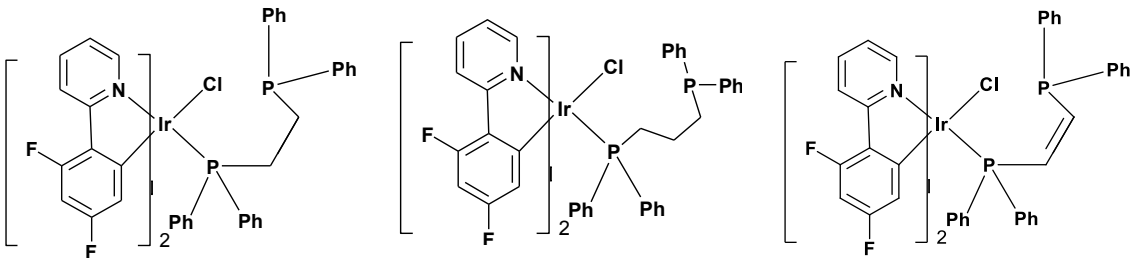

P2 **P3** **P2'**

Figure 2.15 Studied complexes of general formula [Ir(F_2ppy)$_2$(Ph_2PLPPh_2)(Cl)].

4.2.2 Ground state geometries

The optimization of the ground state molecular structures in DCM solution suggests slightly distorted octahedral coordination geometries for the three complexes (Figure 2.16). In the case of the **P2'** complex, the *trans* conformation in the ancillary diphosphine ligand was considered, since it was energetically lower than the *cis* one (represented in Figure 2.15). As shown in Table 2.5, there are no major differences neither in the Ir–X distances nor in the X–Ir–X angles between the three complexes, except for the Ir–P distance and the Cl–Ir–P angle, whose values increase slightly as the bridge between the two diphenylphosphines becomes larger. This trend was already noticed for the compounds of the previous sections, in which the diphosphine ligands coordinated to the metal center in a bidentate fashion.

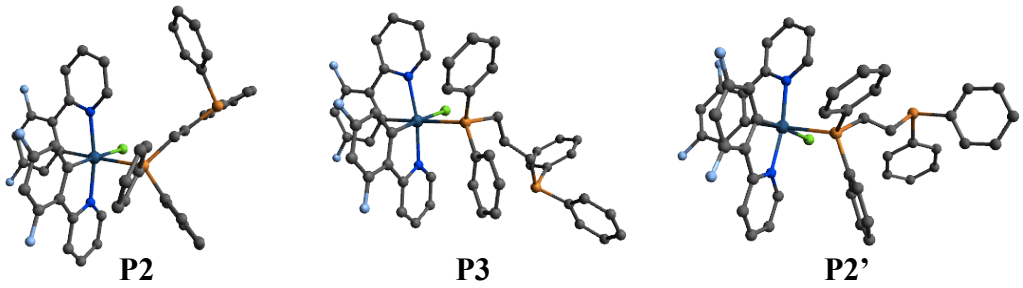

Figure 2.16 Optimized ground state molecular structures for complexes **P2**, **P3**, and **P2'**. Hydrogen atoms are not displayed for the sake of clarity.

Table 2.5 Geometrical parameters for the coordination environment of iridium in the optimized ground state structures in DCM solution of all studied compounds.

	Bond distances[(a)], Å				Angles (º)		
Complex	Ir-N	Ir-C	Ir-Cl	Ir-P	N-Ir-N	C-Ir-C	Cl-Ir-P
P2	2.091	2.025	2.589	2.582	170.0	89.9	90.2
P3	2.094	2.026	2.571	2.608	169.9	88.2	89.5
P2'	2.089	2.025	2.584	2.524	171.1	90.7	85.1

[(a)]Average value of the two Ir-X distances in each compound.

4.2.3 Frontier molecular orbitals

The frontier MOs of **P2** are shown in Figure 2.17. While the HOMO−3, HOMO−2 and HOMO have a remarkable contribution from the Ir(III) d orbitals, along with a p orbital from the Cl atom and some π character from the two ppy ligands, the HOMO−1 consists of a π type orbital located on one of the diphenylphosphines. It is also worth noticing that the lone pair of the phosphorus atom participates in the HOMO-1. This is the only frontier MO that has some participation from the ancillary ligand, in contrast to the bidentated

compounds previously studied. The LUMO and LUMO+1 are quasi-degenerate orbitals composed of π*-type orbitals located on the ppy ligands, with no significant metal participation. Except for the HOMO−1 and HOMO−3, all the other mentioned orbitals have a notable participation in the low-lying electronic states (Table 2.6). The relevant MOs related to the electronic transitions and the HOMO–LUMO gap of approximately 4.0 eV are quite similar for the three studied complexes (Appendix, Figure A2.1).

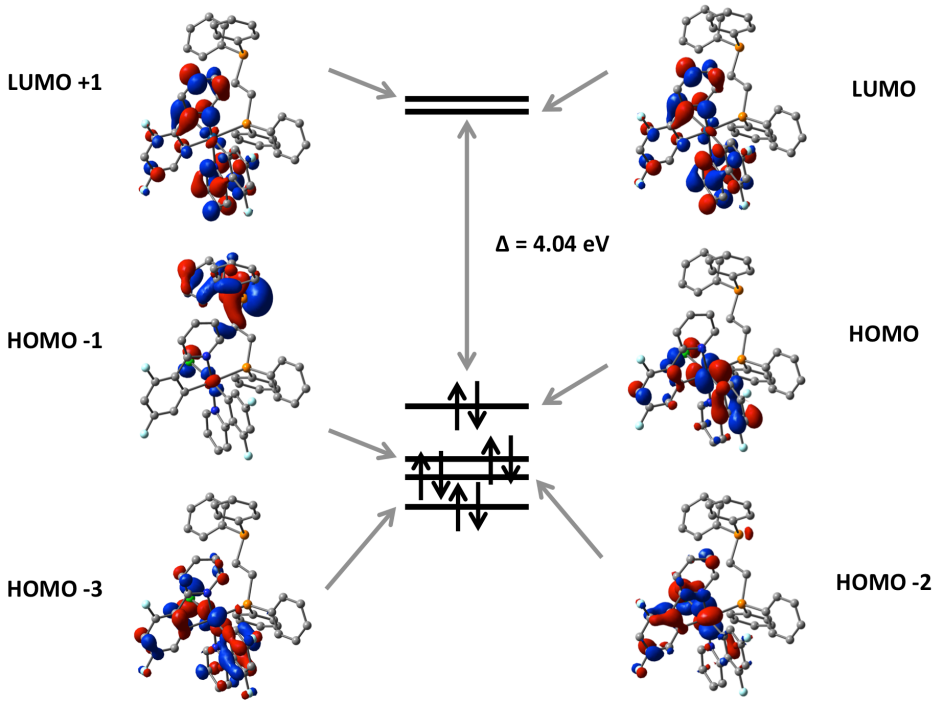

Figure 2.17 Highest and lowest occupied MOs for complex **P2**.

4.2.4 Low-lying excited states at the Franck-Condon region

The calculated excitation energies (Table 2.6) from the ground state to the first excited singlet state (S_1) for **P2** and **P2'** are very close to each other, 3.26 and 3.27 eV respectively, while for **P3** the vertical gap to S_1 is slightly lower, 3.19 eV. This electronic transition can be seen as a promotion of an electron from the HOMO to the LUMO, with an important MLCT character from the occupied d orbitals of the iridium atom to the π system of the two ppy ligands, together with some charge transfer from the p orbital of the Cl atom to the two ppy ligands and a significant π to π* transition within these ligands. The slightly smaller HOMO–LUMO gap obtained for **P3** (3.95 vs. 4.04 eV for **P2** and **P2'**) is responsible for the lower excitation energy calculated for this complex. The computed absorption wavelengths of ~380 nm to S_1 correlate satisfactorily with the experimental absorption spectra, which exhibits a peak at ~370 nm. The associated computed oscillator strengths predict similar absorption intensities for the three complexes, in good agreement with experimental observations.[150]

Table 2.6 Vertical excitation energies, oscillator strengths (*f*), and orbital contributions (≥5%) to the electronic transitions to the lowest excited states of the studied complexes.

Complex	States	ΔE, eV (nm)	*f*	Assignments
P2	T_1	2.87 (432)		H-4→L (10%), H-3→L+1 (8%) H-2→L+1 (14%), H→L (48%)
	T_2	2.89 (430)		H-4→L+1 (8%), H-3→L (8%), H-2→L (21%), H-2→L+1 (5%), H→L+1 (39%),
	S_1	3.26 (380)	0.037	H→L (95%)
	S_2	3.32 (373)	0.004	H→L+1 (95%)
	S_4	3.72 (333)	0.049	H-2→L (26%), H-2→L+1 (47%), H-1→L (5%), H-1→L+1 (9%)
P3	T_1	2.84 (436)		H-4→L (15%), H→L (60%)
	T_2	2.89 (428)		H-3→L (6%), H-3→L+1 (13%), H-2→L (7%), H-2→L+1 (18%), H→L+1 (38%)
	S_1	3.19 (389)	0.032	H→L (97%)
	S_2	3.33 (373)	0.004	H→L+1 (96%)
	S_4	3.75 (331)	0.043	H-2→L+1 (85%)
P2'	T_1	2.88 (430)		H-3→L (11%), H-2→L (28%) H→L (38%)
	T_2	2.90 (428)		H-4→L+1 (14%), H-3→L+1 (8%), H→L+1 (53%),
	S_1	3.27 (379)	0.025	H→L (94%)
	S_2	3.34 (372)	0.024	H→L+1 (95%)
	S_4	3.72 (333)	0.056	H-2→L (85%), H-3→L (5%)

In order to gain more insight into the nature of the electronic transitions observed in the experimental absorption spectra, excitations to other low-lying singlet and triplet states were also calculated. This information is summarized in Table 2.6. The excitation from the ground state to the second excited singlet state, S_2, is mainly a HOMO to LUMO+1 transition. The nature of this second excited singlet state is quite similar to that of the first excited singlet state because of the resemblance between the LUMO and LUMO+1, although the corresponding oscillator strength for this transition is almost negligible for **P2** and **P3**. The intense absorption band observed in the experimental spectra[150] at 300–330 nm corresponds mainly to the electronic transition to the fourth excited singlet state (with contributions from other high-lying singlet states). The major contribution to S_4 is an excitation from the HOMO−2 to the LUMO or LUMO+1, with an important MLCT

character as it is found for the first singlet state. In the low energy region of the absorption spectra (400–450 nm), a band of low intensity is observed, which can be attributed to the partially allowed transitions to low-lying triplet states due to the SOC induced by the presence of the metal centre. The calculated excitation energies to the first and second excited triplet states are in good agreement with the low intensity tail at ~450 nm in the experimental absorption spectrum.

The character of the transitions from the ground state (S_0) to the first and fourth excited singlet (S_1, S_4) and the first triplet states (T_1) has been further analyzed by comparing the atomic Mulliken populations for each fragment in the molecule. The results shown in Table 2.7 indicate a very similar MLCT character of the S_1 and S_4 excitations for the two complexes, while the MLCT character plays a minor role in the transition to the first excited triplet state (T_1). These results are comparable to those obtained for the complexes studied in the previous section. Hence, the coordination mode of the phosphine based ancillary ligand does not seem to affect the MLCT character in a significative way.

Table 2.7 MLCT character for the transitions from the ground state (S_0) to the first and fourth excited singlet (S_1,S_4) and triplet states (T_1).

Complex	$S_0 \rightarrow S_1$	$S_0 \rightarrow S_4$	$S_0 \rightarrow T_1$
P2	43%	46%	14%
P3	45%	48%	20%
P2'	41%	45%	13%

The nature of the MLCT character of these transitions can be visualized by plotting the difference between the charge densities of the two states involved in the transition. Figure 2.18 shows these difference plots for complex **P2**. From this representation it can be seen that the main electron transfer in the $S_0 \rightarrow S_1$ and $S_0 \rightarrow S_4$ excitations takes place between the iridium atom and one of the two ppy rings. If we pay attention at the details of these plots, it seems that a certain charge transfer character between the chlorine atom and the cyclometalating ligand is present in S_4, while it is insignificant in S_1. For T_1, in addition to the MLCT character there seems to be some ligand-centered π,π^* contributions. The plots for complexes **P3** and **P2'** are very similar to those of **P2**, confirming once again the passive role of the ancillary ligand in the excited state character.

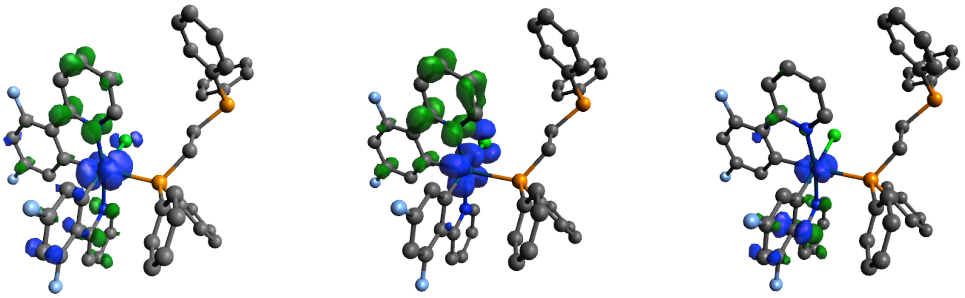

$S_0 \rightarrow S_1$ $S_0 \rightarrow S_4$ $S_0 \rightarrow T_1$

Figure 2.18 Electron density differences between the S_1 and the S_0 states (left), S_4 and S_0 states (middle), and T_1 and S_0 states (right) for **PP2**. Blue corresponds to negative values (higher electron density in the ground state) while green corresponds to positive ones (higher electron density in the excited state).

4.2.5 Conclusions

The calculated transition energies to low-lying excited states are in agreement with the experimental data. A MLCT nature can be assigned to the absorbing (S_0, S_4) and emitting (T_1) states, with some admixture of LC π,π* transitions on the ppy ligands. Although the lone pair of the phosphorus atom participates in the frontier molecular orbitals, it is not directly involved in these electronic transitions. Therefore, the binding mode of the phenylphosphine ligands does not influence greatly the photophysical properties of biscyclometalated Ir(III) complexes. Hence, similar blue-emitting complexes are obtained independently of the phosphine's binding mode. However, it is important to notice that the lone pair plays an important role in the selective binding of Hg^{2+}.

4.2.6 Computational details

Ground state geometry optimizations were performed with DFT using the B3LYP hybrid functional.[111,112] A basis set of double-ζ quality (LANL2DZ) and the ECP of Hay and Wadt[120] were used for iridium, whereas a 6-31G(d) basis set was used for the rest of the atoms. In order to describe the electronic transitions to the low-lying singlet and triplet states, TDDFT calculations were carried out with the same functional and basis sets. All calculations were performed in DCM solutions using the IEF-PCM approach[136-138] and the Gaussian 09 package.[131]

4.2.7 Appendix

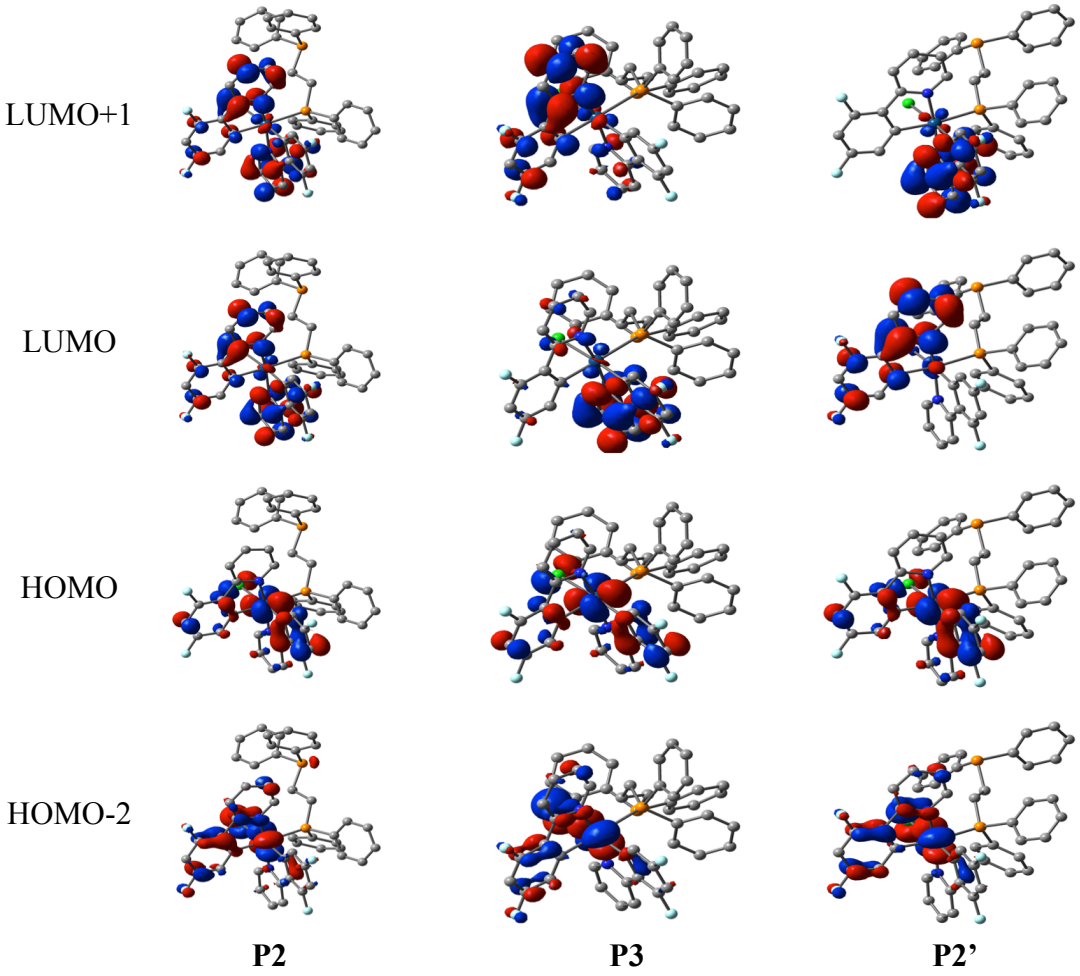

Figure A2.1. Selected frontier MOs of the investigated complexes.

5. Tuning the photophysics of monocyclometalated Ir(III) complexes

5.1 Introduction

With the goal to achieve different emission colors across the visible spectrum, the group of Prof. Laskar synthesized a series of monocyclometalated Ir(III) complexes with the [Ir(C^N)(Px)$_2$(Cl)(H)] general formula.[151] Different cyclometalating ligands (C^N) and modifications on axial phosphines (Px) were investigated (Figure 2.19). Starting from complex **P3** with C^N=ppy and Px=PPh$_3$, two closely related complexes were subsequently synthesized. Namely **P3F**, in which the ppy ligand is fluorinated (F$_2$ppy) and **P1**, in which two phenyl groups of the triphenylphosphine ligand are replaced by methyl units. In a second set of complexes with P$_x$=PPh$_3$ (**N1-N4**), the cyclometalating ligand was varied with increasing π-conjugation.

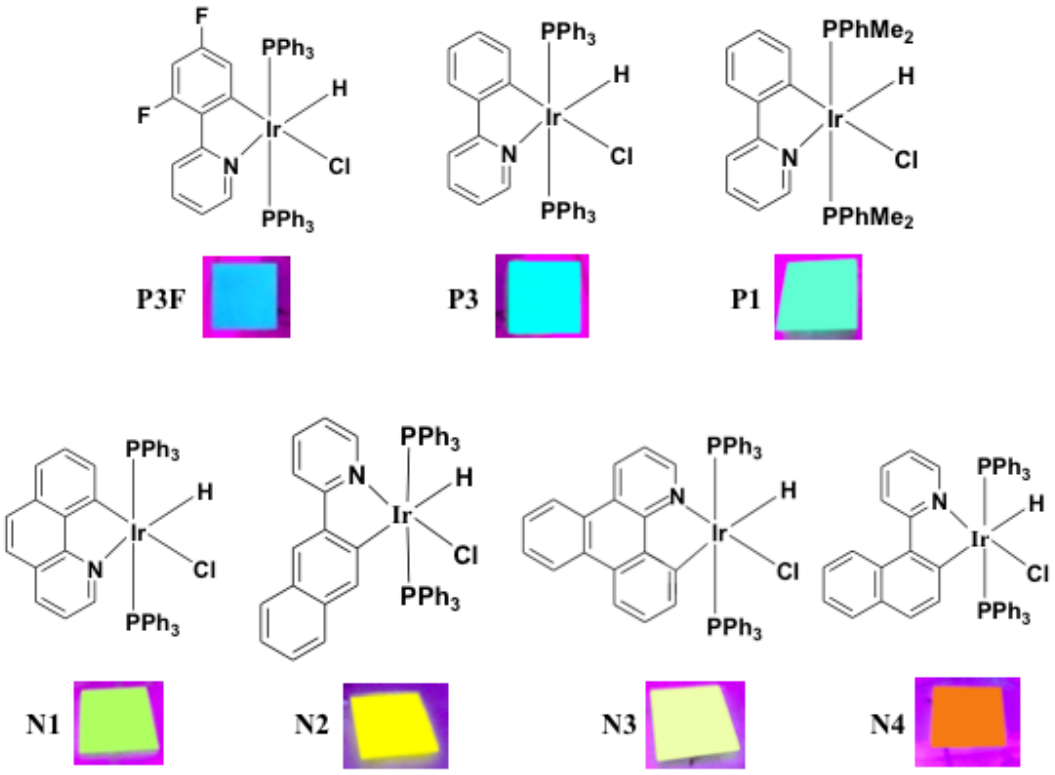

Figure 2.19 Investigated complexes together with their thin film emission color.

All the studied complexes exhibit weak phosphorescent emission in solution that becomes rather strong upon aggregation. i.e they are AIE active. Experiments were performed in solution with different THF/water fractions, inducing a gradual formation of molecular aggregates. Moreover, PL quantum yield measurements confirmed AIE in thin-film

samples. The resemblance of the recorded emission spectra in dilute solutions and in the solid state ruled out the possibility of AIE originated from an emitting state of different electronic nature. To confirm our initial intuition that the observed AIE might be due to the presence of the more or less freely "rotating" phenylphosphine ligands, additional experiments were carried out. A gradual increase of the emission intensity for all the complexes dissolved in THF was observed on increasing the concentration of a viscous solvent (polyethylene glycol). This observation suggests that the hindrance of the rotationally active part of the complexes on increasing the viscosity of the solution may be responsible for the increase of luminescence intensity in aggregated samples. Therefore, the RIR mechanism seems to be a plausible explanation for the AIE of these complexes. This is further supported by the measured decrease in the PL quantum yields (Table 2.8) of complexes **P3F** and **P3** when phenyl rings from the triphenylphosphine ligands are systematically replaced by methyl groups. Therefore, the phenyl rings certainly play an important role in the non-radiative decay pathway, which is blocked in the solid state leading to the observed AIE.

Table 2.8 Solid-state phosphorescence quantum efficiencies (in %) recorded using an integrating sphere, taken from reference 151.

	C^N	
Px	F_2ppy	ppy
PPh_3	41	55
PPh_2Me	11	9
$PPhMe_2$	11	7

A very interesting application was reported by our colleagues by micellar encapsulation of the **P3** AIE active iridium complex. The poor water solubility of the studied Ir(III) complexes limits their practical application, since water solubility is required for biological labeling applications. To overcome this problem, our collaborators encapsulated the AIE active **P3** molecule inside polymeric micelles. An important increase in the emission intensity was detected when the iridium complexes aggregated in the hydrophobic core of the micelles. It is important to point out that these colloidal luminescent particles allow transferring of the insoluble complexes into water, that could then be applied as potential non-toxic bio-imaging probes. In particular, the micellar nanoparticles that encapsulated the AIE-active **P3** complex were used as in vitro cellular imaging probes for biomedical applications.

Our goal herein was to reveal how the MLCT character of the lowest excited states is modified according to the presence of different ligands. We also focussed our attention to understand the variation of emission color among the complexes.

5.2 Ground state geometries

A slightly distorted octahedral geometry is obtained for all the calculated Ir(III) complexes, in which the P-Ir-P angle is approximately 170º, while the Cl-Ir-H and the N-Ir-C angle from the cyclometalating ligand are ~90º and 80º respectively. In general, the ground state optimized structures are similar for all the investigated complexes (Appendix, Table A2.1). However, there are some differences in the Ir-X bond lengths in the equatorial plane. These differences can be rationalized by considering the different σ-donor ability of the C and N atoms in the cyclometalating ligand and the different *trans* effect induced by the H^- and Cl^- ligands. The *trans* influence is responsible for the increase of the Ir-Cl and Ir-N bond lengths by ~0.10 Å and ~0.15 Å and the decrease of the Ir-H and Ir-C bond lengths by ~0.07 Å and ~0.10 Å, respectively in the **P3F**, **P3**, **P1**, and **N1** set of complexes as compared to **N2**, **N3,** and **N4**. On the other hand, among all the calculated complexes, the Ir-P distance is practically constant. Therefore, chemical modifications on the axial phenylphosphine ligands do not greatly influence the coordination environment of the iridium atom, which is mainly affected by the relative *cis* or *trans* disposition of the ligands coordinated in the equatorial plane.

The optimized structures of **P3F**, **P1** and **N1** are very close to the corresponding X-ray geometries, except for the Ir-Cl bond length, which is overestimated by ~0.1 Å in the calculations. This is probably due to weak interactions present in the crystal in which the chloride ligand is involved. Remarkably, the main difference between crystallographic coordinates and geometries obtained from quantum chemical calculations are found in the disposition of the phenyl rings in the phosphine ligands, which can be related to the expected greater molecular flexibility of these ligands in solution (Appendix, Figure A2.2).

5.3 Frontier molecular orbitals

The two lowest unoccupied MOs are very similar for all the calculated molecules and basically correspond to π*-type orbitals of the cyclometalating ligand (Figure 2.20), except for the LUMO+1 orbital of **N4**, for which there is a small participation of a d orbital of the iridium atom and some π* contribution of the pyridine ring of the cyclometalating ligand

and the two phenyl rings belonging to the phosphine that lie just above and below it. In the case of **N4** however, the LUMO+1 has a significant participation in the low-lying excited states. On the contrary, there is a clear distinction between the occupied orbitals of complexes **P3F**, **P3**, **P1**, **N1** and those with a more extended conjugated cyclometalating ligand, that is, complexes **N2**, **N3** and **N4**. While the HOMO in both cases has an important π contribution of the non-pyridine rings of the cyclometalating ligand, the participation of a d orbital of the iridium atom is smaller for the latter, while for the former there is a non-negligible p-orbital contribution of the chlorine atom. Additionally, the HOMO-1 consists in a p orbital of the chlorine atom and participation of a d orbital of the metal center, and for complexes **N2**, **N3** and **N4** there is an important admixture with the equatorial hydrogen and the carbon atom of the cyclometalating ligand to which the iridium is bonded.

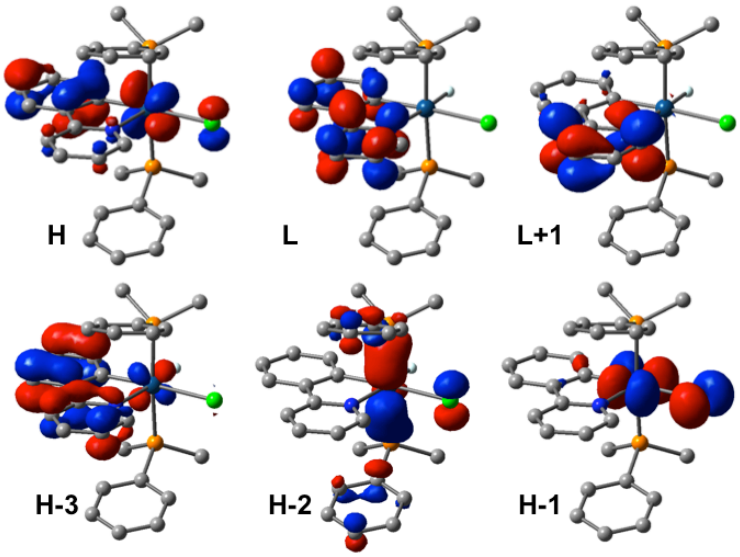

Figure 2.20 Frontier MOs for complex **P1**. Hydrogen atoms on the ligands are not shown for clarity.

For complexes **P3F**, **P3**, **P1**, and **N1** the HOMO-2 has contributions from a p orbital of the chlorine atom, a d orbital of the iridium center and a little participation of the phosphorus atoms, while the HOMO-3 is basically a π orbital of the cyclometalating ligand with little contribution of metal centered orbitals. On the other hand, the HOMO-2 and HOMO-3 of complexes **N2**, **N3**, and **N4** consist in different degrees of mixture of a π orbital of the cyclometalating ligand, together with d and p contributions from the iridium and chlorine atoms, respectively. Except for the HOMO-1, all other mentioned orbitals have a notable participation in the low-lying electronic states.

In order to understand the relative positions of the absorption bands in the UV/Vis absorption spectra, it is interesting to discuss the energy differences between the frontier molecular orbitals, specially the HOMO and LUMO, which are involved in the lowest optical transition. Since the phosphine ligands are not involved in the aforementioned orbitals, the computed HOMO-LUMO gaps (Table 2.9) for complexes **P3** and **P1**, for which the only difference is indeed the phosphine, are practically identical. On the other hand, the substitution of the cyclometalating ligand with fluorine atoms in complex **P3F** gives rise to an increase of the HOMO-LUMO gap as compared to **P3**, because of the greater stabilization of the HOMO relative to the LUMO. Complexes **N1, N2**, **N3** and **N4** display a smaller HOMO-LUMO gap compared to the **P1**, **P3** and **P3F** complexes. Extension of the cyclometalating ligand's π-conjugation results in a systematic destabilization and stabilization of the HOMO and LUMO energies, respectively.

Table 2.9 HOMO-LUMO gap for the investigated complexes and relative value with respect to **P3**. All values are given in eV.

	P3F	**P3**	**P1**	**N1**	**N2**	**N3**	**N4**
Δ(H,L)	4.14	4.01	4.05	3.70	3.55	3.76	3.55
Δrel	0.13	0.00	0.04	-0.31	-0.46	-0.25	-0.46

5.4 Absorption

The experimental UV/Vis absorption spectrum in DCM for the investigated complexes[151] has a moderately intense band in the range of 300-450 nm, with some distinguishable peaks. As it is shown in Table 2.10, the lowest energy allowed electronic transition corresponds to the promotion of an electron from the HOMO to the LUMO in all the calculated molecules, yielding a mixture of MLCT, LLCT (p(Cl)→π*) and LC character of the excitation, since electron density is reallocated from the iridium, chlorine (for complexes **P3F**, **P3**, **P1** and **N1**), and the cyclometalating ligand to the cyclometalating ligand itself. Hence, the energy of this electronic transition displays greatest variations between those complexes in which the cyclometalating ligand is modified, that is, in complexes **N1-4**. Since complexes **P3** and **P1** only differ in the phosphine ligand, their transition energies to S_1 are almost identical. On the other hand, fluorine substitution in **P3F** results in a ~0.1 eV increase in the excitation energy. The variations in the excitation energy to S_1 between the different complexes follow the same trend as the HOMO-LUMO gap previously discussed (Table 2.9), and correlate well with the experimental absorption maxima (Table 2.10).

Table 2.10 Comparison between experimental absorption maxima λ_{exp} and computed transition energies λ_{calc} (in nm) and orbital composition (%) of the lowest excited bright singlet and triplet states for the studied complexes.[(a)]

Complex	State	λ_{exp}	λ_{calc}	H→L	H-n→L[(b)]
P3F	T_1	430	433	56	25
	S_1	369	360	97	
P3F	T_1	445	451	68	19
	S_1	381	372	97	
P1	T_1	430	445	68	21
	S_1	384	368	97	
N1	T_2	451	442	45	
	S_1	407	400	94	
N2	T_1	-	553	63	16
	S_1	424	418	94	
N3	T_1	-	465	28	17
	S_2	400	393	95	
N4	T_1	-	567	84	
	S_1	423	419	84	

[(a)]Results for higher singlet and triplet states can be found in the Appendix (Table A2.2). [(b)]Cumulative contribution from H-n with $1 \leq n \leq 3$.

Our calculations suggest that the longest wavelength, weak intensity tail for complexes **P3F**, **P3**, **P1**, and **N1** corresponds to spin-forbidden transitions to low-lying triplet states, resulting mainly from HOMO and HOMO-3 to LUMO electronic excitations (Table 2.10). In addition, the calculations nicely reproduce the position of the peaks in the high-energy region, above S_1 (Appendix, Table A2.2). These excited singlet states are obtained as the combination of several electronic promotions from occupied to unoccupied orbitals. As it may be noticed, the same happens for the description of the two lowest triplet states. Overall, computed transition frequencies to the low-lying states of these complexes are in very good agreement with experimental absorption peaks in DCM solution.

5.5 Emission

In order to gain more insight into the nature of the photoemission, the lowest triplet state was optimized in solution within the unrestricted DFT framework. The two unpaired electrons of this state were found to be in spin-orbitals very much resembling the HOMO and the LUMO of the singlet ground state. As a result, the coordination environment of the complexes upon populating the T_1 state is mainly affected by a decrease of the Ir-Cl and Ir-C bond lengths (by a maximum of ~0.04 Å) due to the different HOMO/LUMO bonding/ anti-bonding interactions of the axial π system (Appendix, Table A2.3).

The emission spectra of complexes **P3F**, **P3**, **P1**, **N1**, and **N2** shows structured profiles (Appendix, Figure A2.3). This suggests that the emitting triplet states of **P3F**, **P3**, **P1**, **N1**, and **N2** have a lower MLCT character and larger LC contributions compared to **N3** and **N4**, which exhibit broad emission bands with no vibrationally resolved peaks. Furthermore, these complexes do not show solvatochromic effects, i.e., the emission spectra remain practically unchanged irrespective of the polarity of the solvent.

Our calculations underestimate the energy of the electronic transition from the lowest triplet state to the ground state by 0.4-0.5 eV. Nevertheless, the relative energy shifts exhibited between complexes are accurately reproduced (Table 2.11). In general, the computed vertical T_1 de-excitation energies follow the same trends as the ones obtained for the calculated vertical energies to S_1 and T_1 and HOMO-LUMO gaps at the FC region. Therefore, the changes in the emission color can be traced back to the effect that the different ligands have on the HOMO and LUMO energies. By comparing the calculated emission energy with the highest energy peak in the experimental spectrum, **P3F** presents an 0.1 eV blue-shifted emission compared to **P3** because of its wide HOMO-LUMO gap due to great stabilization of the HOMO upon fluorination of the cyclometalating ligand. Modifications on the phosphine ligands in **P1** have a minor impact in the emission color, since they are not involved in the electronic transition. When moving across complexes **N1**, **N2**, and **N4** the emission color relative to **P3** is red-shifted due to greater electronic delocalization on the cyclometalating ligand. The red to blue-shift in the emission color predicted by the calculations is nicely seen in the thin-film sample images of Figure 2.19. In particular, these images illustrate how the modification of the degree of conjugation in the cyclometalating ligands can be used to fine tune the emission color at will.

Table 2.11 Comparison between experimental and calculated emission energies of the investigated complexes. The experimental λ_{em} values correspond to the two peaks of the emission spectrum, while the experimental ΔE values correspond to the highest energy peak. The relative emission energies (Δ_{rel}) with respect to **P3** are also given.

		P3F	**P3**	**P1**	**N1**	**N2**	**N4**
λ_{em} / nm	calc.	537	563	558	636	714	773
	exp.	451, 476	468, 499	468, 497	512, 548	543, 585	589
ΔE / eV	calc.	2.31	2.20	2.22	1.95	1.74	1.60
	exp.	2.75	2.65	2.65	2.42	2.28	2.11
Δ_{rel} / eV	calc.	0.11	0.00	0.02	-0.25	-0.47	-0.60
	exp.	0.10	0.00	0.00	-0.23	-0.37	-0.54

5.6 Conclusions

Controlled tuning of the emission wavelength in monocyclometalated Ir(III) complexes was accomplished throughout the visible range by the introduction of systematic changes in the cyclometalating ligands. Changes in the emission color are minor when the phosphine ligands are modified, since they do not participate in the MOs involved in the electronic transitions. A mixed MLCT/LC/LLCT character is assigned to the emitting state of **P3F**, **P3**, and **P1**, while that of **N1**, **N2**, **N3**, and **N4** is predominantly of MLCT character. The larger admixture of LC contributions is responsible for the observed structured emission profile of **P3F**, **P3**, and **P1**, assigned to vibronic progressions related to vibration modes on the cyclometalating ligand. The computed absorption energies are in very good agreement with the experimental values, while the emission ones are somewhat underestimated. Nevertheless, the change in the emission color among the complexes is nicely reproduced by our calculations, and they can be traced back to the differences in the frontier molecular orbitals.

5.7 Computational details

Geometric optimizations for the investigated complexes in their ground and lowest triplet states were carried out using quantum chemical calculations based on the DFT with a reparametrization of the GGA B97 functional with an empirical dispersion correction, i.e., the B97-D functional[113]. A basis set of double-ζ quality (LANL2DZ) and the ECP of Hay and Wadt[120] were used for iridium. For all the other atoms, standard all-electron 6-31+G(d) basis sets were used. Electronic transitions to low-lying singlet and triplet states were calculated using the B3LYP hybrid functional[111,112] and the same basis sets. Solvation effects in DCM were included by the IEF–PCM.[136-138] The Gaussian 09 package[131] was used for all these calculations.

5.8 Appendix

Table A2.1 Selected bond lengths and angles for the ground state optimized geometries.

	Bond distances, Å					Angles (º)		
Complex	Ir-N	Ir-C	Ir-Cl	Ir-H	Ir-P[(a)]	N-Ir-C	Cl-Ir-H	P-Ir-P
P3F	2.193	2.007	2.593	1.600	2.345	79.1	91.5	171.1
P3	2.201	2.014	2.612	1.601	2.339	79.1	92.4	171.3
P1	2.189	2.013	2.618	1.611	2.325	79.1	90.9	175.1
N1	2.220	2.018	2.604	1.597	2.340	79.9	92.4	172.5
N2	2.050	2.106	2.484	1.673	2.339	80.0	91.7	170.5
N3	2.047	2.111	2.485	1.670	2.340	80.0	91.3	171.4
N4	2.043	2.101	2.490	1.672	2.340	79.1	91.1	170.2
P3F crystal	2.160	1.998	2.464	-	2.324	79.0	-	171.1
P1 crystal	2.142	2.009	2.504	-	2.300	79.5	-	169.1
N1 crystal	2.153	2.021	2.475	-	2.324	80.3	-	169.7

[(a)]Average value of the two Ir-X distances in each compound.

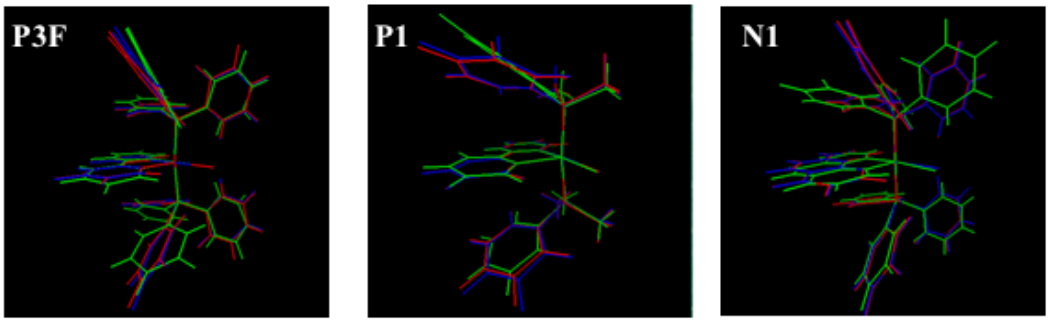

Figure A2.2 Geometry comparison between the X-ray crystal structure (green), and the ground state (blue) and lowest triplet (red) optimized geometries of complexes **P3F**, **P1,** and **N1**.

Table A2.2 Comparison between experimental absorption maxima (λ_{exp}) and extinction coefficients ($\varepsilon \times 10^4$ in $M^{-1}cm^{-1}$) and the computed transition energies (λ_{calc}) and oscillator strengths (*f*) for the studied complexes in DCM solution.

Complex	λ_{exp} / nm	ε	State	ΔE / eV (nm)	*f*	Assignaments
P3F	430	0.05	T_1	2.86 (433)	-	H→L (56%), H-3→L (25%)
	-	-	T_2	3.38 (367)	-	H→L (36%), H-3→L (42%)
	369	1.5	S_1	3.44 (360)	0.05	H→L (97%)
	338	2.3	S_5	4.00 (310)	0.04	H-2→L (66%), H→L+1 (20%), H-3→L (11%)
P3	445	0.025	T_1	2.75 (451)	-	H→L (68%), H-3→L (19%)
	-	-	T_2	3.25 (381)	-	H→L (26%), H-3→L (50%)
	381	0.51	S_1	3.33 (372)	0.07	H→L (97%)
	343	0.65	S_5	3.97 (312)	0.03	H-2→L (89%)
P1	430	0.02	T_1	2.78 (445)	-	H→L (68%), H-3→L (21%)
	-	-	T_2	3.29 (376)	-	H→L (27%), H-3→L (51%)
	384	2.7	S_1	3.37 (368)	0.06	H→L (97%)
	349	3.6	S_4	3.91 (317)	0.02	H-2→L (16%), H→L+1 (80%)
N1	-	-	T_1	2.51 (494)	-	H→L (47%), H→L+1 (19%), H-2→L (13%)
	451	0.04	T_2	2.80 (442)	-	H→L (45%), H→L+1 (37%)
	407	0.71	S_1	3.10 (400)	0.06	H→L (94%)
N2	-	-	T_1	2.24 (553)	-	H→L (63%), H-2→L (16%)
	-	-	T_2	2.79 (444)	-	H→L (24%), H-2→L (62%)
	424	0.59	S_1	2.97 (418)	0.02	H→L (94%)
	336	5.1	S_3	3.49 (356)	0.21	H-2→L (86%)
	319	5.5	S_8	3.79 (328)	0.11	H-3→L (87%)
N3	-	-	T_1	2.67 (465)	-	H→L (28%), H-2→L (17%), H-3→L+1 (10%), H→L+3 (10%)
	-	-	T_2	2.80 (442)	-	H→L (58%), H→L+1 (13%), H-2→L (13%)
	400	0.27	S_2	3.15 (393)	0.04	H→L (95%)
	331	1.86	S_5	3.62 (342)	0.09	H-1→L+1 (43%), H-2→L (29%), H→L+1 (22%)
	331	1.86	S_6	3.63 (342)	0.08	H-1→L+1 (51%), H-2→L (25%), H→L+1 (18%)
N4	-	-	T_1	2.18 (567)	-	H→L (84%)
	-	-	T_2	2.91 (425)	-	H-2→L (34%), H-1→L (33%)
	423	0.4	S_1	2.96 (419)	0.08	H→L (84%), H-1→L (12%)
	336	0.96	S_5	3.62 (343)	0.11	H-2→L (77%)

Table A2.3 Selected bond lengths and angles for the lowest triplet state optimized geometries of the investigated complexes.

	Bond distances, Å					Angles (º)		
Complex	Ir-N	Ir-C	Ir-Cl	Ir-H	Ir-P[(a)]	N-Ir-C	Cl-Ir-H	P-Ir-P
P3F	2.174	1.985	2.555	1.604	2.366	80.8	90.7	172.6
P3	2.188	1.980	2.576	1.603	2.363	81.1	91.7	172.9
P1	2.181	1.978	2.590	1.613	2.348	81.2	90.9	176.3
N1	2.224	1.981	2.573	1.598	2.354	79.7	91.6	173.1
N2	2.048	2.081	2.495	1.675	2.342	79.9	91.6	170.3
N4	2.065	2.093	2.456	1.665	2.352	79.2	95.3	172.2

[(a)] Average value of the two Ir-X distances in each compound.

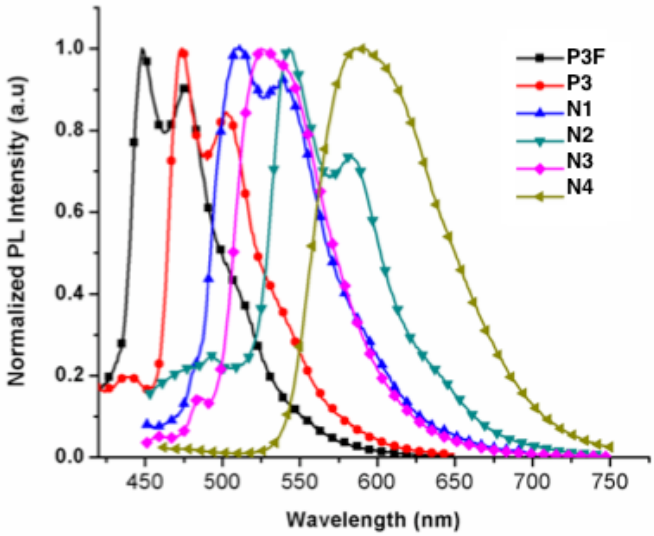

Figure A2.3 Normalized PL spectra of the investigated complexes in 10^{-4} M DCM. Taken from reference 151.

6. Influence of the counterions on the AIE of Ir(III) complexes

6.1 Introduction

Inspired by the role of the axial triphenylphosphine ligands in the AIE properties of Ir(III) complexes previously investigated, our experimental collaborators successfully pursued the synthesis of a novel cationic complex,[152] i.e. $[Ir(bpy)H_2(PPh_3)_2]^+$ abbreviated as $[Ir(bpy)]^+$ in the following (Figure 2.21). Interestingly, the emission color of the solid state samples of $[Ir(bpy)]^+$ varied with the presence of different counterions (Cl^-, $N(CN)_2^-$, BF_4^-, and PF_6^-) in the crystal structure. The four compounds also exhibited a more or less pronounced AIE activity, both in aggregates formed in solution and in the obtained crystals. Moreover, the emission profile of the aggregates happened to be analogous to that recorded for the crystals. Therefore, a careful comparison of their crystal structures offered and excellent opportunity to try to shed some light on the effects of the crystal environment and intermolecular interactions on their AIE activity.

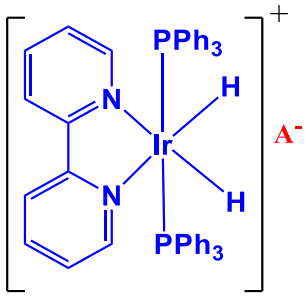

A = Cl, BF_4, PF_6, and $N(CN)_2$

Figure 2.21 Structure of [Ir(bpy)]A.

Further experiments with the [Ir(bpy)]Cl compound were carried out and an unusual photoluminescent behavior was detected. The emission color of the solid-state samples of [Ir(bpy)]Cl changed when it was put under stress, for instance, by mechanical grinding. As shown in Figure 2.22, the yellow powder sample of [Ir(bpy)]Cl switched to green after grinding and fuming with acetone. The sample then reversed to its original color by fuming with DCM/chloroform.

This phenomenon is of great interest since it can be exploited for several applications. In particular, smart solid-state luminescent materials responsive to external stimuli such as shearing, grinding, rubbing, solvent exposure, or temperature changes have recently received considerable attention.[153] The principal interest in these materials stems from their

ability to change their emission color as a response to an external perturbation that triggers changes in the network of weak non-covalent interactions between individual molecules in molecular aggregates.[154] These materials have an immense potentiality in various applications such as optical data recorders, mechanical sensors, security paper, deformation detectors, or storage devices.[155-157] In order to enhance the existing capabilities and guide the design of new improved materials it is, however, necessary to develop a deep understanding of the physical nature of the mechanisms involved in their response to external perturbations.

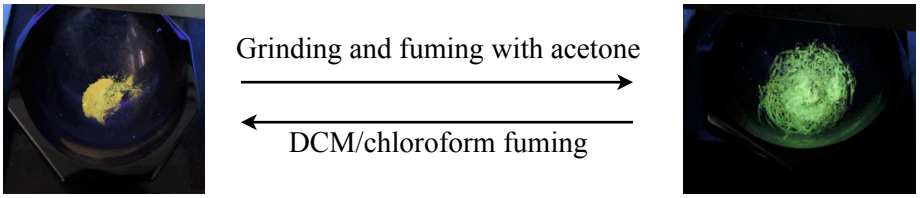

Figure 2.22 Color change of solid state samples of [Ir(bpy)]Cl. Taken from reference 152.

The complete understanding of this phenomenon at a molecular level is very challenging, but the analysis of the crystal packing was a good initial step to learn what kind of intermolecular interactions are present in the solid state. Herein our goal was to characterize the electronic structure of $[Ir(bpy)]^+$, and by following an heuristic approach, put forward the factors that are relevant for the AIE observed for the studied compounds.

6.2 Molecular and crystal structure

The principal building block in the [Ir(bpy)]A crystal structures is the cationic $[Ir(bpy)]^+$ complex, that shows a distorted octahedral coordination sphere around the iridium atom (Figure 2.23), as confirmed by the Single Crystal X-ray Diffraction (SC-XRD) analysis obtained for the [Ir(bpy)]Cl and $[Ir(bpy)]PF_6$ crystals. A bipyridine (bpy) ligand, along with two hydride ligands, lie on the equatorial plane, while the axial positions are occupied by two triphenylphosphine ligands. The chiral propeller-like arrangement of the phenyl rings in the triphenylphosphine ligand allows the possibility of having enantiomeric molecules. Indeed, the two possible enantiomers are present in the two studied crystal structures.

The principal geometrical parameters of the Ir coordination sphere for the two experimental X-ray diffraction structures reveal that both geometries are rather similar (Appendix, Table A2.4). The main departure from a perfect octahedral environment for the

iridium atom corresponds to the off-axis distortion of the two phosphorus atoms, with P−Ir−P angles about 15° smaller than in a perfect octahedron (180°) towards the two hydride ligands side. Bond distances between the central metal atom and the coordinating atoms on the ligands are very similar in the two crystal structures, except for one of the Ir −N bonds, which is approximately 0.05 Å longer in the [Ir(bpy)]PF_6 crystal. This is because the bpy ligand in both structures has some differences in the adopted geometry, probably due to intermolecular forces induced by the bulky phenylphosphine ligands. Nevertheless, these differences do not have a great impact on the electronic structure of the cation, as suggested by the calculations discussed below. The major differences between the two geometries essentially correspond to the relative disposition of the phosphine ligands (Figure 2.23c). In the [Ir(bpy)]PF_6 crystal, the two sets of phenyl rings of the two phosphine groups in a *trans* disposition are closer to an eclipsed conformation than in the [Ir(bpy)]Cl case, as indicated by their C−P−P−C dihedral angles (A2.4). In close relation to this distortion, we notice that the molecular geometries for the two crystals exhibit different degrees of rotation for some of the phenyl rings.

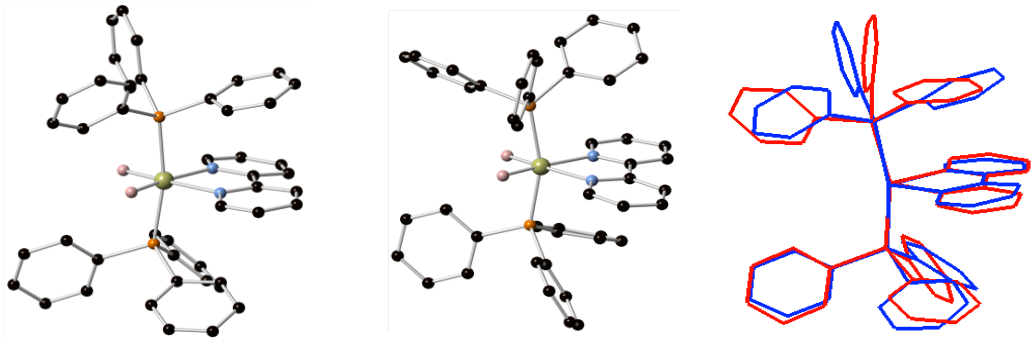

(a) (b) (c)

Figure 2.23 Structures of $[Ir(bpy)]^+$ in the (a) Cl^- and (b) PF_6^- crystals with the optimized hydride ligands and (c) the superposition of their most overlapping enantiomers. Hydrogen atoms on the ligands are not shown for the sake of clarity.

In the unit cell of both crystals, there are four cations and four counterions, but the [Ir(bpy)]PF_6 crystal contains six additional DCM molecules. The four cations in the unit cell are symmetry equivalent, although, in the two crystals, they appear as two pairs of enantiomers. In both cases, the cations are arranged in chains along the *a* direction. A more detailed discussion of their disposition along these chains will be given later on, since these are suggested to play a role in the observed AIE effect.

6.3 Photophysical properties

The qualitative MO diagram in Figure 2.24 summarizes the nature of the $[Ir(bpy)]^+$ frontier molecular orbitals obtained for the cation's geometry in the Cl^- crystal. Due to the loss of octahedral symmetry, the metal-centered t_{2g}- and e_g-type orbitals, shown in red in the diagram, mix significantly with ligand-centered orbitals. Since the P−Ir−P angle is smaller than 180°, it allows the interaction between metal d-orbitals and the phosphine lone pairs, inducing an energy splitting of the t_{2g} orbitals by destabilizing the d_{xz} orbital with respect to the d_{xy} and d_{yz} orbitals, which exhibit a smaller energy separation between them.[158] As a result, the HOMO in the present compounds is mainly an iridium d_{xz} orbital as shown in the diagram, while the other two t_{2g} orbitals lie well below in energy, with several π-type orbitals of the phenyl rings of the phosphines lying in between them. Due to their M-L antibonding character, the e_g-type orbitals are strongly destabilized and appear rather high in energy with a significant mixture with ligand orbitals. A large number of ligand-centered π*-type MOs, either from the phenyl rings of the phosphines or from the bpy ligand, appear between the t_{2g} and the e_g MOs, with the LUMO being a bpy-centered π*-type orbital. The electron density distributions associated with the HOMO and the LUMO are virtually identical for the cation in the two crystal structures (Appendix, Figure A2.4).

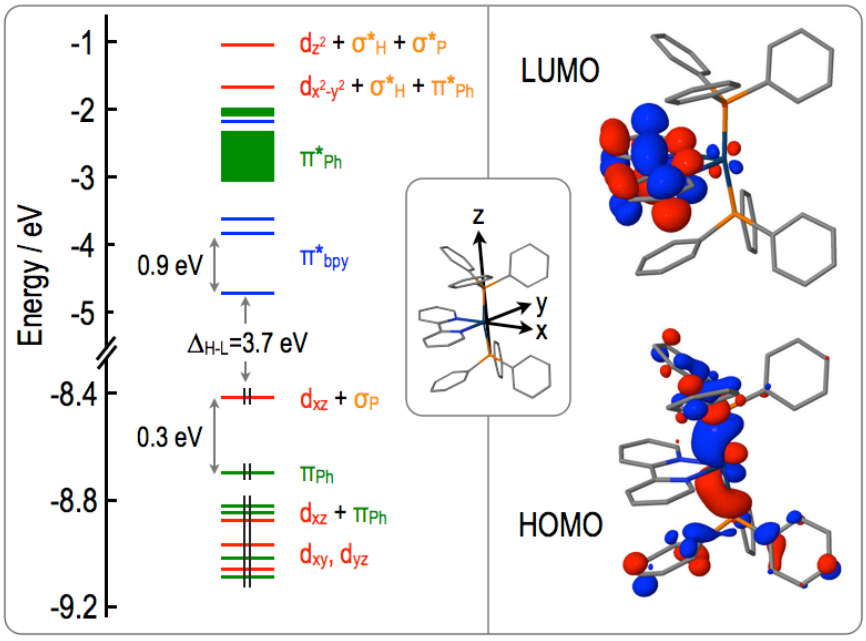

Figure 2.24 MO energy diagram of $[Ir(bpy)]^+$ in the [Ir(bpy)]Cl crystal's geometry and corresponding HOMO and LUMO. Color code: red for d-block orbitals of the iridium atom; green for π- and π*- type orbitals of the phenyl rings of the phosphine ligands; blue for π*- type orbitals of the bpy ligand; and orange for σ-type orbitals of the phosphorus's lone pairs and the hydrogen atoms bonded directly to iridium.

The absorption and emission spectra at room temperature for all four [Ir(bpy)]A complexes in DCM solution are very similar (Appendix, Figure A2.5). This is not surprising since the presence of different counterions is not expected to influence the absorption or emission of the individual cationic complexes. The absorption of the [Ir(bpy)]A crystals are very similar to those in DCM solution, indicating that in the solid state, the absorption is due to excited states localized on individual cations. The emission spectra in the solid state however present differences compared to the spectra in DCM solution (Figure 2.25). Although the emission bands cover the same visible range (450-650 nm) in both cases, the emission band of the crystals presents a much more structured profile.

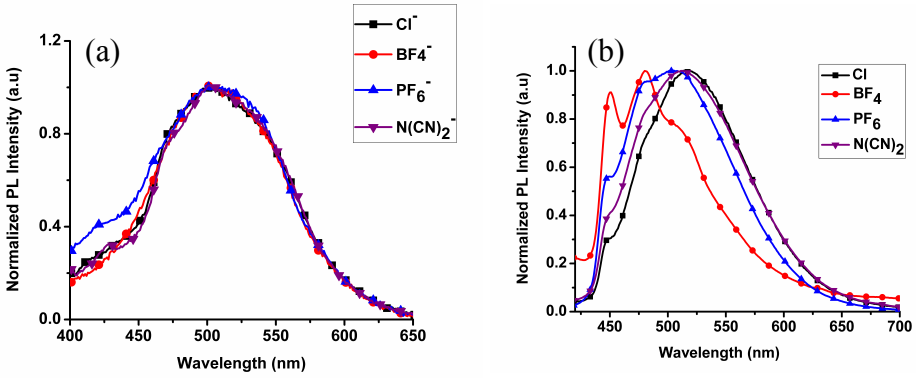

Figure 2.25 Emission spectra (λ_{exc}=385 nm) for [Ir(bpy)]A [A^- = Cl^-, BF_4^-, PF_6^-, $N(CN)_2^-$] compounds (a) $1 \cdot 10^{-5}$ M solutions in DCM and (b) crystals. Taken from reference 152.

The computed energy for the cation's LUMO is very similar in the two compounds for which the crystal structure could be resolved, i.e., [Ir(bpy)]Cl and [Ir(bpy)]PF_6, while the HOMO is 0.15 eV lower in energy in the cation of the [Ir(bpy)]PF_6 crystal (Table 2.12), leading to a 0.1 eV smaller HOMO−LUMO gap for the cation crystalized with PF_6^-. This is indeed the difference between the calculated excitation energies to the lowest excited triplet state of the cation, which are computed at 454 and 433 nm for [Ir(bpy)]PF_6 and [Ir(bpy)]Cl, respectively. The lowest singlet and triplet excited states have a predominant HOMO to LUMO contribution (>80%), except for the lowest triplet state of the cation in the [Ir(bpy)]PF_6 crystal, for which the HOMO to LUMO contribution accounts for just 60% of the transition. The remaining contributions correspond to excitations to the LUMO from a d-type orbital of the iridium atom (~15%) or a π-type orbital of the bpy ligand (10%). Nevertheless, we can assign a strong metal-to-bpy charge transfer MLCT character to the S_1 and T_1 states. The vertical transition energies to the lowest excited singlet state are computed at 405 and 419 nm for the cation in the [Ir(bpy)]Cl and [Ir(bpy)]PF_6 crystals,

respectively, with a non-negligible oscillator strength (*f*=0.03), suggesting that they are responsible of the band observed just around 400 nm in the absorption spectra.

Table 2.12 HOMO and LUMO energies, HOMO-LUMO gap (Δ_{HL}) and vertical transition energies to the first excited singlet and triplet states for $[Ir(bpy)]^+$ in the Cl^- and PF_6^- crystal's geometry. All energies are in eV except values in parenthesis, which correspond to wavelengths in nm.

A^-	E_H	E_L	Δ_{HL}	ΔE	
				T_1	S_1
Cl^-	-8.42	-4.72	3.70	2.86 (433)	3.06 (405)
PF_6^-	-8.27	-4.68	3.59	2.73 (454)	2.96 (419)

It is worth to stress that the computed vertical energies to the lowest triplet state (T_1) cannot be directly compared to the phosphorescence emission spectra (Figure 2.25), since the present calculations neither account for geometry relaxation of the triplet state nor take into consideration vibronic coupling effects. The latter will be discussed below. Nevertheless, our calculations lead us to rule out intramolecular effects as responsible for the different phosphorescent emission properties observed for the [Ir(bpy)]Cl and $[Ir(bpy)]PF_6$ crystals.

A notable difference in the emission spectra of the two crystals is the much better resolution of the vibronic progression structure in the $[Ir(bpy)]PF_6$ case in comparison to the [Ir(bpy)]Cl one. Normal mode analysis for the cation at the minimum energy geometry for S_0 reveals that there are two breathing modes of the bpy ligand that may be assigned to the vibronic progression of the emission spectra. They consist of coupled asymmetric −symmetric and symmetric−symmetric breathing modes of each pyridine unit of the ligand (Figure 2.26), and their computed wavenumbers are 1030 and 1038 cm^{-1}, respectively, in fairly good agreement with the gap observed in the vibrational structure of the experimental spectra (1050 cm^{-1}). In the literature, the appearance of a resolved vibronic structure in the emission band of similar octahedral complexes has been related to a lower MLCT character and more LC π−π* type character of the excited state.[90] As discussed above, our computational study does not suggest that the nature of the emitting triplet state should differ significantly in the two crystals, so that we expect a similar MLCT character for the emission in both cases, and for this reason, we suggest that the differences observed in the vibronic structure of the cation in the two studied crystals are caused by different intermolecular interactions.

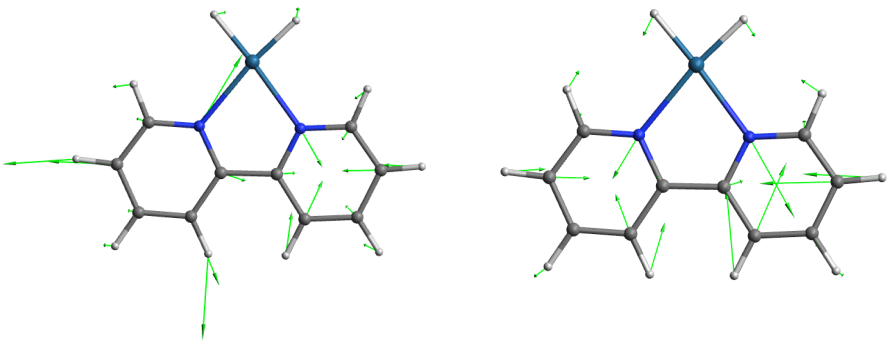

Figure 2.26 Displacement vectors corresponding to the coupled asymmetric-symmetric (left, 1030 cm^{-1}) and the symmetric-symmetric (right, 1038 cm^{-1}) breathing normal modes of vibration of the cation's optimized ground state. The phosphine ligands are omitted for the sake of clarity.

A difference in the color of the emitted light was observed for the four compounds (Figure 2.27). This is clearly seen in the chromaticity diagram. Among the four different crystals, the one with BF_4^- shows a more bluish color than the rest, which follow a trend in their emission colors, going from greenish to more yellow as we move from PF_6^- to $N(CN)_2^-$ and Cl^-. On the other hand, as expected, the color of the weak emission of all the complexes in DCM is very similar, suggesting that the differences arise from intermolecular interactions upon aggregation. The values of the *x*, *y* chromaticity coordinates are found in the Appendix (Table A2.5).

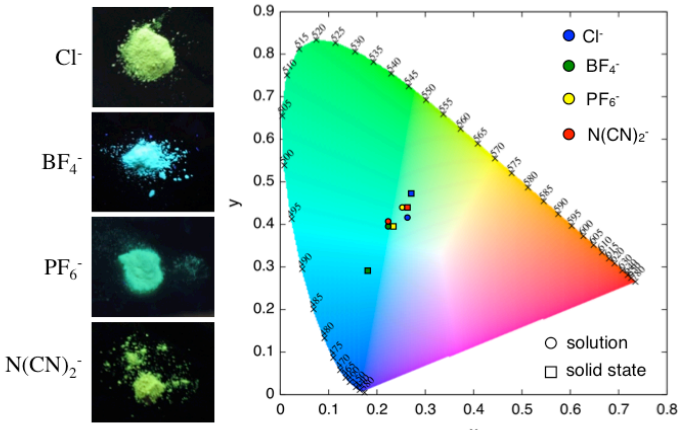

Figure 2.27 Left: Pictures of the emitting [Ir(bpy)]A crystals with different counterions: A=Cl^-, BF_4^-, PF_6^-, and $N(CN)_2^-$. Right: Chromaticity diagram (standard CIE (2°) 1931 color space[130] showing the color coordinates for the synthesized complexes in DCM and solid state.

6.4 Aggregation induced emission

All four investigated compounds present quite weak emission intensities when dissolved in common organic solvents, such as DCM, trichloromethane, or THF, whereas, in the solid state, either in aggregates or crystal samples, their phosphorescence emission becomes

much more intense. The absolute quantum yields for [Ir(bpy)]A compounds were estimated in powder form and found to be 20% (Cl^-), 34% (PF_6^-), 27% (BF_4^-), and 7% ($N(CN)_2^-$), respectively, while the relative quantum efficiencies in DCM solution (with respect the standard coumarin 153 dye dissolved in degassed ethanol, QE = 0.38) were very low for all cases, i.e. <1%. These facts support that all four compounds have an enhanced emission in the solid state.

Let us consider four possible sources for emission enhancement upon aggregation of the coordination complexes studied in this work:

(i) Packing forces in the aggregated state induce a reorganization of the coordination sphere of the metal atom large enough to change the nature of the emitting state. In this scenario, the change of the coordination sphere should enhance spin−orbit coupling in the emitting state as compared to that in diluted solutions with a result of an increase in the efficiency of the radiative deactivation pathway.

(ii) The aggregation process leads to strong intermolecular delocalization of the ground state, the emitting state, or both. This change will affect mainly the efficiency of the radiative pathway, although it is not easy to predict a priori if the emission intensity should increase or decrease since it will depend largely on the degree of delocalization of the emitting and the ground states and this degree of localization is difficult to describe from a computational point of view.

(iii) Packing forces in the aggregate state restrict the internal motion (RIM) in the cations, most importantly internal rotations and low frequency, large amplitude vibrations in the emitting molecule. The non-radiative deactivation process is well described by a first-order rate equation whose constant depends on two parameters: the strength of the coupling between the initial (emitting) state and the final (ground) state as well as the density of vibronic states of the ground state at the energy of the emitting state.[73,159-161] Considering that the presence of nearby molecules should not induce great changes in the coupling between the initial triplet and the final singlet state, the leading ingredient should be a decrease of the ground state's density of vibrational states. Steric congestion and interlocking of mobile parts would hinder large amplitude movements upon aggregation

with an increase in their vibrational frequencies and the associated decrease in the density of states, leading to a smaller rate constant for the non-radiative process.

(iv) Another possibility is that packing forces in the crystal could impose restrictions along the molecular geometry relaxation on the emitting state PES. Thus, the emitting state in the solid would be less distorted than in solution, leading to a decrease of the Franck-Condon factors, which would result in a decrease of the non-radiative decay rate constant.

Of course, more than one of these mechanisms may occur simultaneously in a same crystal, and discerning if there is a clear effect causing the enhancement of emission upon aggregation is extremely difficult. The present case, where we have the same emitting cation in different crystalline environments, offers an excellent opportunity to try to shed some light on these questions, although we will unfortunately have to limit our study to the comparison between crystals with the Cl^- and PF_6^- counterions, for which our experimental partners have been able to obtain X-ray resolved crystalline structures that will be considered to offer a proper model for the types of interactions that may be present in amorphous aggregates.

Since the principal features of the common $[Ir(bpy)]^+$ cation at the molecular level, both regarding its atomic and electronic structure, have already been discussed, and intramolecular effects do not seem to be responsible for the enhanced emission in the aggregate state, herein we will focus efforts towards understanding the role of the crystal structure. In particular, we will discuss the different molecular packing modes and their possible implications in the electronic structure of the crystals such as electronic delocalization and π-stacking.

6.4.1 Intrachain interactions

The $[Ir(bpy)]^+$ cations are packed into chains along the *a* direction of the crystals (Figure 2.28). The fundamental difference between the packing modes in the [Ir(bpy)]Cl and $[Ir(bpy)]PF_6$ crystals is the way in which the molecules dispose with respect to the chain direction. In the $[Ir(bpy)]PF_6$ crystal, the molecular P−Ir−P axis is oriented along the chain axis (Figure 2.28a), whereas it lies approximately perpendicular to it in the [Ir(bpy)]Cl crystal (Figure 2.28b). This difference in the orientation of the molecule with respect to the chain axis in the two cases may be important for the RIM mechanism since in the

[Ir(bpy)]PF_6 crystal, for which a relatively stronger AIE effect is observed, interlocking between the highly movable phenyl rings of neighboring molecules may effectively restrict their motion, while in the [Ir(bpy)]Cl crystal the interaction between neighbors is mainly between the rigid bpy and mobile triphenylphosphine fragments, which may result in a less effective RIM.

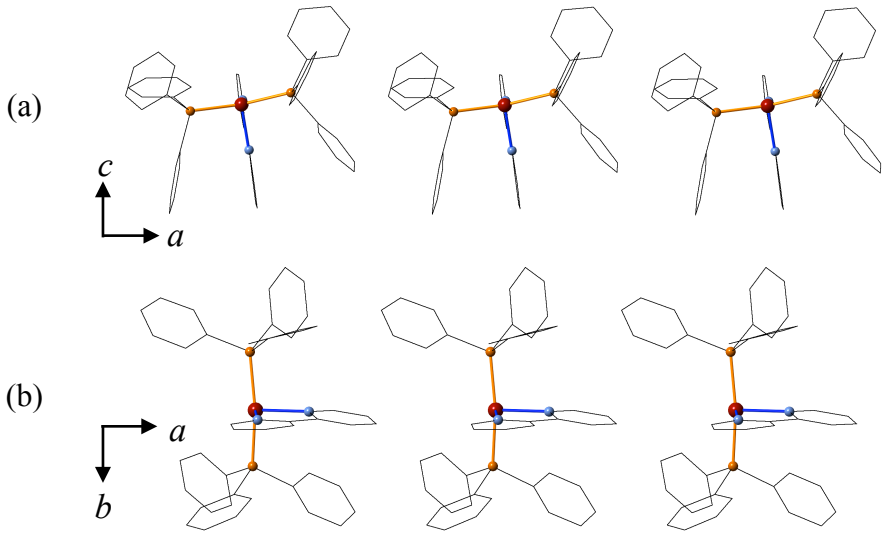

Figure 2.28 Chains in the (a) [Ir(bpy)]PF_6 and (b) [Ir(bpy)]Cl crystal structures. Color code: Ir−P bonds (orange) and Ir−N bonds (blue). Hydrogen atoms are not shown for the sake of clarity.

6.4.2 Interchain interactions

In the [Ir(bpy)]PF_6 crystal structure, shown in Figure 2.29a in a view along the direction of the chains, and taking the chain with the ligands colored in red as our reference, there are four chains of alternating PF_6^- counterions and DCM molecules forming a more or less square prism around the reference chain. There are also four additional cation chains that interact with the reference chain through the faces of this square prism. The neighboring chains at the left and right side of the central one in the figure are shifted along the chain direction with respect to the central chain so that the iridium atoms do not have the same coordinate along the axis parallel to the chain direction, in contrast to the neighboring chains shown above and below the central one in the figure, which lie on the same plane as the reference cation's chain.

In the [Ir(bpy)]Cl crystal, where anions are much smaller, each chain is surrounded by six neighboring cationic chains (Figure 2.29b) in an arrangement reminiscent of a compact hexagonal packing for perfect cylinders. In this case, the four neighboring chains shown to the left and the right of the central one are also shifted along the chain direction with respect to the central chain, while all the iridium atoms from chains represented above and

below lie in the same plane perpendicular to the *a* direction (*yz*-plane of Figure 2.29b). As it can be appreciated in the figure, since in this case the P-Ir-P axis is approximately perpendicular to the axis of the chains, molecules from different chains face each other mainly through the triphenylphosphine ligands. The Cl^- counterions occupy in this case the voids in the structure left between the rigid bpy ligands of one molecule and the hydride ligands on the neighboring one.

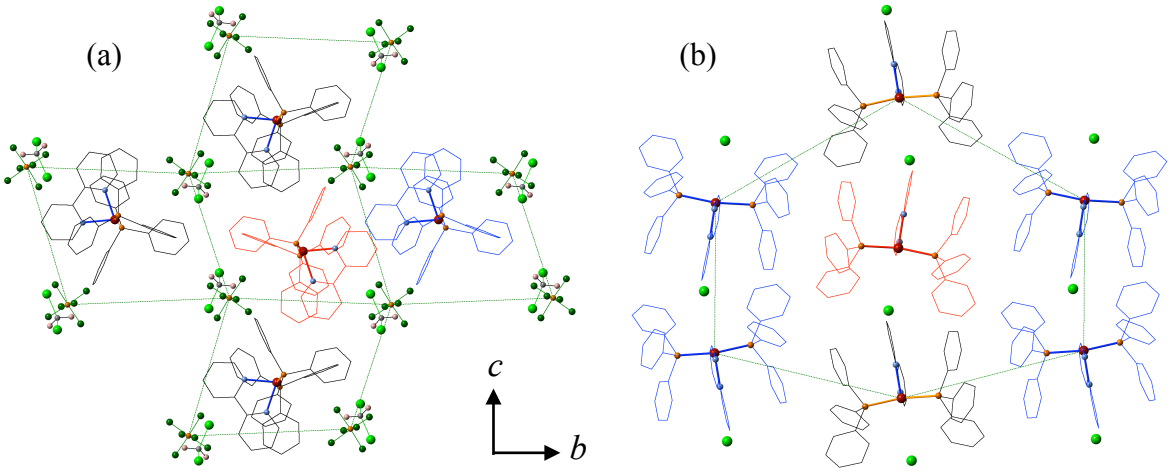

Figure 2.29 Interactions between chains that align along the *a* direction in the (a) [Ir(bpy)]PF_6 and (b) [Ir(bpy)]Cl crystal structures.

In both crystals, there are relevant interactions between some hydrogen atoms on the bpy ligand or the phenyl rings and the counterions. In the [Ir(bpy)]Cl crystal, there are short C−H···Cl contacts that range from 2.7 to 3.0 Å (Appendix, Figure A2.6), while, in the [Ir(bpy)]PF_6 crystal, there are C−H···F interactions that lie in the range of 2.4−3.1 Å (Appendix, Figure A2.7).

More important for our purposes, there are also significant interchain interactions in the two cases. In the [Ir(bpy)]PF_6 crystal, C−H···π interactions[162,163] are found between the cation chains highlighted in blue and red in Figure 2.29a. These interactions between the rigid bpy fragment and the mobile phenyl rings (Figure 2.30) may indeed play an important role in the restriction of the motion of these rotors. No other relevant interactions between the rigid fragments of the cations and their phenyl rings were found for the remaining chains of the [Ir(bpy)]PF_6 crystal. In contrast, for the [Ir(bpy)]Cl crystal, the C−H···π distances are much larger, excluding the possibility of this type of interactions to be relevant in this case. The principal interactions between the neighboring chains and the reference one, highlighted in red in the [Ir(bpy)]Cl crystal (Figure 2.29b), are with the

triphenylphosphine ligands on the chains highlighted in blue, in which interlocking of the phenyl rings would restrict motions in the solid state.

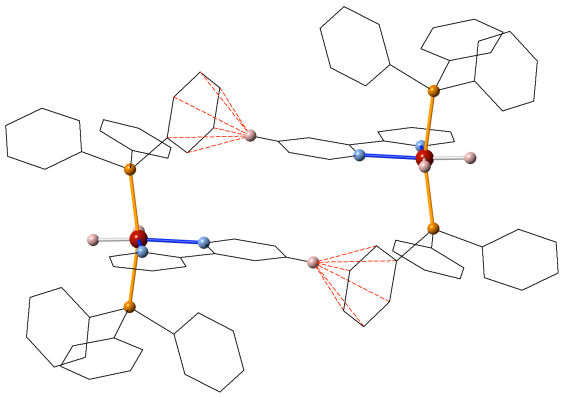

Figure 2.30 Interchain C−H···π interactions in the [Ir(bpy)]PF_6 crystal structure.

The only interactions between chains that may have significant electronic implications in their photophysical properties, that is, electronic delocalization and/or π-stacking interactions, are those between the chains highlighted in red and blue in the [Ir(bpy)]PF_6 crystal (Figure 2.29a), where the π-systems of their bpy ligands are susceptible to have a non-negligible overlap (Figure 2.31). The shortest C−C distance between the two coplanar bpy ligands is approximately 3.47 Å. Although the distance between the two ligands is short enough to be below the upper limit of what may be considered as a π-stacking interaction,[164,165] the vertical overlap between them is very poor, since the two ligands are quite displaced with respect to a complete alignment, limiting the overlap of π-type orbitals to just two carbon atoms on each bpy fragment. In light of this qualitative analysis, we can exclude significant electronic cooperative effects between neighboring complexes as the source of the different emission properties in the [Ir(bpy)]Cl and [Ir(bpy)]PF_6 crystals.

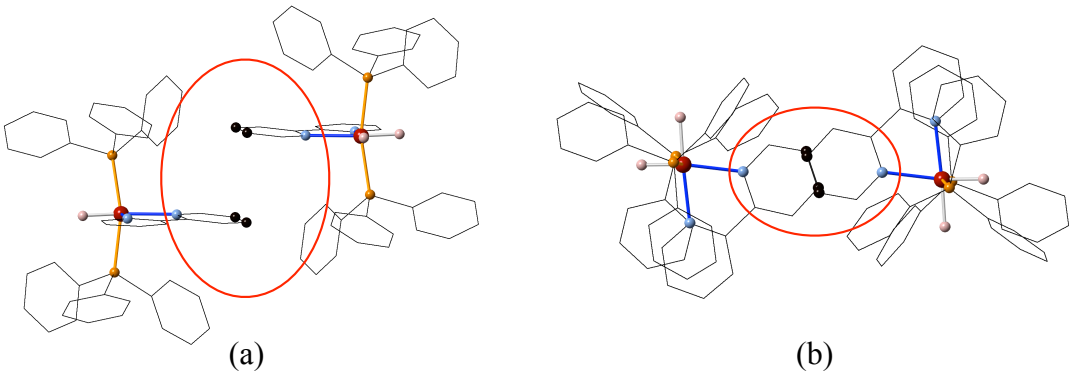

Figure 2.31 Side view (a) and top view (b) of a possible π-stacking interaction between two cations in the [Ir(bpy)]PF_6 crystal.

Summarizing, we arrive at the following conclusions: the involvement of the phenyl rings of the flexible triphenylphosphine ligand in intermolecular interactions is clearly recognizable in the two crystal structures, namely, as interlocking interactions between neighboring molecules in each chain in the [Ir(bpy)]PF_6 crystal with additional attractive C−H···π interactions between chains and interlocking of the phenyl rings of neighboring molecules on different chains in the [Ir(bpy)]Cl crystal. Since all other sources of possible AIE can be discarded from the comparative analysis of the crystal structures, it seems plausible to assume that the establishment of these intermolecular interactions will significantly hinder the molecular motion of the phenyl rotors in the aggregated state.

6.4.3 Molecular relaxation of the emitting state

The optimized geometry of the lowest excited triplet state of $[Ir(bpy)]^+$ has important differences with respect to the ground state optimized geometry and the molecular structure in the crystal. In fact, our calculations point toward a decrease of the P−Ir−P angle of approximately 20° upon excitation to the T_1 state (Table 2.13) due to the participation of the phosphorus's lone pair in the t_{2g}-type orbitals of the cation. This considerable geometry change in the MLCT triplet state may in fact have an important contribution to the factors responsible for the enhanced phosphorescence in the solid state since the triplet state in the aggregate may not be able to fully relax, as opposed to in solution. As a result, we might expect smaller Franck−Condon factors and a decrease of the non-radiative decay rate constant in the crystal with respect to in solution,[107] enhancing phosphorescence in the solid state.

Table 2.13 P−Ir−P Angles for different structures of $[Ir(bpy)]^+$.

structure	Cl^- crystal	PF_6^- crystal	S_0	T_1
P-Ir-P angle (º)	168	162	164	140

6.5 Conclusions

Our analysis shows that the lowest triplet state of the $[Ir(bpy)]^+$ cation originates from a HOMO-to-LUMO transition with a strong MLCT character that is not greatly affected by the relative minor differences in the coordination geometry induced by the crystalline environment. The arrangement of the cations in the two crystals allows interlocking interactions between the triphenylphosphine ligands on neighboring molecules that are suggested to lead to a significant restriction of the motion of the phenyl rotors in aggregates. In addition, C−H···π interactions between the bpy and the triphenylphosphine

ligands are present in the PF_6^- crystals, leading to further hindering of these internal motions. The existence of relevant intermolecular π-stacking interactions has been ruled out by analyzing the crystal packing. Since the changes in coordination geometry and electronic delocalization seem to be out of the question, the most plausible origin of the AIE effect in the studied compounds appears to be the restriction of internal motion (RIM mechanism). The presence of six phenyl rings that can experience large amplitude internal rotations around the P−C axis should lead to a relatively high density of states of vibrational modes in solution that would decrease dramatically upon aggregation and restriction of their movement. The larger phosphorescence quantum yield observed for the crystals with PF_6^- seems to hint at a larger RIM in this case, perhaps due to the additional C−H···π interactions found in the crystal. The observation of some vibrational structure in the spectra for the PF_6^- case seems also to hint to a stronger restriction of the low frequency modes, which would result in a larger spacing of their associated vibrational states and a more structured spectrum in which the vibronic progressions of the modes affected by the electron transfer are not blurred by the quasi continuum of low frequency modes active in solution or in loosely packed crystals. The importance of the intermolecular interactions analyzed in the crystal is further evidenced by the reversible color changes of [Ir(bpy)]Cl samples when grinded and fumed with different solvents, which are most likely due to the formation/destruction of non-covalent interactions.

6.6 Computational details

Ground state optimizations and frequency calculations were carried out within the framework of DFT with the B3LYP hybrid functional[111,112] in combination with a basis set of double-ζ quality (LANL2DZ) and the ECP of Hay and Wadt[120] for iridium, while the standard 6-31G(d) basis set was used for the rest of the atoms in the molecule. Vertical transition energies were calculated using TDDFT with the same xc functional and basis sets. The geometry for the lowest excited triplet state was also optimized at the same level of theory. Frequency calculations were performed within the harmonic approximation.

In order to have a reference structure for the isolated cation, the optimization calculations have been carried out in the vacuum. Since, in this study, we are only seeking for a qualitative explanation of the experimentally observed trends by comparing the calculations for different geometries of the same cation, we have not considered the necessity of accounting for the effects of solvation on the photophysical properties in our

calculations. A guess of the atomic positions of the two hydrogen atoms coordinating the iridium atom in the [Ir(bpy)]Cl and [Ir(bpy)]PF_6 crystals has been obtained through restricted geometry optimizations, in which all atoms have been frozen in the geometry obtained from X-ray diffraction and only the two hydrogen atoms directly bonded to the iridium atom were allowed to move in the energy minimization procedure. The basis set used in these calculations was 6-31G(d,p). Throughout this section, whenever the cation in the crystal's geometry is mentioned, it will correspond to this latter geometry. These restricted optimizations were also carried out in the presence of nearby counterions, but practically the same final positions for the hydrogen atoms were obtained. The ground state and the lowest triplet state of $[Ir(bpy)]^+$ were optimized starting from the monomer's geometry in the Cl^- and PF_6^- crystals. The same ground state was obtained starting from either geometry, while, for the triplet states, some differences in the relative orientations of the phenyl rings of the phosphine ligands were observed. Nevertheless, the pseudo-octahedral environment of the iridium atom and the geometry for the bpy ligand that determine the energy for the emission band were practically identical in the two geometries for the T_1 state. For this reason, we refer only to one optimized S_0 and T_1 geometry for the cation throughout the text. All electronic structure calculations reported in this study were performed with the Gaussian 09 suite of programs.[131]

6.7 Appendix

Table A2.4 Principal geometrical parameters for the coordination environment of Ir in $[Ir(bipy)]^+$, distances in Å, angles in degrees.

A^-	Ir-P1	Ir-P2	P1-Ir-P2	Ir-N1	Ir-N2	N1-Ir-N2	Ir-H1	Ir-H2	H1-Ir-H2	C-P-P-C*
Cl^-	2.310	2.297	168.0	2.136	2.119	77.4	1.591	1.599	86.2	48.0
PF_6^-	2.298	2.291	162.0	2.130	2.164	76.6	1.601	1.584	86.3	18.7

*Average value of the three smallest C-P-P-C dihedral angles.

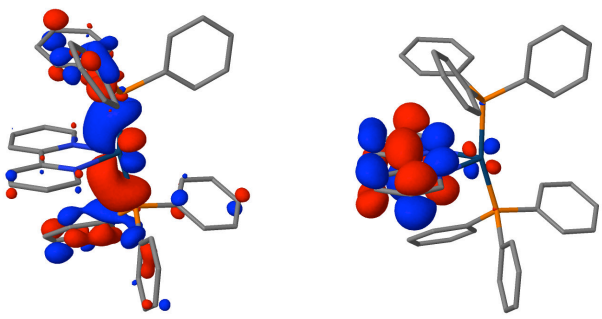

Figure A2.4 HOMO (left) and LUMO (right) of the cationic complex in the [Ir(bipy)]PF_6 crystal.

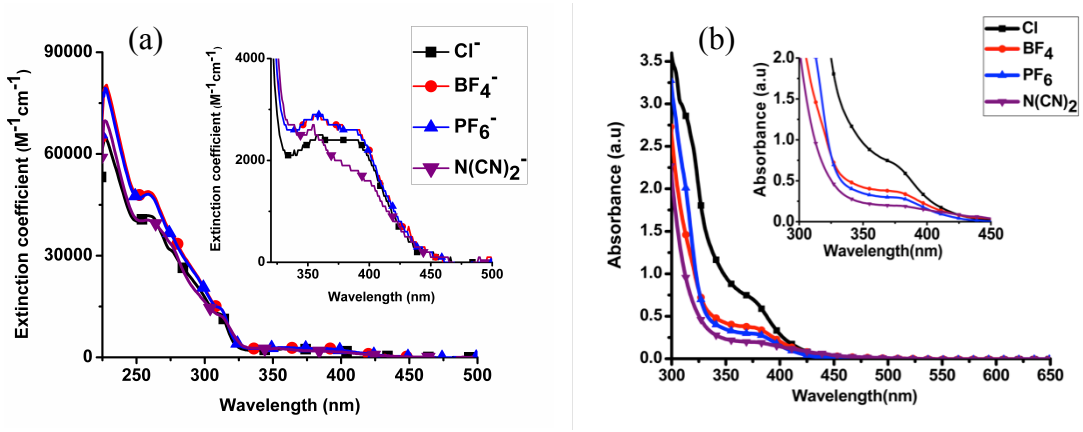

Figure A2.5 Absorption spectra for [Ir(bipy)]A [A^- = Cl^-, BF_4^-, PF_6^-, $N(CN)_2^-$] compounds (a) $1 \cdot 10^{-5}$ M solutions in DCM and (b) crystals. Taken from reference 152.

Table A2.5 Calculated *x*, *y* chromaticity coordinates for the studied complexes in DCM solution and in solid state.

(*x*,*y*)	Cl^-	BF_4^-	PF_6^-	$N(CN)_2^-$
solution	(0.26, 0.42)	(0.22, 0.40)	(0.25, 0.44)	(0.22, 0.41)
solid state	(0.27, 0.47)	(0.18, 0.29)	(0.23, 0.40)	(0.26, 0.44)

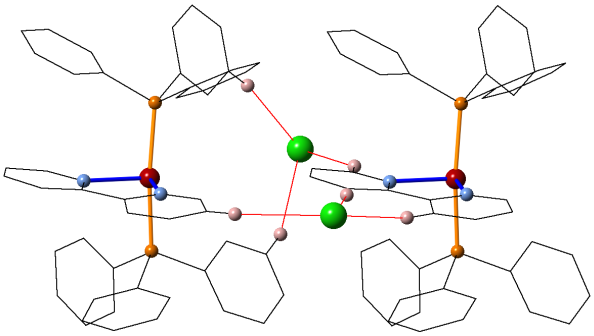

Figure A2.6 C-H···Cl interactions (red lines) between the counterion and the cation in the Cl^- crystal.

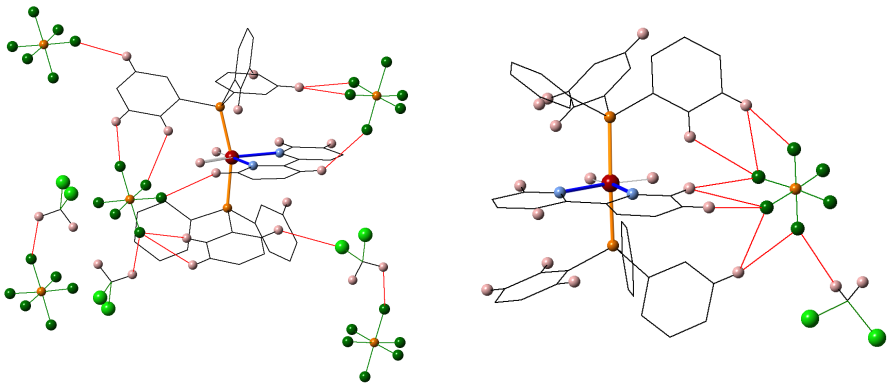

Figure A2.7 C-H···F interactions (red lines) between the counterion, the cation and the DCM solvent molecules in the PF_6^- crystal.

7. Dual emission and AIE in Ir(II) complexes with a Schiff base ligand

7.1 Introduction

Motivated by the previous works in which Ir(III) complexes with axial phosphine ligands presented AIE, our collaborators synthesized four new complexes (Figure 2.32) with general formula [IrHCl(C^N)(PPh_3)$_2$] containing different conjugated Schiff base ligands (C^N). All the complexes are phosphorescent and exhibit AIE either in aggregates formed in solution or in thin-film samples. Three very interesting practical results were obtained in this case: (i) a dual fluorescent and phosphorescent emissive complex in solution, (ii) successful acid/base sensing in solution and solid state and (iii) quantitative CO_2 detection.

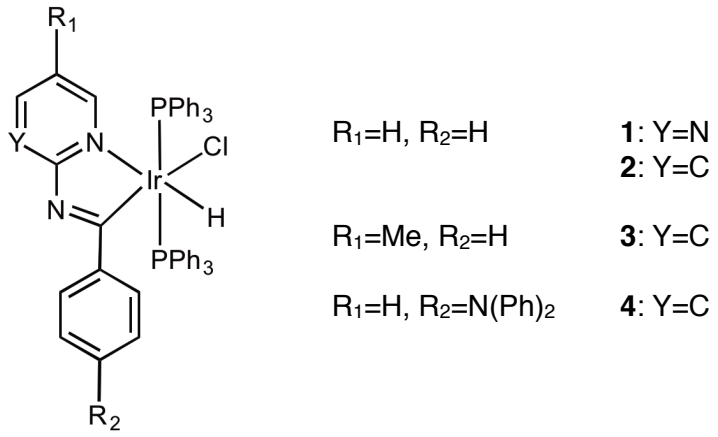

Figure 2.32 Studied complexes with general formula [IrHCl(C^N)(PPh_3)$_2$].

Complex **4** presents dual fluorescent and phosphorescent emission in solution, with the particularity that the fluorescent emission band is solvatochromic. This property is indeed very suitable for the development of Ir(III) probes,[166] in which switching of the luminescence by external stimuli is essential. In the literature, there are several examples of dual phosphorescent Ir(III) complexes,[167-174] but dual fluorescent and phosphorescent Ir(III) complexes are still scarce.[175-178] To the best of our knowledge, the Ir(III) complex synthesized in the group of Prof. Laskar is the first example of facile emission tuning between a singlet and triplet state by just varying the solvent's polarity. This certainly opens a whole new range of possibilities for the application of Ir(III) complexes as luminescent probes.

The presence of the Schiff base ligand in these complexes granted a very interesting property, namely, a dependence of the emission spectra with pH. This dependence is

observed for all four complexes in solution and in thin-film samples. In particular, the emission color of **1-4** changed upon exposure to an acid and was reversed to the original situation by exposure to a base. Therefore, these compounds have potential as acid/base sensors.

Further experiments were performed with complex **4**, and because of its AIE, quantitative detection of CO_2 was accomplished. There is nowadays active research in the field dedicated to the development of molecular sensors for quantitative detection of molecular gases, specially CO_2, due to the well-known harmful effects that high concentrations of this gas have on human beings. Current detection techniques[179,180] based on electrochemical (EC), infrared (IR), combined gas chromatography - mass spectroscopy (GC-MS) methods, or field-effect transistors are quite costly. Therefore, efficient molecular sensors based on AIE materials could represent a real breakthrough in this area.

Our goal herein was to characterize the lowest excited states of the synthesized complexes to interpret the experimental results. The nature of the emitting states of **1-4** was assigned and the simulated vibrationally resolved emission spectra agree with the experimental ones. The crystal structure of **2** was characterized by crystal X-ray diffraction. This allowed the analysis of the intramolecular interactions present in the crystal, and to give a plausible explanation regarding the origin of the observed AIE. Calculation of the protonated forms of **1-4** gave an explanation to the photoluminescent changes observed upon exposure to an acid.

7.2 Molecular and electronic structure

All the investigated complexes have a single Ir(III) metal center in a distorted octahedral coordination environment. Complexes **1-4** contain two triphenylphosphine ligands (PPh_3) axially coordinated to the Ir(III) atom. The four coordination positions on the equatorial plane are occupied by the N and C atoms of a Schiff base bidentate ligand, a chloride, and a hydride ligand. The differences between the four synthesized complexes are in the Schiff base (Scheme 1). Concretely, complex **1** contains a pyrimidine ring, while complexes **2** and **3** have pyridine and methylpyridine moieties instead, respectively. Complex **4** corresponds to the substitution of the Schiff base with a diphenylamine donor group.

The principal geometrical parameters describing the distorted octahedral environment of the Ir(III) atom in complex **2** are gathered in Table 2.14. Optimized bond distances and angles for the ground state are in qualitative agreement with the X-ray molecular structure. In both structures, the crystal monomer and the optimized singlet ground state, the angles between *trans* ligands are very similar to each other and within the 170-180º range. The largest differences arise in the Ir-C, Ir-N, and Ir-Cl bond lengths, which are overestimated by 0.05-0.09 Å in the optimized geometries. Intermolecular effects in the crystal could be responsible for the difference in the Ir-Cl bond length, but they don't seem to be responsible for the differences in the Ir-C and Ir-N bond lengths. Thus, we attribute these differences to the inherent approximations of the computational methodology. Superposition of both structures reveals that the phosphine ligands are practically identical in both geometries. Comparison of the two phosphine ligands in the complex reveals that they are enantiomers, with the iridium's equatorial plane acting as the mirror plane (Figure 2.33).

Table 2.14 Selected geometrical parameters of the iridium's coordination environment and the imine group (C-N, N=C and C-C) in the crystal (X-ray structure) and for the optimized S_0 and T_1 states of **2**.

	bond lengths (Å)								angles (º)		
	Ir-C	Ir-Cl	Ir-N	Ir-H	Ir-P	C-N	N=C	C-C	C-Ir-Cl	N-Ir-H	P-Ir-P
crystal	1.983	2.476	2.101	1.582	2.325	1.485	1.313	1.483	172	180	169
S_0	2.021	2.561	2.176	1.601	2.400	1.373	1.323	1.494	171	174	169
T_1	2.024	2.558	2.164	1.602	2.405	1.314	1.425	1.425	172	175	169

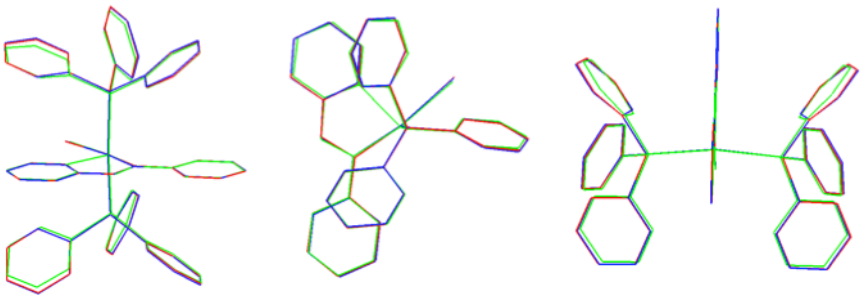

Figure 2.33 Different views of the superposition of the crystal's monomer (green) of **2** with the optimized ground state (blue) and lowest triplet state (red). Hydrogen atoms have been omitted for the sake of clarity.

Next we analyze in detail the electronic structure of the synthesized compounds by means of their frontier occupied and virtual MOs. In the following we refer to the z-axis as the one in the P-Ir-P direction while the x-axis is defined by the C-Ir-Cl direction. Figure 2.34

depicts the MO energy diagram for complex **2**. Due to the heterogeneous ligand substitution pattern, all d-type orbitals on the Ir atom exhibit sizeable mixings with ligand orbitals. In particular, Ir orbitals in the t_{2g}-like set combine with occupied p-type orbitals from the chloride ligand, the lone pairs on the phosphorus atoms and π-type orbitals from the Schiff base ligand. The two highest occupied MOs, HOMO and HOMO-1, of complex **2** are practically degenerate combinations of metal d_{xy} with chlorine p_y and metal d_{xz} with chlorine p_z AOs, respectively, with the HOMO having an additional participation of π-type orbitals of the Schiff base. The lowest unoccupied orbitals correspond mainly to π*-type orbitals of the Schiff base. The LUMO has a small contribution of the Ir atomic orbitals, while the LUMO+3 shows participation of orbitals from two phenyl rings on the phosphine ligands. Further details regarding the MOs of **2** can be found in the Appendix (Figure A2.8).

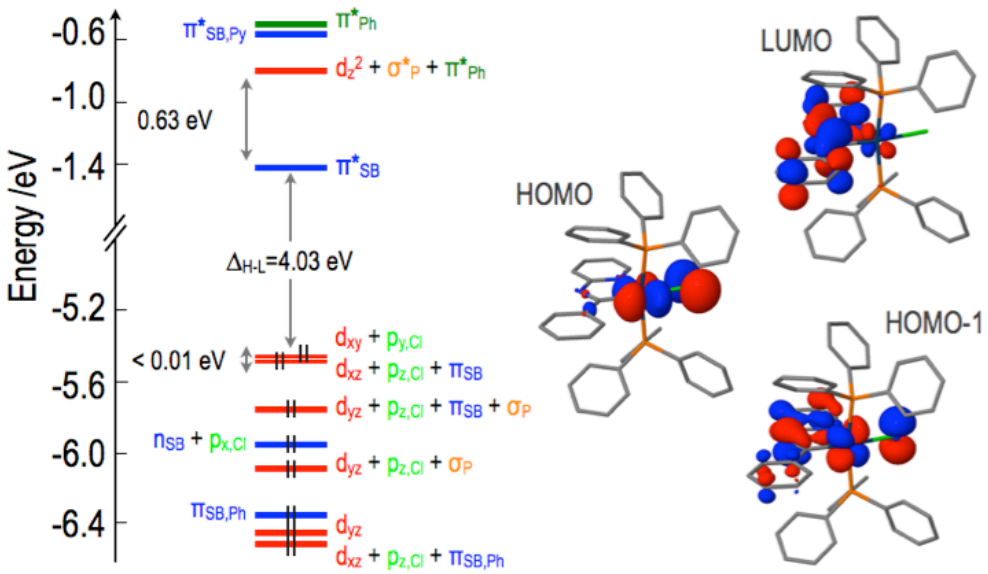

Figure 2.34 MO diagram of **2** at the optimized ground state. Participation of fragment orbitals to the whole system's MOs is indicated by the following color code: red for d-block orbitals of the iridium atom; light green for p orbitals of the chloride ligand; dark green for π and π* type orbitals of the phenyl rings of the phosphine ligands; blue for n, π and π*-type orbitals of the Schiff base ligand and orange for σ-type orbitals of the phosphorus's lone pairs. Hydrogen atoms are omitted from the picture for the sake of clarity.

MO diagrams for complexes **1** and **3** are qualitatively very similar to that of **2**, except for subtle differences in the energies of the orbitals and the degree of mixing of fragment orbitals due to the differences in the Schiff bases. There is, though, an important difference between **4** and the other three complexes. Substitution of the Schiff base with an electron-donating diphenylamine group modifies dramatically its electronic structure. The HOMO

is no longer an orbital centered on the iridium atom, but a pure π-type orbital of the donor amine unit (Figure 2.35). The remaining frontier MOs of **4** are equivalent to those of **2**.

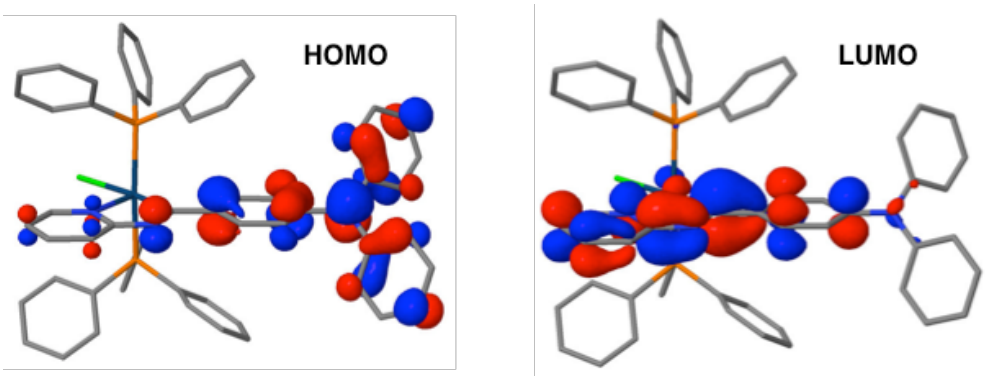

Figure 2.35 HOMO and LUMO of the optimized ground state of **4** at the B3LYP/LANL2DZ, 6-31G(d) level. The orbitals computed with the CAM-B3LYP functional are analogous. Hydrogen atoms have been omitted for the sake of clarity.

7.3 Absorption in solution

The lowest computed singlet and triplet states of complexes **1-3** correspond to excitations from the d_{xy} and d_{xz} type HOMOs to the Schiff base centered LUMO. Amplitude analysis of these excitations reveals that the corresponding excited states have important MLCT, LLCT from the chloride to the Schiff base, and LC π,π* character in the case of the excited state involving the d_{xz} based occupied orbital. For simplicity, we will from now on refer to these excited states as MLLCTy and MLLCTz/LC, where y or z indicate the atomic p orbital of the chlorine atom involved in the occupied MO of the transition. The lowest excited singlet state for complexes **1-3** is MLLCTy, while the lowest triplet corresponds to MLLCTz/LC. Contrary, the lowest computed singlet and triplet states of complex **4** correspond to HOMO to LUMO transitions with intra-ligand charge transfer (ILCT) character due to the donor nature of the diphenylamine substitution in the Schiff base. The computed vertical excitation energies to these states are gathered in Table 2.15. The excitation energies of the singlet and triplet MLLCTy and MLLCTz/LC states of all the complexes compared to **2** vary very slightly, with changes below 0.1 eV, except for the ^{3}MLLCTz/LC state of **4**, which lies ~0.3 eV above that of **2**. The oscillator strength for the transition to the ^{1}ILCT state of **4** is quite large compared to that of the ^{1}MLLCTz/LC state, that is at least ten orders of magnitude larger. The value for the ^{1}MLLCTy states is negligible due to the poor overlap of the MOs involved in the transition, yet this overlap is significant in the ^{1}MLLCTz/LC states, since the occupied orbital has π-type participation from the Schiff base, which overlaps efficiently with the π*-type LUMO.

Table 2.15 Vertical excitation energies and oscillator strengths (≥ 0.01) for the lowest excited states of **1-4.** All values computed at the B3LYP/LANL2DZ,6-31G(d) level.

	State	**1**	**2**	**3**	**4**
ΔE / eV (λ / nm)	^{3}MLLCTz/LC	2.72 (456)	2.63 (472)	2.59 (479)	2.96 (420)
	^{3}MLLCTy	3.05 (406)	3.12 (397)	3.14 (395)	3.14 (395)
	^{3}ILCT	-	-	-	2.35 (528)
	^{1}MLLCTz/LC	3.35 (370)	3.37 (368)	3.37 (368)	3.39 (365)
	^{1}MLLCTy	3.12 (397)	3.19 (389)	3.21 (387)	3.20 (387)
	^{1}ILCT	-	-	-	2.98 (416)
f	^{1}MLLCTz/LC	0.02	0.04	0.07	0.01
	^{1}ILCT	-	-	-	0.58

The UV-VIS absorption spectra in DCM solution for **1-4** are shown in Figure 2.36. The moderately intense band at 300-450 nm is assigned by our calculations to the ^{1}MLLCTz/LC state computed at ~370 nm for all complexes. The absorption profiles of complexes **1-3** are very similar to each other, as predicted by the correspondence of their MO diagrams. The absorption spectrum of complex **4** exhibits a rather intense band centered at ~400 nm not present for the other three complexes, which is a signature of the ILCT transition in the Schiff base ligand. The vertical transition to ^{1}ILCT in **4** is computed at 416 nm, in very good agreement with the experimental absorption maximum (404 nm).

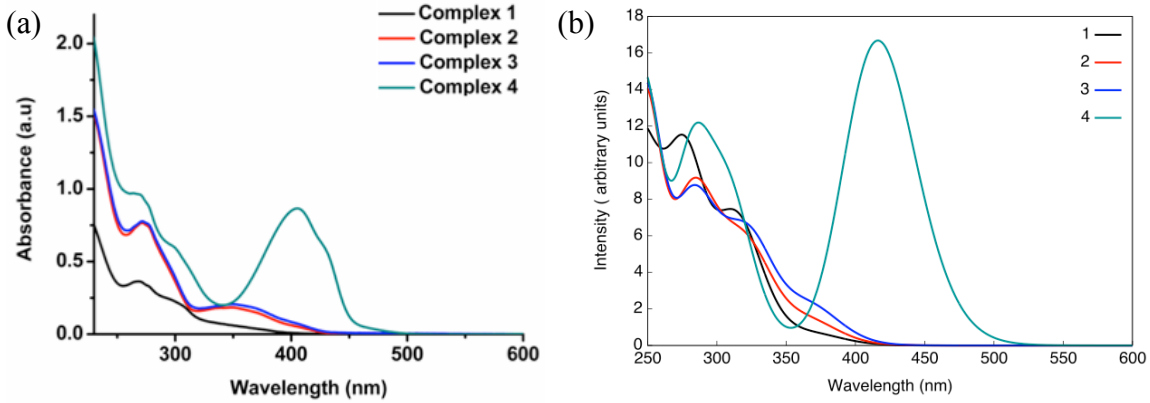

Figure 2.36 UV-Vis absorption spectra of **1-4** (a) recorded in degassed DCM (10^{-5} M) at room temperature (b) simulated at the B3LYP/LANL2DZ,6-31G(d) level.

The simulated spectra for all complexes (Figure 2.36) reproduce reasonably well the band positions and relative intensities of the experimental absorption spectra. The excited states responsible for the absorption profile do not have a dominant contribution, but many instead, making it difficult to easily assign their nature unequivocally since on top of this, the frontier MOs have quite mixed participation. NTOs were checked for these transitions, but did not help much in the description of the excited states. Hence, we preferred to

maintain the characterization based on the frontier MOs. The vertical transitions responsible for the absorption profile of complex **2** have been analyzed in detail. They mainly correspond to exited singlet states of mixed MLLCT and LC character. For higher energy excited states, d-d and LMCT character is also present (Appendix, Figure A2.9 and Table A2.6).

The solvent polarity dependence of the absorption spectra for the studied complexes was also explored experimentally. While the absorption spectra of **1-3** show no dependence on solvent polarity, the absorption spectrum of complex **4** shows a weak dependence with the solvent dielectric constant due to the strong absorption of the ^{1}ILCT state and its CT character.

7.4 Emission

The normalized emission spectra of the synthesized complexes in DCM solution and in thin film are shown in Figure 2.37. All complexes present structured emission profiles with a separation between peaks of the order of 1200 cm^{-1}, which we assign to vibronic progressions. The position and relative intensity of the vibronic peaks in the thin-film emission spectra are very close to their counterparts in solution. This matching is also reflected when comparing the emission colors in thin film with the emission colors in DCM solution, as shown in the chromaticity diagram (Figure 2.38 and Appendix, Table A2.7), for which the same green to yellow transition is observed.

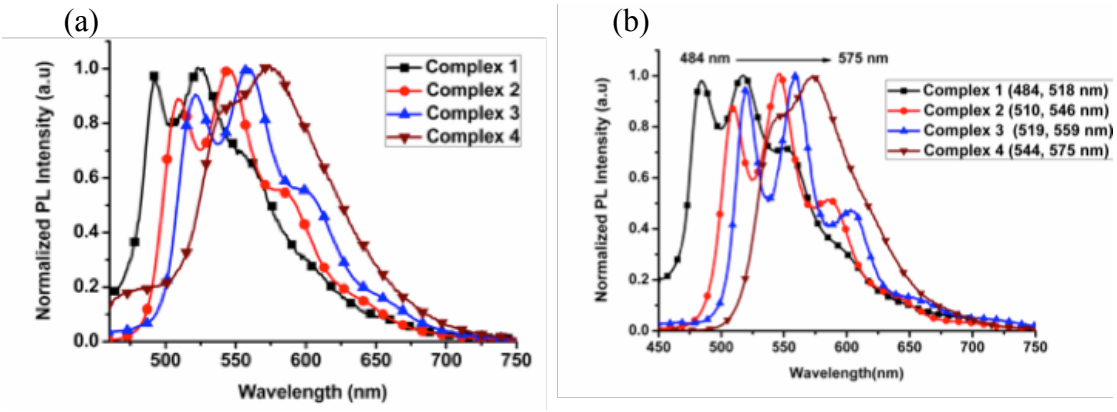

Figure 2.37 Normalized emission spectra of **1-4** (a) in degassed DCM at room temperature and (b) thin film.

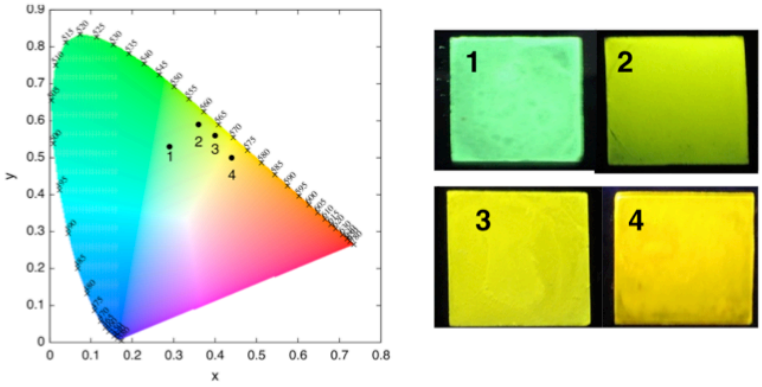

Figure 2.38 Chromaticity diagram for the emission of **1-4** in DCM (left) and their respective thin-film emission color under 365 nm UV lamp (right).

Our calculations predict the ^{3}MLLCTz/LC state as the one responsible for the phosphorescence emission of complexes **1-3**. This state was already the lowest triplet state at the FC region. For all three complexes there is a nice agreement between the experimental emission spectra and the simulated vibrationally resolved phosphorescence profiles (Figure 2.39a and Appendix, Figures A3.10 and A3.11). Each spectrum has clearly three peaks at the short wavelength region and several less intense shoulders at long wavelengths. The relative positions of the well-resolved peaks in the emission band are correctly reproduced by our calculations, but the relative intensities are, in some cases, not correctly estimated. Although the peak at ~550 nm is also the most intense in our calculations, the relative intensities with the two neighboring peaks are over and underestimated, respectively. The blue shift of the 0-0 transition with respect to the convoluted peak at ~500 nm is due to the presence of nearby transitions that contribute to the band's intensity. We could not find an explanation to why the long wavelength region of the emission band decays slower in the simulated spectra of complexes **2** and **3**.

For complexes **1-3**, the main vibrational mode responsible for the structured emission is related to the stretching of the C=N bond in the Schiff base, with a computed frequency of 1470-1450 cm^{-1} (Figure 2.39b). The distortion associated with this mode is in fact the main geometrical modification along the molecular relaxation on the T_1 state PES from the FC region. Although this vibronic progression is the main contribution defining the overall shape of the emission spectra, there are other less intense normal modes also contributing to the emission profiles (Appendix, Tables A3.8-A3.11). Apart from the C=N vibronic progression, there are combinations of modes of the imine unit with modes involving the phenyl rings of the PPh_3 ligands. Since the modifications in the Schiff base ligand of complexes **1-3** do not have a great impact on the C=N stretching mode, the peaks of the

vibronic progressions in the emission spectra are similarly spaced out in the three complexes and the relative intensities are alike. The main effect of the substitution is therefore in tuning the energy of the electronic transition from the T_1 state back to the ground state, but not in the modification of the overall shape of the emission spectrum. As we move from complex **1** across to **2** and **3**, the emission spectrum is slightly red-shifted. The same trend was already observed for the vertical transition energies from the ground state to the ^{3}MLLCTz/LC state.

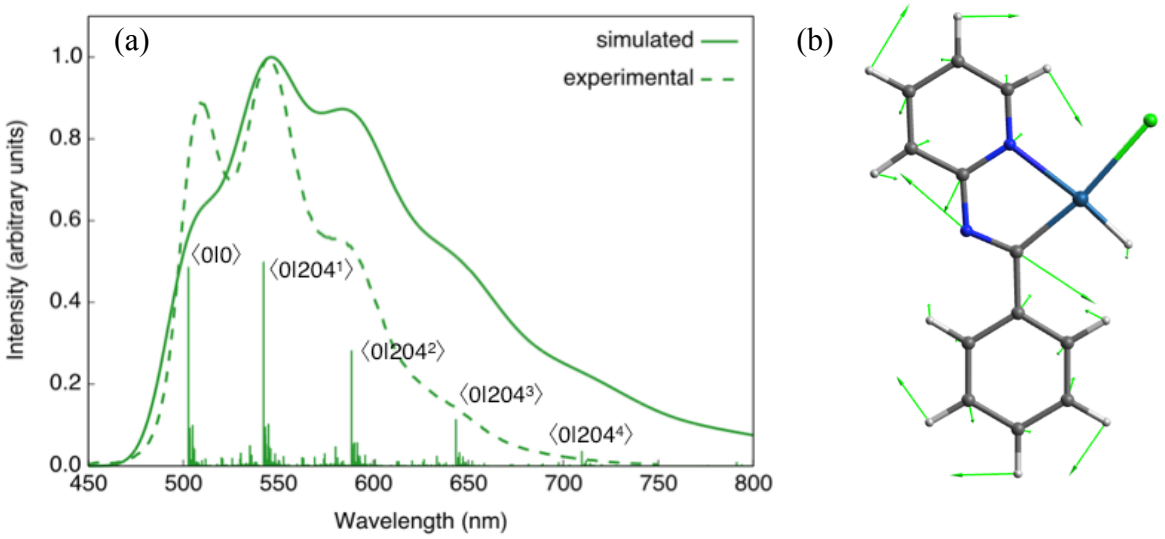

Figure 2.39 (a) Simulated (solid line) and experimental (dashed line) phosphorescent emission spectra of **2**. Vertical sticks indicate the relative strength of vibronic transitions contributing to the simulated spectrum. Both spectra have been normalized and the calculated spectrum has been blue shifted by 0.12 eV to superimpose the most intense peaks (b) Displacement vectors of the normal mode (204) responsible for the vibrational structure. The triphenylphosphine ligands have been omitted for greater clarity.

The emission spectrum of **4** in solution exhibits two clearly distinct bands (Figure 2.40a): (i) a solvatochromic band at 400-525 nm and (ii) a structured emission band in the 525-700 nm region, very similar to the emission band in **1**-**3**, that is practically independent of the solvent's polarity for all complexes. Due to this dual emissive behavior, the emission color of **4** may be easily tuned by varying the solvent's polarity. In particular, in low polarity solvents (benzene, 1,4-dioxane), the emission color of **4** is blue with an emission band maximum at 461 nm, whereas in more polar solvents (ethyl acetate, $CHCl_3$, DCM and THF) the emission gradually shifts to longer wavelengths. In strongly polar solvents (DMSO) complex **4** shows a yellow emission (Figure 2.40b).

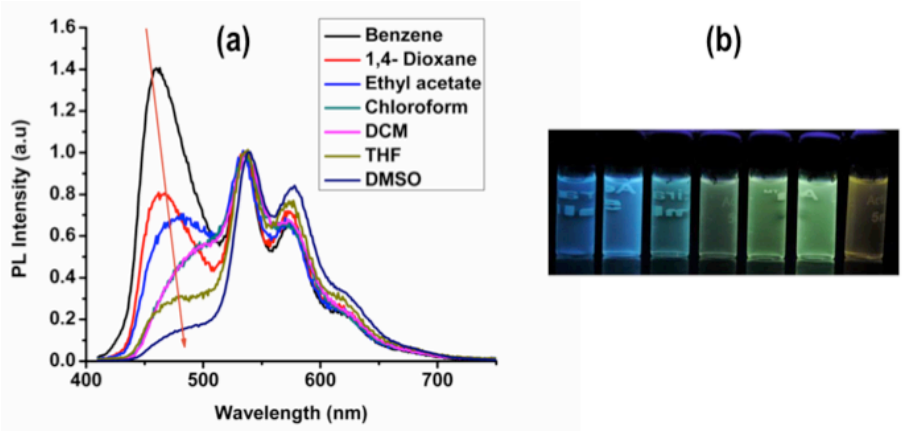

Figure 2.40 (a) Emission spectra of **4** in different solvents (b) Photographs showing the emission colors of **4** under UV light in different solvents (from left to right): benzene, 1,4-dioxane, ethyl acetate, $CHCl_3$, DCM, THF and DMSO. Concentration of **4** in all cases: 10^{-5} M. The spectra have been normalized to the peak at ~535 nm.

The similarities of the emission of **4** in the 525-700 nm region with the emission spectra of complexes **1-3** allows us to assign this band to the phosphorescence emission from the ^{3}MLLCTz/LC state. When trying to optimize complex **4** on the triplet PES, either with DFT or TDDFT and in vacuum or in different solvents, it always converged to an ^{3}ILCT state, regardless of the functional (B3LYP or CAM-B3LYP). On the other hand, our calculations indicate that the state responsible for the solvatochromic band below 500 nm corresponds to the singlet state with ILCT character. This assignment seems to be also supported by life-time measurements of the band at 450 nm in different solvents (benzene, DCM, THF and DMSO), obtained within the 0.9-1.4 ns range, consistent with a fluorescent emission. However, the measured life-time of the band at 530 nm is observed in the microsecond range (1.4-1.7 μs), which is consistent with phosphorescent emission. The ^{1}ILCT state of **4** was optimized in strongly polar and non-polar solvents, i.e. DMSO and benzene, for which the experimental emission maxima were measured at 480 and 459 nm**,** respectively. The calculated relative shift in the vertical emission energies of **4** in benzene and DMSO is 0.16 eV, in very good agreement with the shift observed in the experimental spectra (0.12 eV). As the polarity of the solvent increases, the LUMO is more stabilized than the HOMO, leading to the observed red-shift in the emission energy. The trend of the intensity of the experimental ILCT emission band with the polarity of the solvent is not the one predicted by the computed oscillator strengths (Table 2.16), thus, this may be ascribed to the relative populations of the ^{1}ILCT and ^{3}MLCTz/LC states with varying solvent polarity.

Table 2.16 Vertical emission energies and oscillator strengths (*f*) of the excited singlet states of n,π* and ILCT character of **4** computed with the CAM-B3LYP and B3LYP functionals in different solvents (DMSO and benzene).

	CAM-B3LYP				B3LYP			
	DMSO		benzene		DMSO		benzene	
	ILCT	n,π*	ILCT	n,π*	ILCT	n,π*	ILCT	n,π*
ΔE / eV	2.90	2.37	3.06	2.31	2.46	1.97	2.48	1.91
nm	428	524	405	536	505	629	500	648
f	1.36	0.00	1.00	0.00	0.78	0.00	0.31	0.00

When optimizing the lowest excited singlet state of **4**, the ^{1}ILCT state and an n,π* state were obtained. This n,π* state mainly consisted in electron transfer from the lone pair of the iminic nitrogen to the π*-type LUMO of the Schiff base. The relative energies between the minimum of these two excited singlets computed with different functionals and solvents are shown in Table 2.17. With the B3LYP functional, due to its well-known tendency to stabilize charge-transfer states, the ILCT state is always the lowest excited singlet. The CAM-B3LYP results, which in principle should be more reliable for the ILCT state, suggest that in polar solvents the ILCT state is the most stable one, while in non-polar solvents it is the n,π* state. Comparison between the CAM-B3LYP computed vertical emission energies (Table 2.16) with the available experimental data evidences that the ILCT state is responsible for the emission band below 500 nm. The oscillator strength of the n,π* state is null due to the inexistent overlap between the involved orbitals, thus it cannot be responsible for the observed emission. By following Kasha's rule, one may be tempted to think that the singlet emissive state changes from n,π* to ILCT with increasing solvent polarity, when moving from benzene to DMSO. One must be cautious since although CAM-B3LYP improves the description of charge-transfer states compared to B3LYP, it may not properly describe states of different nature on the same footing.

Table 2.17 Relative energies (in kcal/mol) between the n,π* and ILCT singlet excited states of **4** optimized with the CAM-B3LYP and B3LYP functionals in different solvents (DMSO and benzene).

CAM-B3LYP				B3LYP			
DMSO		benzene		DMSO		benzene	
ILCT	n,π*	ILCT	n,π*	ILCT	n,π*	ILCT	n,π*
0.0	2.0	2.2	0.0	0.0	3.8	0.0	0.2

The tendency of B3LYP to exaggerate charge-transfer is clearly seen in Table 2.16, comparing the lower values of the oscillator strength of the ILCT state to those obtained

with CAM-B3LYP. This is because the dihedral angle between the amine and the Schiff base plane is 67º in benzene and 53º in DMSO when computed with B3LYP, while with CAM-B3LYP it is 38º in benzene and 36º in DMSO.

Further calculations designed to explore the potential formation of a twisted intramolecular charge transfer state[181] (TICT) were carried out. The energy profile in benzene and DMSO along the molecular torsion of the diphenylamine donor group in the Schiff base ligand was calculated. Our results (Figure 2.41) indicate that the potential energy minimum of ^{1}ILCT corresponds to the same dihedral angle between the phenyl rings of the donor group and the planar Schiff base ligand obtained for the optimized ground state. Moreover, this picture is virtually the same for the two explored solvents. These results force us to rule out the formation of a TICT state in this compound.

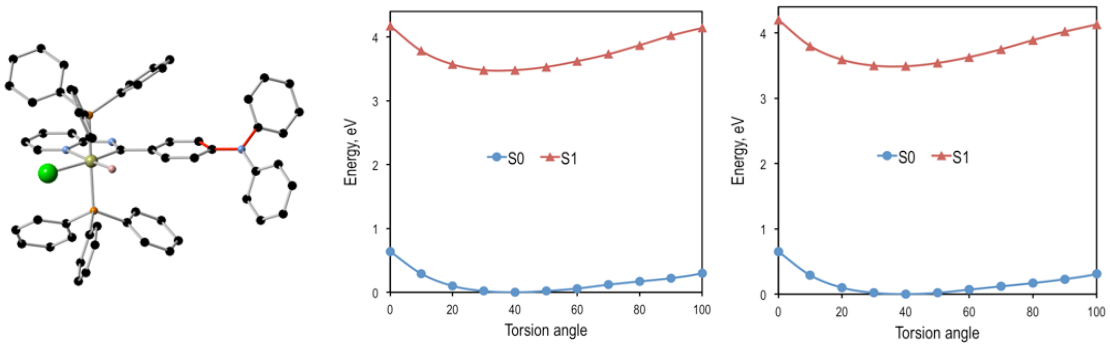

Figure 2.41 Molecular torsion in the Schiff base ligand of **4** (left) and corresponding energy profiles of the ground (S_0) and ^{1}ILCT (S_1) states of **4** in benzene (middle) and DMSO (right) computed with the CAM-B3LYP functional.

Frozen samples of **4** in benzene and 1,4-dioxane at -80ºC showed yellow emission under excitation at 365 nm, while at room temperature a blue emission was observed**.** Since the yellow emission of **4** has been attributed to the ^{3}MLLCTz/LC state, this suggests that molecular relaxation of the ^{1}ILCT state from the FC geometry is slowed down in the frozen samples, allowing the population of the ^{3}MLLCTz/LC state via intersystem crossing.

7.5 Aggregation induced emission

In order to explore the possibility of whether weak intermolecular interactions could be responsible for the restriction of intermolecular motions in the solid state and give rise to an enhancement of the PL intensity upon aggregation, the crystal packing of **2** was analyzed in detail considering that it might represent an acceptable structural model for the

aggregates formed in the mixtures of water with organic solvents. The crystal structure of **2** has a unit cell with four equivalent Ir(III) complexes together with four cocrystallized ACN molecules exhibiting disorder in the position of their hydrogen atoms. Iridium complexes arrange in chains along the *b*-axis, with each chain being surrounded by six other chains in an approximate elongated hexagonal fashion as shown in Figure 2.42. The molecules of the reference chain (highlighted in red) lie in the same *ac*-plane as the chains highlighted in grey. On the other hand, the chains shown in blue are displaced by half a unit cell along the *b*-axis with respect to the reference chain. Inspection of interatomic distances between molecules in the reference and grey chains indicates the absence of potentially important non-covalent interactions between them. The reference and blue chains, however, exhibit short interchain C-H···Cl distances (2.802 Å) between the chloride ligand and a hydrogen atom from an adjacent PPh_3 ligand, indicative of non-negligible interchain interactions that represent a possible source of restriction of molecular motions in the solid state (Appendix, Figure A2.12). Nevertheless, the most significant interactions are found along the chains themselves, where crystallized ACN solvent molecules alternate with iridium complexes, as shown in Figure 2.43. An analysis of intermolecular distances hints to the presence of strong C-H···π interactions between each ACN molecule and two phenyl rings from PPh_3 ligands of adjacent complexes. The computed interaction energy between one complex with the two neighboring ACN molecules was 9.1 kcal/mol, confirming the presence of these C-H···π interactions.

Further calculations were carried out to investigate the origin of the observed disorder for the hydrogen atoms of the ACN molecules in the crystal structure. Calculation of the energy cost for a rotation of the methyl group of the solvent molecule considering a fixed geometry was done in the presence of the two neighboring complexes (see Computational details). Two minima were obtained corresponding to the two hydrogen configurations found in the resolution of the crystal structure. The computed energy barrier (0.3 kcal/mol) for the interconversion of the two conformations lies below the thermal energy at the temperature of crystal determination (0.4 kcal/mol), suggesting that the origin of the observed disorder in the crystal structure is dynamic rather than static. These calculations show that in the crystal we should expect the methyl groups to rotate quite freely, establishing thus C-H···π interactions that restrict the motion of the PPh_3 ligands and block non-radiative decay channels in the solid state with an increase of the emission intensity as a result.

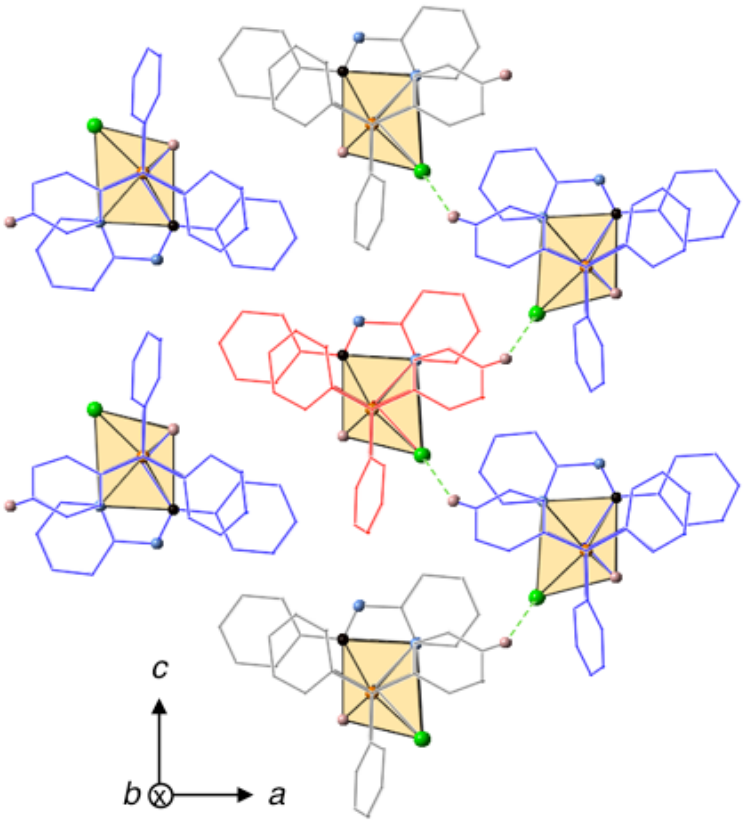

Figure 2.42 Crystal packing of **2** with a reference chain highlighted in red. C-H···Cl interactions (2.802 Å) between chains are shown in green. Atom color code: nitrogen in blue, phosphorus in orange, chlorine in green, carbon in black, and hydrogen in white. Hydrogen atoms not involved in intermolecular interactions are omitted for the sake of clarity.

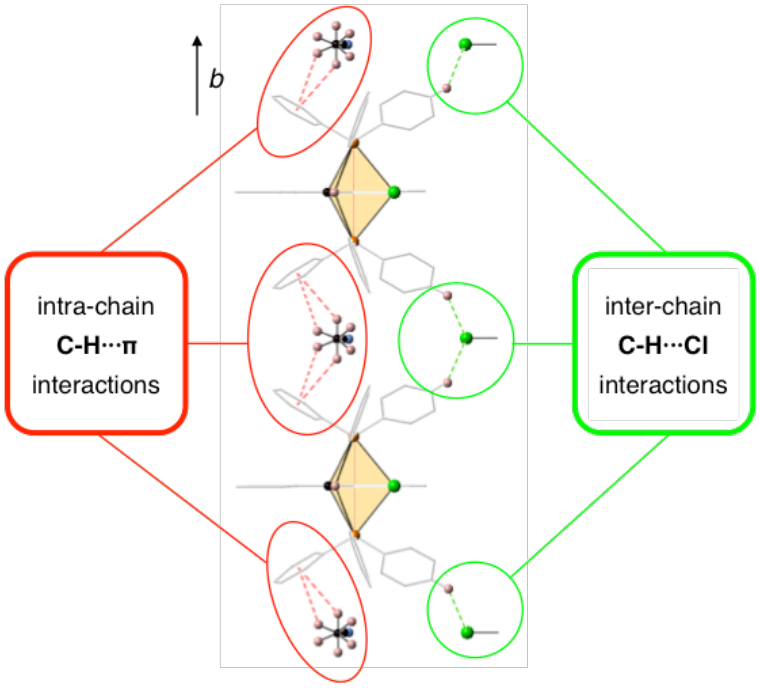

Figure 2.43 C-H···π interactions between ACN molecules and Ir(III) complexes along the crystal chains and inter-chain C-H···Cl interactions with the chains highlighted in blue in Figure 2.42. ACN molecules present dynamic disorder.

7.6 Reversible protonation-deprotonation

Further experiments of complexes **1-4** were performed in the presence of trifluoroacetic acid (TFA) and triethylamine (Et_3N) to evaluate their capability as acid/base sensors. The emission of **1-4** either in DCM solution or in thin-film samples is indeed affected by the exposure to TFA and reversed to its original emission by exposure to Et_3N. Therefore, the dependence of the emission profiles for these complexes with pH suggests these materials as potential candidates for H^+ detection.

As an example, the thin-film emission spectra of **1** is shown in Figure 2.44. The exposure of **1** to TFA results in a broad emission band with a maximum at 539 nm responsible for a yellow emission, which is reversible to the original green emission after exposure to Et_3N. A similar red-shift was observed for the thin-film emission of **4** after protonation with TFA, while the emission color change of **2** and **3** was less pronounced. In DCM solution (Figure 2.45), the emission of **1-3** was blue-shifted to 475 nm after exposure to TFA, while that of **4** was red-shifted. Regardless of the color change, a common feature of all the complexes either in thin film or in DCM solution after protonation due to TFA exposure was the loss of vibrational structure of the emission band.

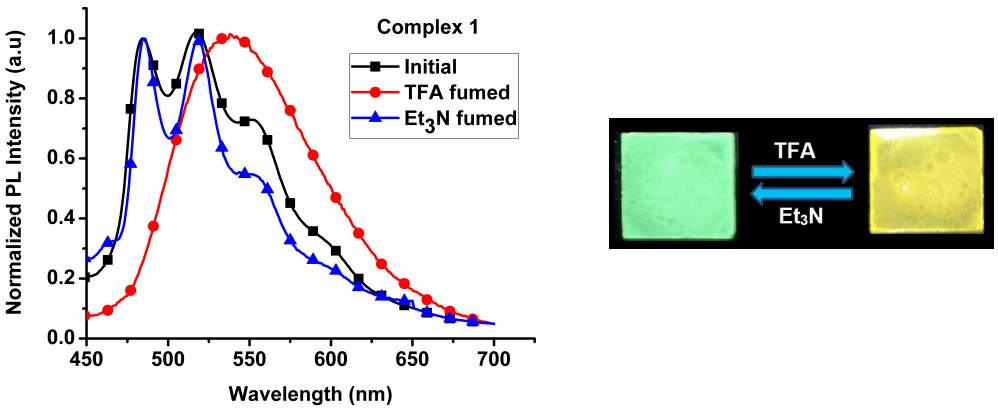

Figure 2.44 Solid-state reversal of emission color of **1** from green to yellow on exposure to TFA and the reverse process on exposure to Et_3N. The corresponding emission spectra is shown. The photographs were taken under excitation with 365 nm radiation.

The reversibility of such protonation/deprotonation process was confirmed experimentally by ^1H NMR spectra. Electronic structure calculations suggest that the energetically most favorable protonation occurs on the iminic nitrogen for all complexes (Appendix, Figure A2.13 and Table A2.12). Computation of the protonated cationic form of complex **2** (labeled as **2H**) indicates that the most important geometrical difference with respect to the neutral complex is the larger torsion angle of the phenyl ring of the Schiff base ligand due

to steric hindrance between one of its hydrogen atoms and the protonating hydrogen atom (Figure 2.46). In the unprotonated complex, the Schiff base ligand is completely planar, while in the **2H** form the phenyl ring experiences a torsion of 22º with respect to the complex's equatorial plane. Other structural differences of the coordination sphere of complex **2** upon protonation may be found in the Appendix (Table A2.13).

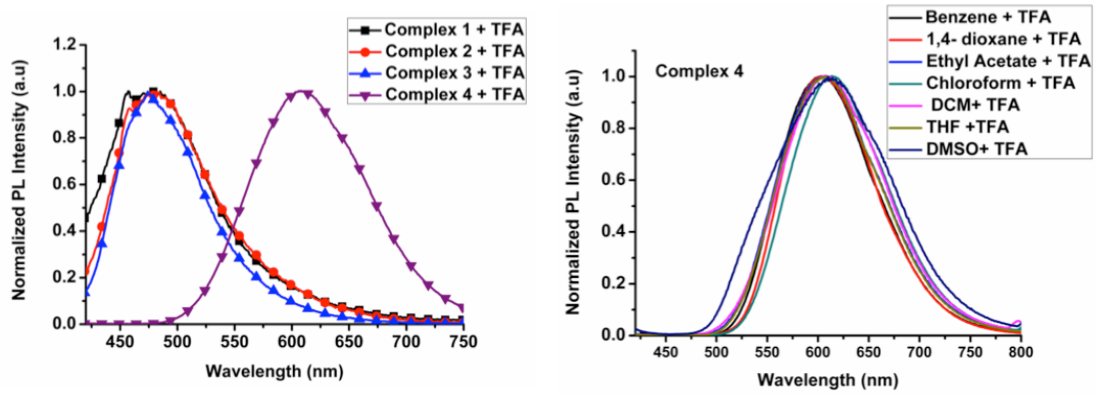

Figure 2.45 Emission spectra of **1-4** in solution (DCM) in the presence of TFA (left) and of **4** in different solvents + TFA.

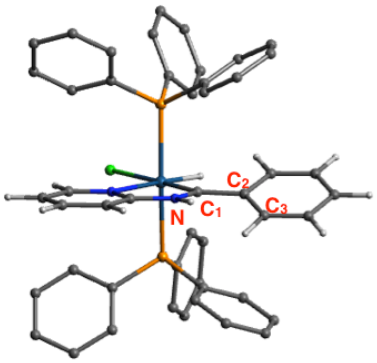

Figure 2.46 Optimized S_0 geometry of **2H**. Hydrogen atoms of the PPh_3 ligands are omitted for the sake of clarity.

Protonation of the molecular species disrupts their electronic properties, resulting in changes of their photophysical behavior. Concretely, there is a reduction of the HOMO-LUMO gap upon protonation. Moreover, in the protonated form the electron density on the Schiff base ligand is strongly stabilized, as shown in the molecular orbital diagram for **2H** in Figure 2.47. As a result, the highest occupied orbitals with d_{xy} and d_{xz} participation do not show contributions from the conjugated systems of the bidentate ligand, and the computed excitation energies to the ^{3}MLLCTy and ^{3}MLLCTz states are very close to each other at the FC region, as shown for complexes **1H** and **2H** in Table 2.18. The optimized

lowest triplet state of **1H** and **2H** is of MLLCTy character, with no participation of the Schiff base ligand, in contrast to the MLLCTz/LC character of the unprotonated forms. The experimental blue-shift of the emission energies between the unprotonated and protonated forms of **1** and **2** in solution is not captured by our calculations, since they predict a red-shift in the emission upon protonation. Nevertheless, the vertical emission energies computed for **1H** and **2H** are practically identical, in agreement with the experimental emission bands of **1** and **2** in DCM in the presence of TFA (Figure 2.45). These values however strongly underestimate the experimental emission maxima at ~475 nm.

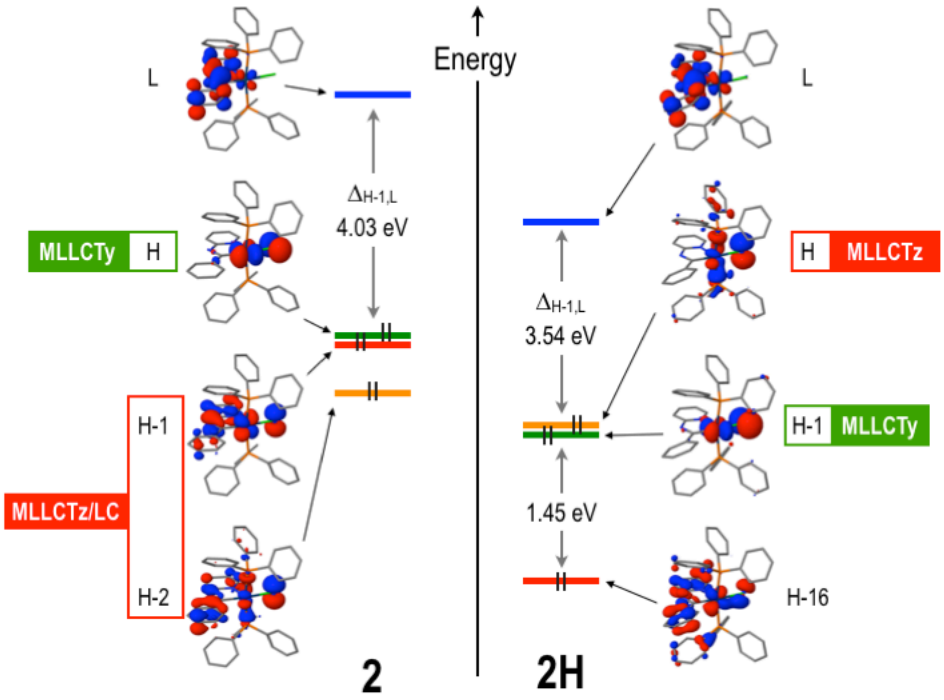

Figure 2.47 Representation of the MO diagram of **2** in its neutral (left) and protonated (right) forms. MLLCTz and MLLCTy labels indicate occupied MOs contributing to the corresponding lowest lying triplet states. Note: distribution of the MOs along the vertical axis only corresponds to a qualitative schematic representation of their relative energies.

Table 2.18 Vertical energies to the lowest excited triplet states (T_1 and T_2) of **1** and **2** in their protonated and unprotonated forms. The values are computed at the S_0 and T_1 optimized geometries.

Form	State	Character	S_0 geometry		T_1 geometry	
			1	**2**	**1**	**2**
unprotonated	T_1	MLLCTz/LC	2.72	2.63	2.05	1.84
	T_2	MLLCTy	3.05	3.12	2.67	2.74
protonated	T_1	MLLCTy	2.55	2.61	1.35	1.34
	T_2	MLLCTz	2.62	2.69	1.96	2.01

The lowest triplet state of **4H** was optimized using DFT and TDDFT with the B3LYP and CAM-B3LYP functionals, but the obtained state was always of ILCT character, as it also happened for the unprotonated form. These results are not consistent with the available experimental data. In particular, the emission maximum of **4** is independent of the solvent polarity upon TFA exposure, thus ruling out the possibility of emission from an ^{3}ILCT state.

All these results point towards three factors responsible of the broad emission band with no vibrational structure observed upon exposure of the complexes to TFA: (i) the absence of LC character in the emitting triplet state, (ii) the loss of ligand planarity and (iii) the increase of molecular flexibility.

7.7 Conclusions

Our results indicate that the triplet state responsible for the vibrationally structured phosphorescence band of the synthesized complexes is of mixed MLLCT and LC character of the Schiff base. The presence of a donor-acceptor unit in **4** is responsible for the additional fluorescence emission observed and it's positive solvatochromism (increase in emission wavelength with increase in solvent polarity). The excited state responsible for this fluorescence has been characterized by our calculations as an ^{1}ILCT state on the Schiff base ligand. Such dual emission present in **4** accounts for color tuning from blue to yellow by increasing the solvent's polarity. The crystal packing of **2** was analyzed revealing significant inter-chain C-H$\cdots\pi$ interactions (~9 kcal/mol) and intra-chain C-H$\cdots$Cl interactions, which could be responsible for the hindering of internal motions of the PPh_3 ligands, blocking the non-radiative decay channels and hence enhancing the emission in the solid state. Our calculations indicate that the iminic nitrogen is protonated when the complexes are exposed to TFA. The change in the emission profile to a broad band is due to the change in nature of the emitting state upon protonation. This state was characterized as ^{3}MLCT, with no LC admixture of π-π^* transitions in the Schiff base ligand, because of the stabilization of the π electronic density of the ligand upon protonation.

7.8 Computational details

Electronic structure calculations were performed within the DFT framework. Geometry optimizations for the ground state (S_0) and lowest triplet state (T_1) were carried out with the B3LYP hybrid functional,[111,112] the double-ζ quality basis set consisting of Hay and

Wadt's ECP[120] (LANL2DZ) for the iridium atom and the standard all-electron 6-31G(d) basis set for all other elements. Optimized geometries were identified as true local minima with no imaginary frequencies within the harmonic approximation. Vertical transition energies at the S_0 and T_1 geometries were computed via TDDFT with the same energy functional and basis set. The absorption spectra were simulated by convolution of Gaussian functions with a half-width at half maximum (HWHM) of 3500 cm^{-1}. The vibrationally resolved emission spectra for T_1 were simulated within the FC approximation as described by Barone et al.[132] and a HWHM of 650 cm^{-1} was used for the Gaussian convolution. All calculations were done considering isolated molecules in the vacuum, except for the optimization of the S_0, ILCT and n,π* singlet states of complex **4**, for which the IEF-PCM method[136-138] was employed in order to account for solvent effects. Vertical excitation energies of these states were also computed in solution when studying the solvatochromic emission of complex **4**. In addition, the CAM-B3LYP functional[115] was used for the optimization of the ^{1}ILCT state of **4** to account for the strong charge-transfer nature of this transition, not properly described by the B3LYP functional.[182] Interactions between ACN molecules and Ir(III) complexes in the crystal structure were analyzed using two molecular models: (i) two Ir(III) complexes and the central ACN molecule and (ii) one Ir(III) complex with two ACN molecules interacting via both PPh_3 ligands. Interaction energies between ACN molecules and Ir(III) complexes were computed applying the standard counterpoise correction for the basis set superposition error[183] at the M06-2X/LANL2DZ, 6-31G(d,p) level.[114] The origin of the observed disorder for solvent molecules in the crystal structure was also investigated at the M06-2X/LANL2DZ,6-31G(d,p) level by carrying out a fixed rotation of the methyl group of one ACN molecule in the presence of the two neighboring interacting Ir(III) complexes with fixed geometries. Color coordinates for compounds **1-4** were calculated from the experimental emission spectra in the standard CIE (2º) 1931 color space[130] following a conventional procedure. All electronic structure calculations were performed using the Gaussian09 package.[131]

7.9 Appendix

From the HOMO to HOMO-7 (Figure A2.8), there are only two orbitals that do not have participation of the iridium atom. That is, HOMO-3, which is a combination of the non-bonding orbital of the nitrogen atom of the imine unit with the p_x orbital of the chloride ligand, and HOMO-5 which is a π-orbital of the phenyl ring of the Schiff base ligand. The

LUMO+1 is mainly a d_z^2 type orbital with some participation of π-type orbitals of the phenyl rings of the phosphines and lies ~0.6 eV above the LUMO due to the anti-bonding interaction with the lone pair of the phosphorus. The $d_{x^2-y^2}$ type orbital on the other hand, appears rather high in energy due to strong anti-bonding interactions with orbitals of the hydride ligand, the phosphorus atoms, and the nitrogen of the Schiff base.

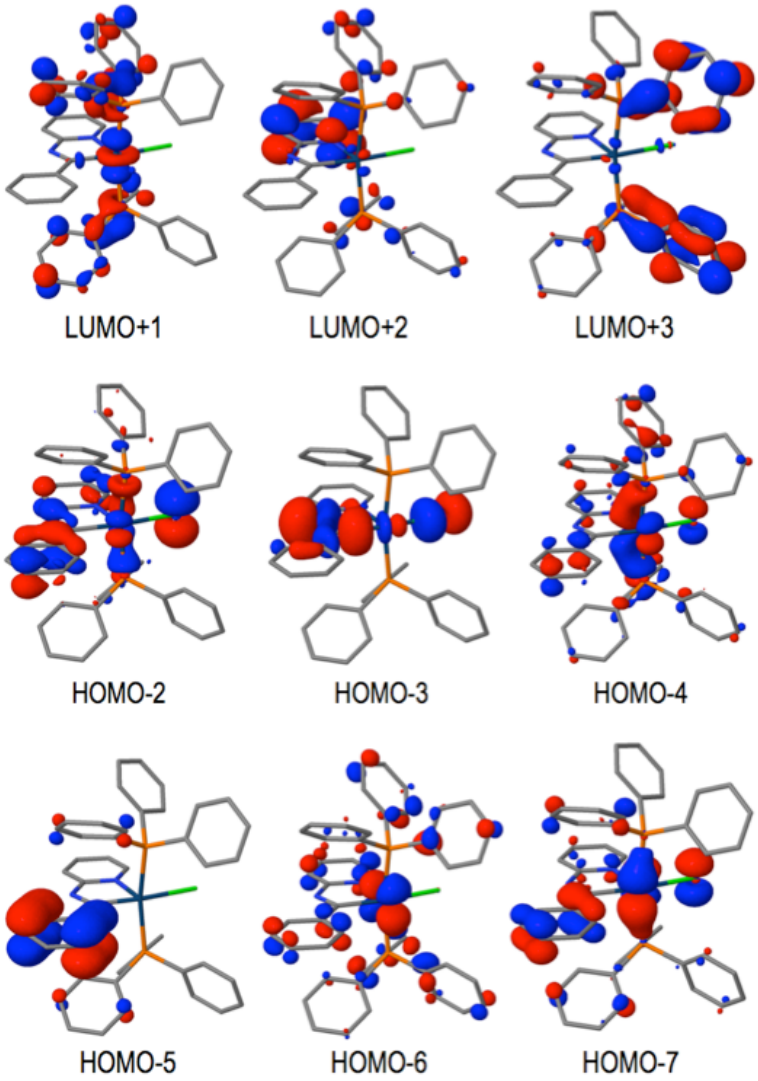

Figure A2.8 Representation of selected MOs of **2**.

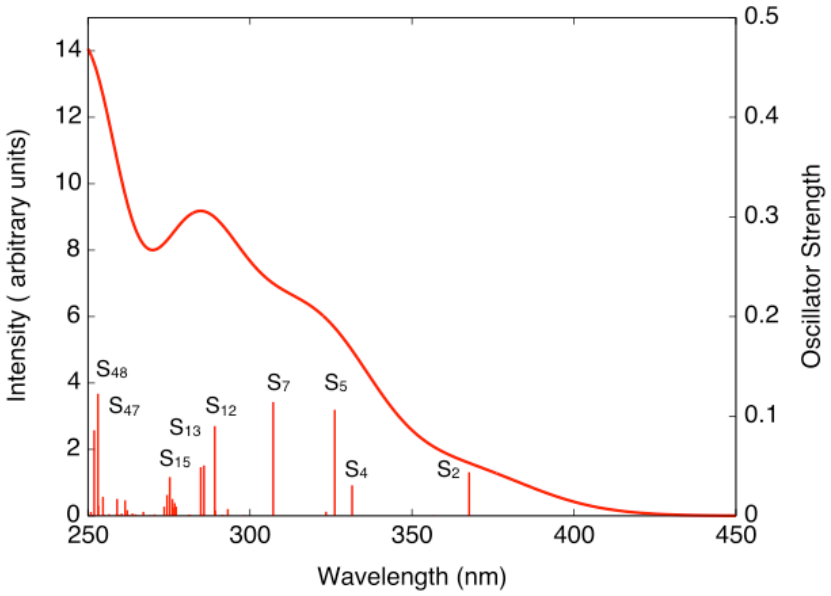

Figure A2.9 Simulated absorption spectrum of **2** along with a stick spectrum.

Table A2.6 Data relative to the most intense electronic transitions of the simulated absorption spectrum of **2** corresponding to Figure A2.9.

State	ΔE / eV	λ / nm	*f*	Contributions	Assignment[1]
S_2	3.37	368	0.04	H-1→L (89%)	$ML_{Cl}L_{SB}CT/L_{SB}C$
S_4	3.74	332	0.03	H-2→L (20%) H→L+1 (61%)	$ML_{Cl}L_{SB}CT/L_{SB}C$ $d\text{-}d/ML_{Cl}L_{Ph}CT/L_{Cl}MCT$
S_5	3.80	326	0.11	H-2→L (58%) H→L+1 (27%)	$ML_{Cl}L_{SB}CT/L_{SB}C$ $d\text{-}d/ML_{Cl}L_{Ph}CT/L_{Cl}MCT$
S_7	4.04	307	0.11	H-4→L (77%)	$ML_{Cl}L_{SB}CT$
S_{12}	4.29	289	0.09	H-2→L+1 (63%) H-1→L+3 (22%)	$d\text{-}d/ML_{Cl}L_{SB}L_{Ph}CT/L_{Cl}L_{SB}MCT$ $ML_{Cl}L_{SB}L_{Ph}CT$
S_{13}	4.34	286	0.05	H-2→L+1 (23%) H-1→L+3 (56%)	$d\text{-}d/ML_{Cl}L_{SB}L_{Ph}CT/L_{Cl}L_{SB}MCT$ $ML_{Cl}L_{SB}L_{Ph}CT$
S_{15}	4.35	285	0.05	H-7→L (33%) H-6→L (28%) H-1→L+2 (16%)	$ML_{Cl}L_{SB}CT/L_{SB}C$ $ML_{SB}CT$ $ML_{Cl}L_{SB}CT/L_{SB}C$
S_{47}	4.90	253	0.12	H-7→L+1 (24%) H-6→L+1 (16%) H-4→L+1 (18%)	$d\text{-}d/ML_{Cl}L_{SB}L_{Ph}CT/L_{Cl}L_{SB}MCT$ d-d $d\text{-}d/ML_{Cl}L_{Ph}CT/L_{Cl}MCT$
S_{48}	4.92	252	0.09	H-4→L+2 (70%)	$ML_{Cl}L_{SB}CT$

[1]Key:

$LC = \pi_L \rightarrow \pi_L^*$; $L_iLCT = L_i \rightarrow L$; $d\text{-}d = d_{ij} \rightarrow d_z^2$ (i,j=x,y,z)

$MLCT = d_{ij} \rightarrow \pi_L$; $LMCT = \pi_L \rightarrow d_{ij}$ (i,j=x,y,z)

$ML_1LCT = MLCT + L_1LCT$; $ML_1L_2LCT = MLCT + L_1LCT + L_2LCT$

$L_1L_2MCT = L_1MCT + L_2MCT$

Table A2.7 Calculated x,y color coordinates for complexes **1-4**.

(x,y)	1	2	3	4
solution	(0.29, 0.53)	(0.36, 0.59)	(0.40, 0.56)	(0.44, 0.50)
thin film	-	(0.36, 0.59)	-	-

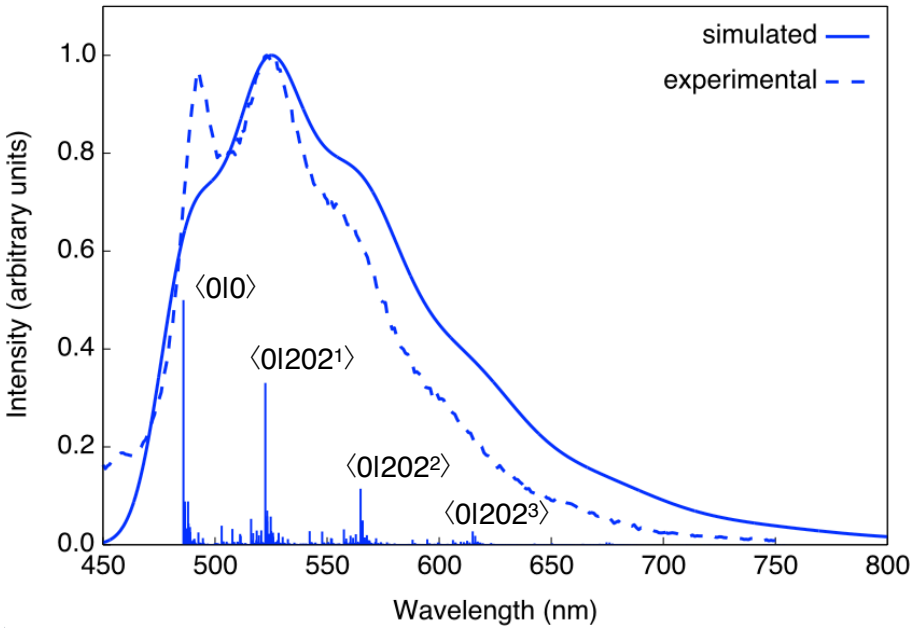

Figure A2.10 Simulated (solid) and experimental (dashed) emission spectra of 1 together with the calculated stick spectrum. Both spectra have been normalized and the calculated spectrum has been blue shifted by 0.09 eV to superimpose the most intense peaks. The 202 normal mode of vibration corresponds to the C=N stretching mode of the imine.

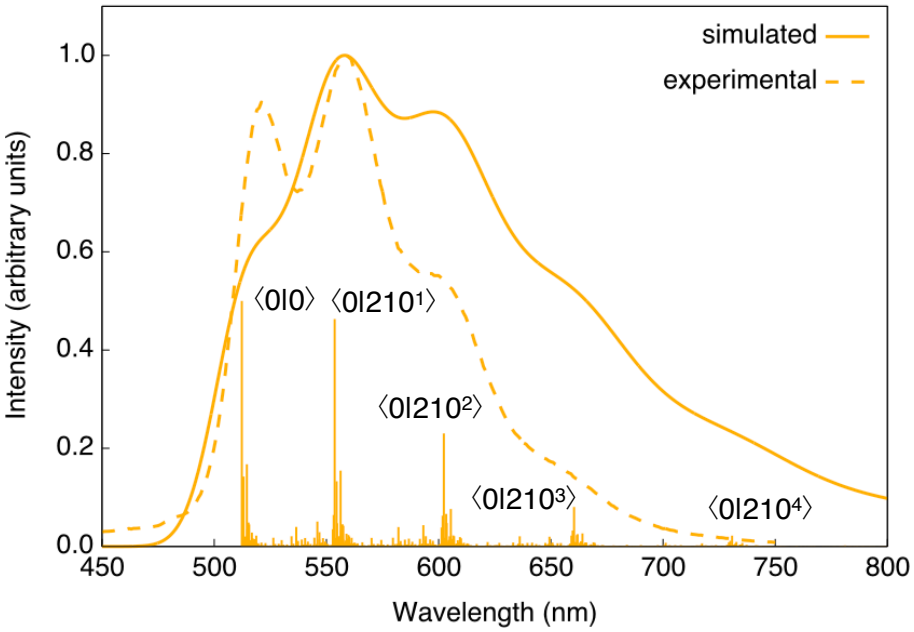

Figure A2.11 Simulated (solid) and experimental (dashed) emission spectra of **3** together with the calculated stick spectrum. Both spectra have been normalized and the calculated spectrum has been blue shifted by 0.12 eV to superimpose the most intense peaks. The 210 normal mode of vibration corresponds to the C=N stretching mode of the imine.

Table A2.8 Energy, wavelength, intensity (arbitrary units), and assignation of the most intense transitions of the calculated stick spectrum of **1**, blue-shifted by 0.09 eV.

λ / nm	ΔE / eV	Intensity	Assignation
486	2.55	0.50	**<0|0>**
486	2.55	0.08	<0|2^1>
487	2.55	0.09	<0|5^1>
487	2.55	0.07	<0|6^1>
488	2.54	0.09	<0|20^1>
516	2.40	0.05	<0|177^1>
522	2.37	0.33	**<0|202^1>**
565	2.19	0.11	**<0|202^2>**
523	2.37	0.07	<0|203^1>
523	2.37	0.05	<0|202^1;2^1>
523	2.37	0.06	<0|202^1;5^1>
525	2.36	0.06	<0|202^1;20^1>

Table A2.9 Energy, wavelength, intensity (arbitrary units), and assignation of the most intense transitions of the calculated stick spectrum of **2**, blue-shifted by 0.12 eV.

λ / nm	ΔE / eV	Intensity	Assignation
503	2.46	0.49	**<0|0>**
503	2.46	0.09	<0|5^1>
503	2.46	0.07	<0|6^1>
505	2.46	0.10	<0|20^1>
535	2.32	0.05	<0|179^1>
542	2.29	0.50	**<0|204^1>**
589	2.11	0.28	**<0|204^2>**
643	1.93	0.11	**<0|204^3>**
544	2.28	0.05	<0|212^1>
543	2.28	0.10	<0|204^1;5^1>
590	2.10	0.05	<0|204^2;5^1>
543	2.28	0.08	<0|204^1;6^1>
545	2.28	0.10	<0|204^1;20^1>
592	2.10	0.06	<0|204^2;20^1>
590	2.10	0.06	<0|212^1;204^1>

Table A2.10 Energy, wavelength, intensity (arbitrary units), and assignation of the most intense transitions of the calculated stick spectrum of **3**, blue-shifted by 0.12 eV.

λ / nm	ΔE / eV	Intensity	Assignation
512	2.42	0.50	**<0|0>**
513	2.42	0.14	<0|6^1>
515	2.41	0.17	<0|21^1>
546	2.27	0.05	<0|182^1>
553	2.24	0.06	<0|209^1>
554	2.24	0.46	**<0|210^1>**
602	2.06	0.23	**<0|210^2>**
660	1.88	0.08	**<0|210^3>**
555	2.24	0.13	<0|210^1;6^1>
603	2.05	0.07	<0|210^2;6^1>
556	2.23	0.15	<0|210^1;21^1>
605	2.05	0.08	<0|210^2;21^1>
602	2.06	0.06	<0|210^1;209^1>

Table A2.11 Vibration normal modes that contribute to the simulated emission spectra together with their frequencies and nature.

Complex	NMV	Frequency / cm^{-1}	Assignation
1	2	20.2	PPh_3
	5	28.1	PPh_3
	6	28.7	PPh_3
	20	87.5	PPh_3
	177	1203.9	C_{Ph}-C_{Ir}
	202	1439.8	C_{py}-N
	203	1468.9	C_{Ir}=N
2	5	28.5	PPh_3
	6	29.0	PPh_3
	20	86.7	PPh_3
	179	1203.7	C_{Ph}-C_{Ir}
	204	1450.5	C_{Ir}=N
	212	1494.1	C_{py}-N
3	6	28.2	PPh_3
	21	84.8	PPh_3
	182	1203.5	C_{Ph}-C_{Ir}
	209	1444.4	C_{py}=N & CH_3 umbrella
	210	1458.9	C_{Ir}=N & CH_3 umbrella

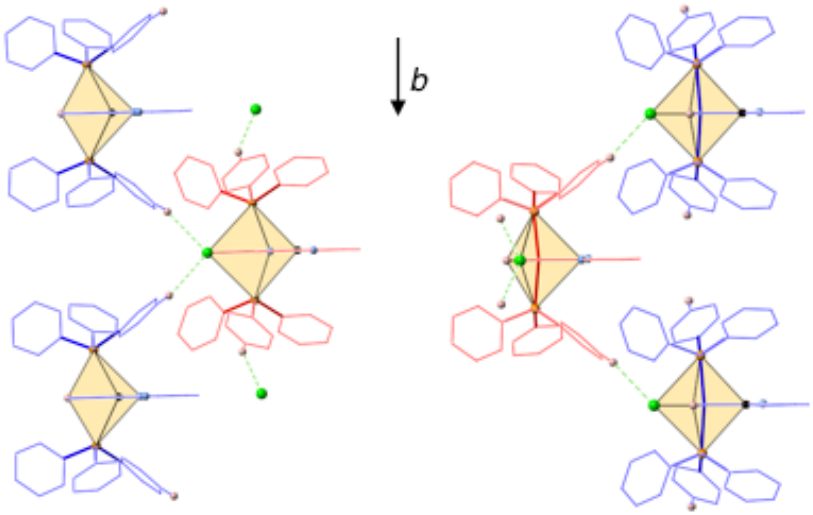

Figure A2.12 Side view of the C-H···Cl interactions of **2** shown in Figure 2.42 between a complex in the reference chain (red) and complexes of the blue chains.

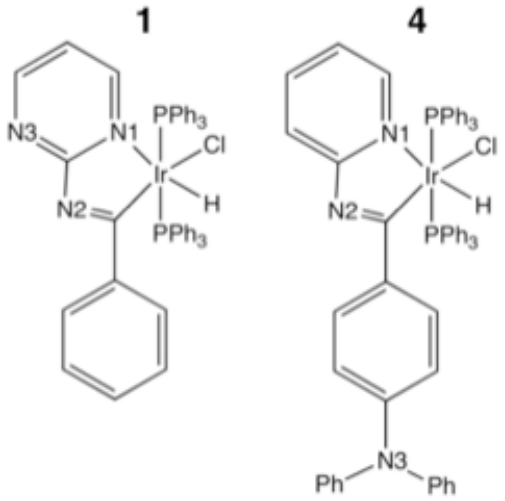

Figure A2.13 Complexes **1** and **4** with labels for N atoms corresponding to protonated sites given in Table A2.12.

Table A2.12 Relative energies (in kcal/mol) of different protonated forms of complexes **1** and **4** (Figure A2.13).

complex	Protonated site	
	N2	N3
1	0.0	12.3
4	0.0	35.2

Table A2.13 Selected geometrical parameters for the iridium's coordination environment and the imine group (C-N, N=C and C-C) for the optimized S_0 and T_1 states of **2H**. Δ indicates the differences of the optimized S_0 geometrical parameters of **2H** relative to the original optimized S_0 of **2**. The δ dihedral angle corresponds to the N=C_1-C_2-C_3 atoms shown in Figure 2.46.

geometry	bond lengths (Å)							
	Ir-C	Ir-Cl	Ir-N	Ir-H	Ir-P	C-N	N=C	C-C
S_0	1.965	2.491	2.213	1.585	2.443	1.397	1.362	1.474
T_1	2.064	2.401	2.188	1.588	2.459	1.357	1.394	1.439
Δ	-0.056	-0.070	0.037	-0.016	0.043	0.024	0.039	-0.020

geometry	angles (º)			
	C-Ir-Cl	N-Ir-H	P-Ir-P	δ
S_0	176	174	168	22
T_1	163	157	175	21
Δ	5	-1	0	22

8. AIE in an Ir(III) complex with a Schiff base ligand

8.1 Introduction

Our experimental collaborators synthesized a new Ir(III) complex[184] (Figure 2.38) with two cyclometalating ppy ligands and a Schiff base (SB) ancillary ligand with an N^O coordination to the metal center. From now on, we will refer to this complex as [Ir(N^O)]. This complex exhibited AIE in aggregates formed in solution and in solid state samples, with the emission wavelength red-shifted with respect to that observed in dilute solutions.

Due to the AIE effect, this compound turned out to have a potential application as a non-toxic bio-imaging probe for mitochondrial staining. In particular, [Ir(N^O)] was successfully employed by our collaborators as a bio-imaging agent, which selectively stains the mitochondria. This is of notable interest since specific imaging of mitochondria has a great importance in the biomedical field.[185,186]

Our goal herein was to characterize the excited states of [Ir(N^O)] and try to elucidate the origin of the observed AIE by considering the environment in our calculations. In particular, we aimed to understand if intermolecular interactions in the crystal are responsible for a change in the nature of the emitting state and if they are related to the blocking of non-radiative pathways. The [Ir(N^O)] complex is very similar to one of the complexes discussed for the Ir(III) AIE controversy in the introduction of this chapter,[105] where instead of a pyridine group bonded to the iminic nitrogen there was a phenyl ring. Let us just recall that the authors of this study arrived to the conclusion that for their system, RIR was the mechanism behind the observed AIE effect.

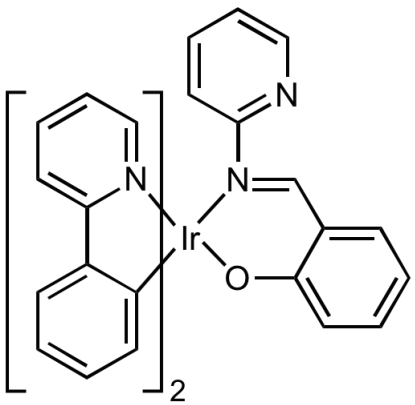

Figure 2.38 Investigated complex referred to as [Ir(N^O)].

8.2 Ground state geometries

The ground state optimized geometry of [Ir(N^O)] exhibits a distorted octahedral coordination environment for the iridium atom (Table 2.19). There are significant differences between the SB ligand at the optimized S_0 geometry and the monomer extracted from the experimental X-ray crystal structure, likely due to intermolecular interactions in the crystal. In particular, the Ir-N_{SB} bond length is 0.09 Å larger in the optimized geometry and the pyridine ring is ~10º closer to planarity with the entire SB ligand. The optimized geometry of [Ir(N^O)] when simulating the presence of the crystal environment (see computational details) does, however, not show any significant structural difference with respect to the molecular geometry optimized in vacuum.

Table 2.19 Selected bond lengths (in Å) and dihedral angles (in º) of [Ir(N^O)] where δ_1 and δ_2 correspond to the dihedral angles N_{SB}-Ir-O-C and N_{py}=C_{py}-N_{SB}=C_{SB}, respectively (where py refers to pyridine ring).

geometry	Ir-C*	Ir-N*	Ir-O	Ir-N_{SB}	C_{SB}=N_{SB}	N_{SB}-C_{py}	δ_1	$\lvert\delta_2\rvert$
monomer	2.009	2.063	2.152	2.155	1.293	1.429	10	66
S_0 isolated	2.016	2.072	2.181	2.243	1.310	1.424	12	54
T_1 isolated	2.024	2.074	2.147	2.211	1.373	1.398	36	31
S_0 environment	2.017	2.079	2.179	2.239	1.308	1.425	13	56
T_1 environment	2.022	2.080	2.152	2.215	1.366	1.406	19	44

*average value

8.3 Molecular orbitals

The HOMO of [Ir(N^O)] shows contributions from a d orbital of the iridium atom together with a π-type orbital of the SB ligand, in which there is minor participation of the pyridine ring (Figure 2.39). The HOMO-1 and HOMO-2 mainly correspond to t_{2g}-type orbitals of the iridium atom with small participation from the SB and ppy ligands, while the HOMO-3 can be described as a π-type orbital delocalized over both ppy ligands. The LUMOs have almost no metal participation and they are basically π*-type orbitals of both ppy ligands (LUMO, LUMO+2 and LUMO+3), except for the LUMO+1, which is a π*-type orbital of the SB ligand, with a bonding interaction in the iminic nitrogen N-C_{py} bond.

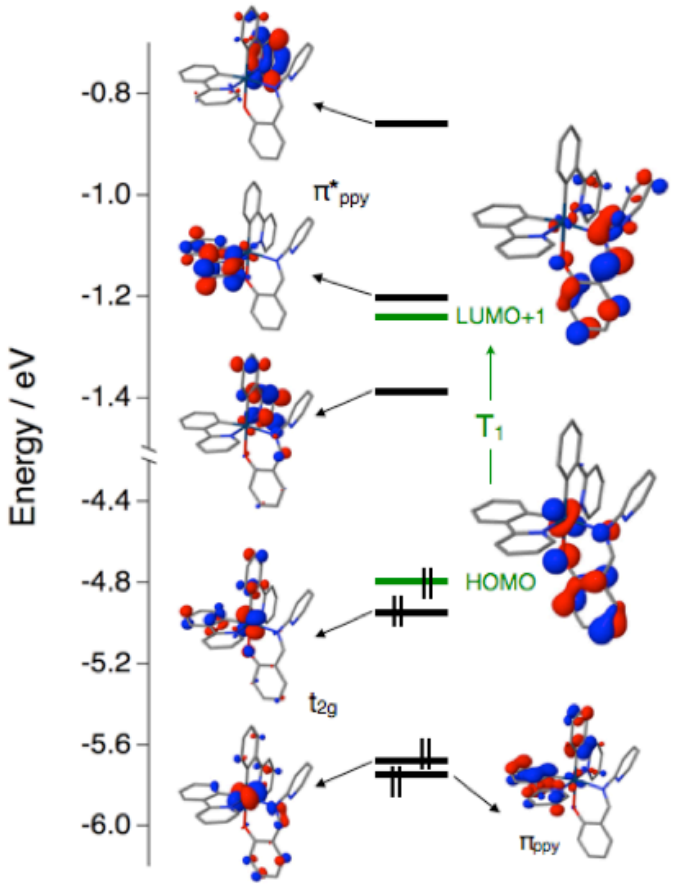

Figure 2.39 Frontier MO diagram of [Ir(N^O)]. The two orbitals (HOMO and LUMO+1) involved in the S_0 to T_1 transition are indicated in green.

8.4 Absorption and emission in solution

The UV-Vis absorption spectrum of [Ir(N^O)] recorded in degassed DCM is shown in Figure 2.40. Electronic structure calculations at the TDDFT level identify the intense absorption band below 320 nm as originated from spin-allowed LC transitions on the ppy moieties (HOMO-3→LUMO+2 in Figure 2.39). The lowest LC (π→π*) transition is computed at 314 nm, in fairly good agreement with the experimental band onset. The moderately intense broad absorption band between 320-450 nm corresponds to the convolution of the transitions to the lowest excited singlet states. The vertical transition energies to the three lowest optically active singlet states are shown in Table 2.20. The lowest spin singlet state can be characterized as a metal-ligand to ligand charge transfer (^{1}MLLCT) state, mainly corresponding to the HOMO→LUMO excitation involving the SB and ppy ligands. The second excited singlet is mainly obtained as an HOMO-1→LUMO electronic promotion with ^{1}MLCT (where L=ppy) character, while the third computed singlet corresponds to the HOMO→LUMO+1 transition with important participation of the π-orbitals on the SB ligand, with mixed MLCT and LC character. Inspection of the long wavelength range of the absorption spectra unravels a very weak

absorption tail beyond 450 nm. We associate the origin of this band to spin-forbidden transitions to the lowest ^{3}MLCT/LC state and the two triplet states with mixed MLCT and MLLCT character, respectively computed at 557, 492 and 465 nm.

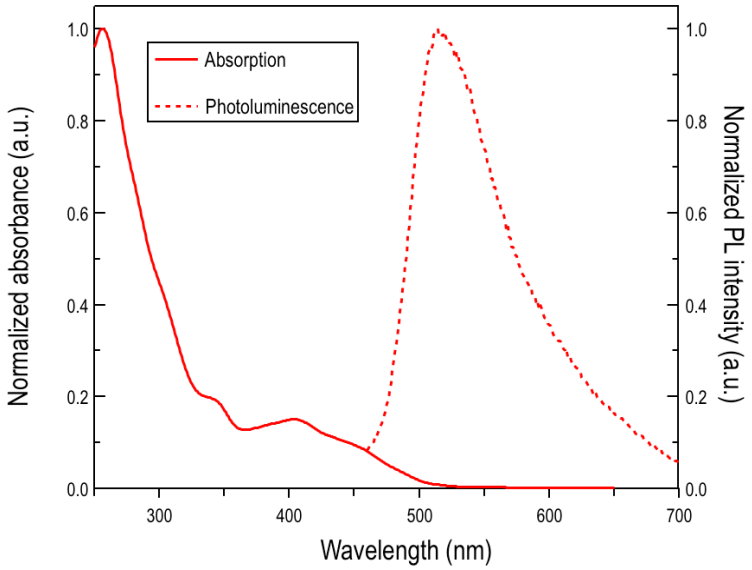

Figure 2.40 UV/Vis absorption (solid lines) and PL (dashed lines) spectra of [Ir(N^O)] in DCM solution (10^{-5}M).

Table 2.20 Vertical excitation energies and wavelengths, oscillator strengths (*f*), character, and composition for the lowest electronic transitions of [Ir(N^O)].

state	character	ΔE / eV	λ / nm	*f*	composition
S_1	MLLCT	2.73	454	0.009	H→L (81%)
S_2	MLCT	2.86	434	0.020	H-1→L (78%)
S_3	MLCT/LC	2.93	423	0.023	H→L+1 (73%)
T_1	MLCT/LC	2.23	557	-	H→L+1 (69%)
T_2	MLCT/MLLCT	2.52	492	-	H-1→L (51%), H→L (25%)
T_3	MLCT/MLLCT	2.67	465	-	H-1→L+2 (67%)

After photoexcitation, [Ir(N^O)] is expected to relax down to its lowest triplet state, from where it can eventually decay back to the ground state by phosphorescent emission. Upon excitation at 365 nm at room temperature, [Ir(N^O)] showed weak emission in degassed DCM solution with λ_{max} = 515 nm (Figure 2.40).

The most significant geometrical changes with respect to the Frank-Condon structure due to the molecular relaxation on the T_1 PES are on the Schiff base ligand (Table 2.19). Upon occupation of the LUMO+1, the pyridine ring twists in an attempt to planarize with the imine unit because of the favorable π-bonding C_{py}-N_{SB} interaction (Figure 2.41). Naturally,

due to the torsional strain imposed by the coordinated bidentate ligand, complete planarization is not accomplished, and the N_{py}-C_{py}-N_{SB}=C_{SB} dihedral angle decreases ~25º up to a value of 31º (Table 2.19). Concomitantly, a decrease of ~0.03 Å of the N_{SB}-C_{py} bond length and an increase of ~0.06 Å of the iminic C=N bond length takes place. The partial planarization of the pyridine ring with the imine unit increases the strain in the phenolate fragment, in particular, the N_{SB}-Ir-O-C dihedral angle increases ~25º to a value of 36º. The modifications in the iridium's coordination environment are less pronounced for the ppy ligands, since the orbitals involved in the electronic transition are mainly located on the SB ligand, and the only significant changes are in the Ir-O and Ir-N_{SB} bond lengths, which decrease ~0.03 Å. Similar structural rearrangements were recently reported for a series of cyclometalated complexes with general formula [Ir(C^N)$_2$(N^O)], for which distortions of the bonding of the six-membered chelate ring of the ancillary ligand in the T_1 optimized geometry were observed.[107]

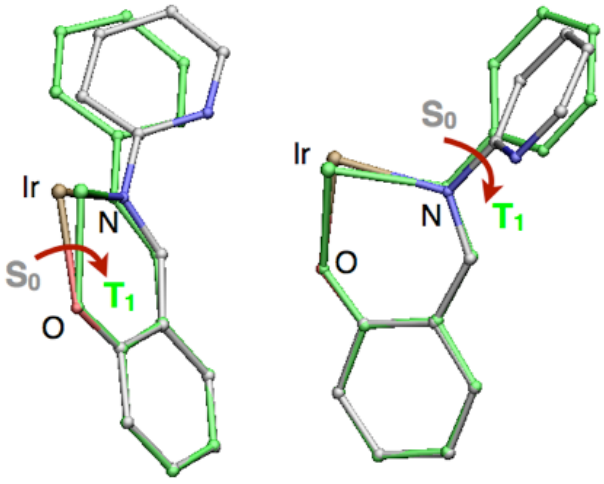

Figure 2.41 Superposition between S_0 and T_1 optimized geometries for [Ir(N^O)].

8.5 Aggregation induced emission

In spite of exhibiting very weak phosphorescent intensities in common organic solvents, the photoluminescence intensity of [Ir(N^O)] increased very rapidly upon aggregation and the compound was highly emissive in solid state (Figure 2.42). However, the emission band maximum in solid state was red-shifted to 610 nm with respect to [Ir(N^O)] in methanol (515 nm). This ref-shift was also observed for the aggregates formed in solution. The maximum emission intensity of [Ir(N^O)] in methanol with 95% of water fraction was recorded at 605 nm, very close to the emission in the solid state.

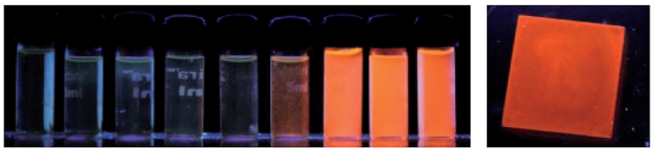

Figure 2.42 Photographs of [Ir(N^O)] in methanol with different water fractions (left) and solid-state sample emission (right). Taken from reference 184.

8.5.1 Delocalization effects

In order to identify the origins of the AIE of the studied compounds, we turn our attention to the crystal structure. The main differences of the molecular geometry of [Ir(N^O)] in the crystal structure with respect to the optimized ground state are found at the Schiff base ligand (Table 2.19). In the crystal however, the complexes are packed into dimers, with potential π-π interactions between two ppy ligands from two adjacent molecules (Figure 2.43). These interactions might modify the nature and ordering of the low-lying electronic states in the solid with respect to solution. It is important to point out that these dimers are isolated, that is, they do not form chains of π-stacked molecules in the crystal.

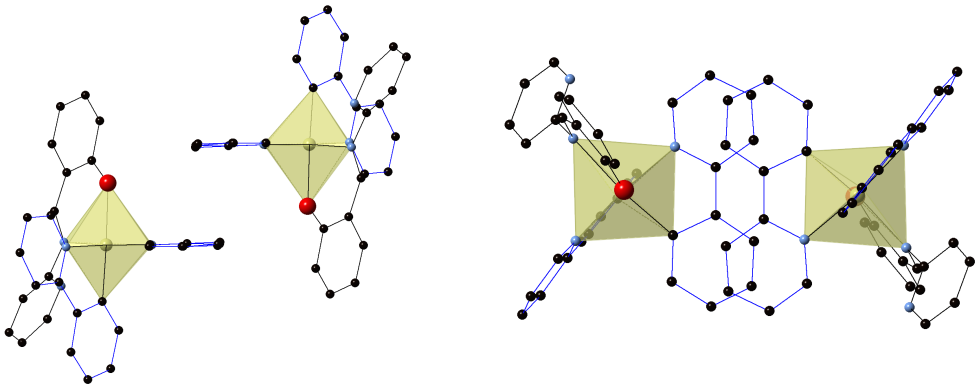

Figure 2.43 Dimers present in the crystal structure of [Ir(N^O)]. Distance between the π-stacked ppy ligands is ~3.5 Å.

The potential π-π interactions between ppy ligands might modify the electronic structure of the triplet state manifold, resulting in the different emission properties with respect to the lowest triplet state in solution. Calculations for the dimer indicate that the vertical excitations to the T_1 and T_2 states are 2.28 eV. This value is very close to that for the T_1 state of the monomer (2.27 eV), which is analogous to the HOMO→LUMO+1 triplet of the optimized ground state. Therefore, these T_1 and T_2 states correspond to ^{3}MLCT/LC states localized on a single molecule of the dimer. For the higher-lying triplet states of the dimer (T_5 and T_6), visualization of the NTOs (Figures 3.44 and 3.45) seems to indicate that there is electronic coupling between the monomers, since they exhibit sizable π-π

interactions with electron/hole delocalization over the two molecular species. However, the excitation energy to both states is 2.72 eV, very close to that of the T_3 state of the monomer (2.68 eV). Thus, the T_5 and T_6 states can be described in a first approximation as linear combinations of the T_3 states of each monomer. The 0.04 eV difference between the excitation energy of the monomer (T_3) and the dimer (T_5 and T_6) might be due to minor CT contributions between adjacent ppy ligands. Nevertheless, these states of the dimer are 0.45 eV above the T_1 state responsible for phosphorescence. It seems difficult to suppose that relaxation after absorption in the crystal will be able to overcome such a large gap, so that the T_5 (or T_6) state becomes the emitting state. These results seem to rule out the possibility of a change in the electronic nature of the emitting state in the dimer as the source for the observed AIE. In particular, because the T_1 state of the dimer is localized on a single molecule and its nature is analogous to that of the T_1 state of the complex in solution.

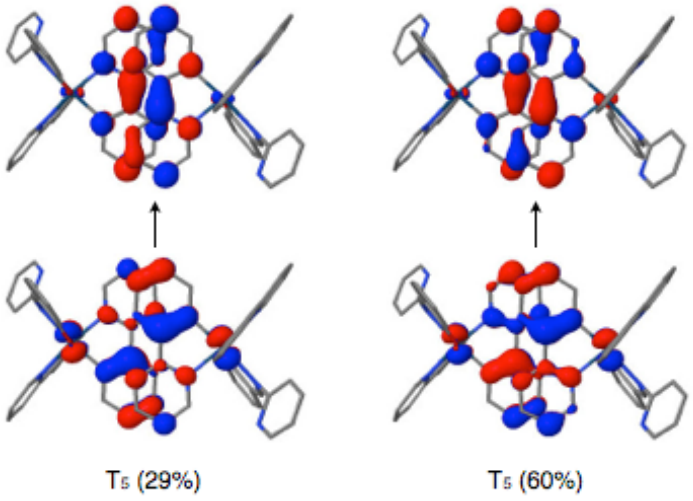

Figure 2.44 NTOs corresponding to the T_5 state of the [Ir(N^O)] dimer from the crystal structure.

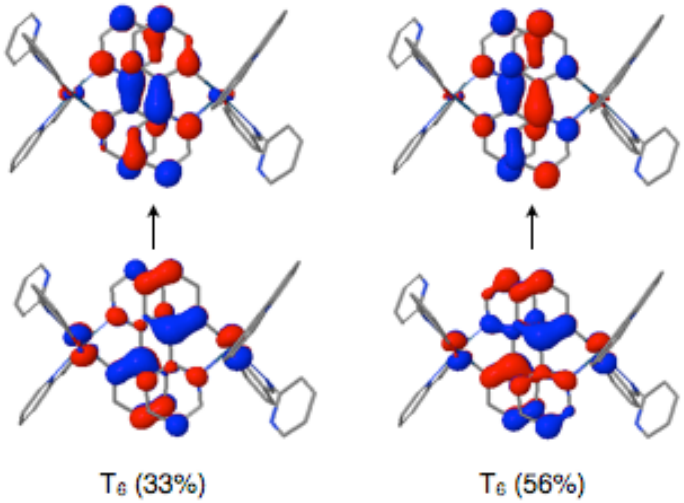

Figure 2.45 NTOs corresponding to the T_6 state of the [Ir(N^O)] dimer from the crystal structure.

8.5.2 Restriction of internal rotations

As already mentioned, upon relaxation on the T_1 PES, the pyridine ring of the SB ligand tends to planarize with the rest of the conjugated system. Such nuclear motion could be related to the RIR mechanism for AIE. Thus, we wanted to explore how the torsion of the pyridine ring might be affected by the presence of the environment in the crystal. To this end, we modeled the environment by selecting the nearest neighbors to a given monomer of the crystal (Figure 2.46). The cluster was treated computationally with the ONIOM method,[143,144] where the central complex (in red in Figure 46a) was described at the QM level, while the environment (in grey) at the MM level. Starting from the crystal cluster, we considered the rotation of the pyridine ring of the QM complex by performing a relaxed scan (i.e. optimizing the T_1 state of the central complex subject to the torsion constraint), while keeping a frozen environment. In order to quantify the effect of the environment on such torsion, we compare the energy profile relaxed for the case including the environment, with the energy of the central QM metal complex at the same geometries.

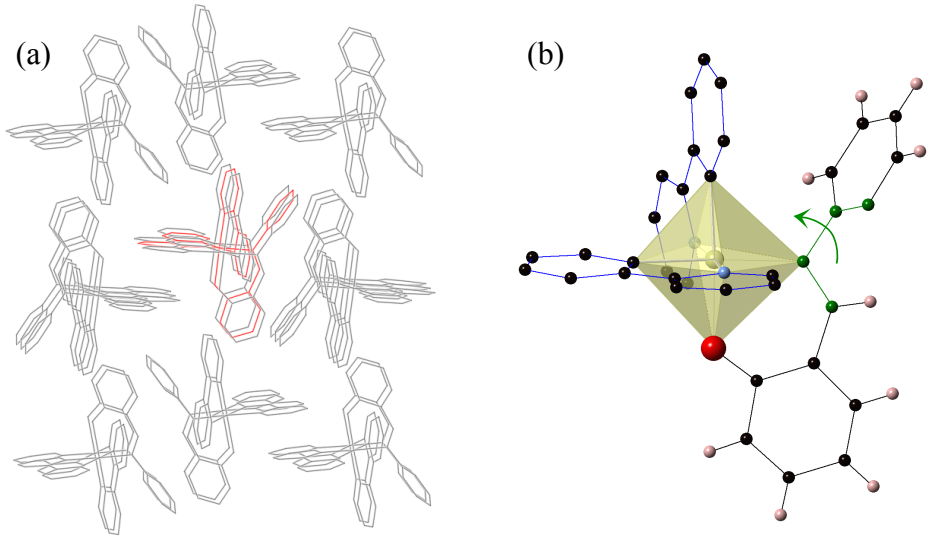

Figure 2.46 (a) Nearest neighbors model from the crystal structure of [Ir(N^O)] with central complex treated at the QM level (red) and environment at the MM (grey). (b) Torsion of the pyridine ring from the SB ligand.

The torsion profiles of the S_0 and T_1 states for the isolated complex and the complex embedded in the crystal environment are shown in Figure 2.47, where it is evident that the torsion energy profiles of S_0 and T_1 are barely affected by the environment. These results indicate that the crystal environment does not block the pyridine ring rotation, thus it seems not to be directly involved in the origin of the observed AIE.

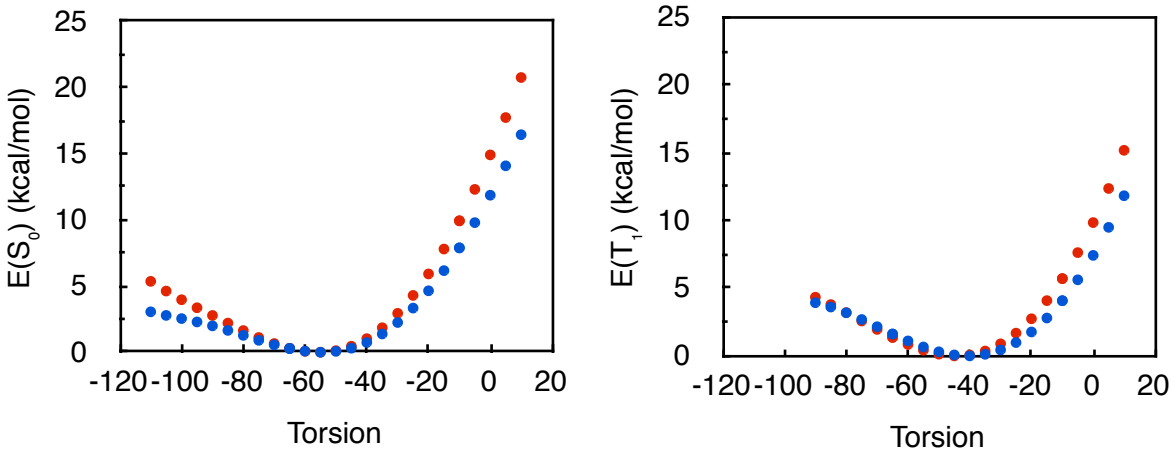

Figure 2.47 Potential energy scans for S_0 and T_1 along the N_{py}=C_{py}-N_{SB}=C_{SB} dihedral angle. Blue curves correspond to the QM energy of the central complex shown in red in Figure 2.46, while red ones include the environment with ONIOM. The geometries along the torsion are relaxed for the ONIOM calculation.

8.5.3 T_1 relaxation with environment

In the search for a mechanism explaining the AIE observed for [Ir(N^O)], we now consider how the environment in the crystal might affect the structural relaxation of the T_1 state (Figure 2.46a). We optimized the T_1 state for the central metal complex at the QM level keeping a frozen environment at the MM level. The coordination environment of the iridium atom in the T_1 state is barely affected by the presence of the environment in our model, but the SB ligand is indeed affected (Table 2.19). Our calculations reveal that when we consider the environment, the Ir(III) complex is not able to fully relax. In particular, for the isolated complex, the N_{py}=C_{py}-N_{SB}=C_{SB} dihedral angle decreased from 54º to 31º from the FC geometry to the T_1 minimum. When considering the environment, the pyridine ring suffers a minor planarization and the obtained dihedral angle is 44º. Focusing on the phenolate fragment, the N_{SB}-Ir-O-C dihedral angle increased from 12º to 36º when relaxing on the T_1 PES of the isolated complex, but the environment restricts such motion and the angle suffers a minor increase to 19º. These results point out that the complex in the crystal is not able to fully relax due to restrictions imposed by the neighboring molecules. However, the red-shift in the emission energy observed experimentally for the solid state cannot be explained by these results. In particular, our calculation predicts a 0.15 eV blue-shift in the vertical emission of T_1 when we include the environment relative to the isolated case.

8.5.4 Non-radiative decay

In case the emitting state of the studied complex does not change its electronic nature upon aggregation, and considering that the environment in the crystal does not affect the rate of ISC from the singlet to the triplet manifold, the emission efficiency is then related to the relative rates of radiative and non-radiative decay processes from the lowest excited triplet to the ground state. To further explore how the intermolecular interactions in the crystal structure might modify the PL intensities of [Ir(N^O)], we analyze the impact that the molecular environment has on the vibrational landscape of the molecule. To this end we compute the HR factors of [Ir(N^O)] in two situations: (i) isolated complex and (ii) considering the crystal environment with the cluster model of Figure 2.46a.

The HR factors for complex [Ir(N^O)] computed in the gas phase and in the crystal environment are shown in Figure 2.48. In general, the HR factors are much larger in the gas phase than in the presence of the crystal environment, indicating a strong influence of intermolecular interactions. For the isolated molecule, there are a fairly large number of vibrational modes with large HR values, especially in the low frequency range (< 1500 cm^{-1}). These modes correspond to collective torsions and rotations of the ligands. It is also worth noticing the presence of a high frequency mode (~3200 cm^{-1}) with a HR factor of 0.1, which corresponds to C-H stretching modes on the SB ligand. The HR factors in the solid state are almost an order of magnitude smaller than for the isolated molecule. These results evidence how the crystal environment hinders intramolecular motions, difficulting the non-radiative conversion of electronic energy into the vibrational degrees of freedom.

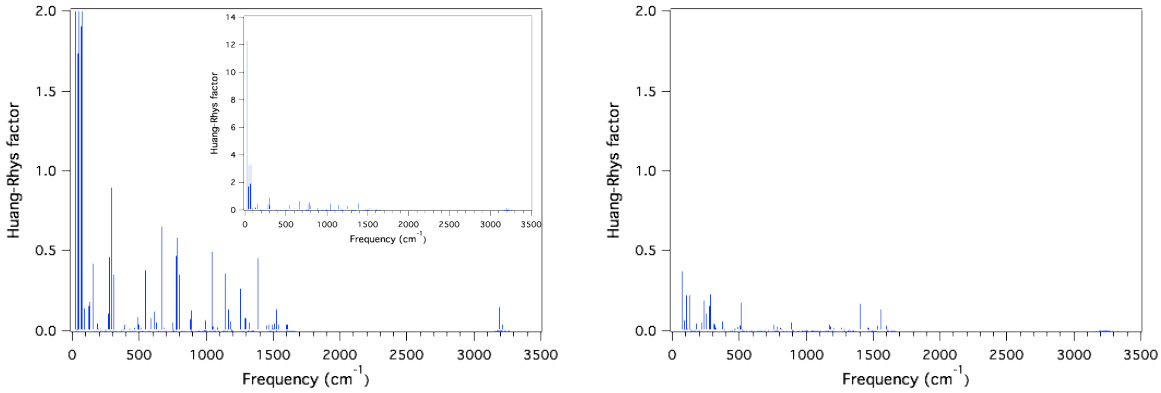

Figure 2.48 HR factors of [Ir(N^O)] computed in gas phase (left) and in the crystal (right).

In order to confirm that the harmonic approximation is valid for the normal modes of [Ir(N^O)], we calculated the reorganization energies of the S_0 and T_1 states by two

different routes. From the HR factors of each normal mode, the total reorganization energy may be estimated from the following expression

$$\lambda = \sum_i \lambda_i = \sum_i \hbar\omega_i HR_i \qquad (2.17)$$

On the other hand, the total reorganization energies of each state can also be calculated directly by performing single point calculations for the S_0 and T_1 minima. We refer to this approach as adiabatic. The total reorganization energies calculated by these two approaches are gathered in Table 2.21. For the solid state, both approaches yield very close values, but for the isolated complex in the gas phase, the reorganization energies calculated from the HR factors are largely overestimated. This results suggest that the harmonic approximation fails in the vacuum calculations. We suspect that those modes giving rise to very large HR factors (Figure 2.48) are highly anharmonic and thus responsible for such discrepancy. For this reason, at least for this system, we cannot calibrate the importance of certain modes in the non-radiative decay due to the failure of the harmonic approximation in the isolated case. In the solid state, the approximation holds probably because the environment does not allow very large displacements along the modes and anharmonic effects will be smaller.

Table 2.21 Total reorganization energies (λ) for the S_0 and T_1 states calculated via adiabatic energy differences and HR factors.

λ (kcal/mol)	vacuum		solid state	
approach	adiabatic	HR	adiabatic	HR
S_0	6.6	17.3	4.3	4.2
T_1	5.6	22.9	4.7	4.7

8.6 Conclusions

The weak emission of [Ir(N^O)] in solution has been assigned to a ^{3}MLCT/LC state on the SB ligand. The lowest triplet state of the [Ir(N^O)] dimer is localized on one of the molecules, and higher-lying states are found to have some degree of electronic coupling between monomers. The existence of a novel electronic state due to molecular aggregation seems unfeasible, at least within the computational level employed. Possible candidates of delocalized electronic triplet states of aggregate species appear higher in energy compared to the T_1 (phosphorescent) state. Moreover, a blue-shift in the emission energy is obtained when the triplet state of a complex is optimized with the surrounding environment of the crystal. Therefore, our calculations are not able to explain the red-shift of the emission in

the solid state. The involvement of the pyridine ring rotation in a RIR mechanism to explain the observed AIE has been ruled out by considering environment effects. Our attempt to quantify which normal modes may be responsible for non-radiative decay in vacuum compared to in the crystal has not worked out since the harmonic approximation seems to fail for the modes of the isolated complex. The analysis of the HR factors allows to identify those modes (mainly low frequency ones) that undergo an important change upon aggregation, but we cannot quantitatively trust on the considered harmonic approximation.

8.7 Computational details

Electronic structure calculations have been performed within the DFT and TDDFT frameworks with the B3LYP energy functional,[111,112] a basis set of double-ζ quality (LANL2DZ) and the ECP of Hay and Wadt for iridium,[120] while the standard 6-31G(d) basis set was used for the rest of the atoms in the complex. Geometry optimizations of the S_0 and T_1 states were performed for the case of the isolated complex and considering effects of the crystal environment. Environment effects were taken into account by carrying out ONIOM calculations[143,144] of the cluster model (Figure 2.46), where the central complex was treated at QM level and the remaining environment was treated at MM level with the Universal Force Field (UFF).[187] Within the ONIOM calculations, when the geometry of the central complex was optimized or a relaxed scan was performed for this central complex, the MM environment was kept frozen at the fixed geometry of the crystal structure. Frequency calculations on the S_0 and T_1 minima for the two situations (isolated complex and considering the environment) were performed within the harmonic approximation. All ONIOM calculations were carried out with mechanical embedding. The relaxed scan curves were checked with electrostatic embedding and the same profile as with mechanical embedding was obtained. The HR factors were determined from the Duschinsky transformation[132,133] between the normal modes of the S_0 and T_1 states. All calculations have been done in the vacuum with no solvent effects and with the Gaussian 09 program.[131]

9. General Conclusions

The main conclusions drawn from the studies of this chapter are summarized in the following lines.

By changing the nature of the coordinating ligands to the Ir(III) center the emission color can be easily tuned. When one ppy unit is replaced in [Ir(ppy)$_3$] by a diphosphine ligand in section 4.1, the emission color shifts from green to blue because the diphosphine ligand is not involved in the T_1 state and so it is less delocalized over the ppy ligands. The binding mode of the diphosphine ligand (either mono or bichelating) does not alter the emission color, that arises from a ^{3}MLCT state.

For the complexes with axial PPh_3 ligands in section 5, an increase in the π-conjugation of the cyclometalating ligand results in a red-shift in the emission energy. These color changes can be traced back to the changes of the frontier molecular orbitals energies. Fluorination on the cyclometalating ppy ligand or modifications on the PPh_3 ligands have a minor effect on the emission color, since the latter do not have an active participation in the T_1 state. The nature of the emitting states is of mixed MLCT/LC/LLCT character.

The vibronic progression in the emission spectra of the studied complexes in section 6 is due to modes on the bpy cyclometalating ligand, with the emitting state being of mainly MLCT character. The presence of PPh_3 ligands plays an important role in the AIE phenomenon, since they are involved in noncovalent interactions in the crystal structure, namely of C-H···π, C-H···Cl and C-H···F types.

The presence of a Schiff base ligand in the complexes of section 7 gives rise to many interesting properties. The emitting state of all complexes is ^{3}MLLCT/LC while one of the complexes exhibits dual emission from an ^{1}ILCT state. Calculations are able to reproduce the vibronic progressions of the experimental emission spectra, which are due to the C=N stretching mode of the iminic nitrogen. Weak interactions present in the crystal of C-H···π and C-H···Cl type seem to be responsible for the restriction of motions in solid state giving rise to AIE. Protonation of these complexes changes the nature of the emitting state as rationalized by our calculations.

The origin of AIE for the [Ir(N^O)] complex is still not resolved. The Schiff base ligand (N^O) suffers an important geometrical distortion when relaxing on the T_1 PES, compared to the ground state geometry, and this distortion is hindered when the environment is taken into account. However, we were unable to reproduce the red-shift in the emission color experimentally measured. Our calculations suggest that the RIR mechanism related to the pyridine ring of the Schiff base ligand does not seem to be responsible for the observed AIE. A change in the nature of the emitting state was also considered by calculating dimers from the crystal. However, the T_1 state is found to be equivalent to that in solution, and delocalized excited states with π-interactions between ppy ligands are found to be too high in energy. The analysis of the HR factors allows to identify which modes are modified by the presence of the environment, but for the isolated complex, the harmonic approximation does not hold and thus, in our opinion, definite conclusions related to the non-radiative process cannot be drawn from these results.

10. References

(1)Hong, Y.; Lam, J. W. Y.; Tang, B. Z. *Chem. Commun.* **2009**, 4332.
(2)Luo, J.; Xie, Z.; Lam, J. W. Y.; Cheng, L.; Chen, H.; Qiu, C.; Kwok, H. S.; Zhan, X.; Liu, Y.; Zhu, D.; Tang, B. Z. *Chem. Commun.* **2001**, 1740.
(3)Birks, J. B. *Rep. Prog. Phys.* **1975**, *38*, 903.
(4)Yuan, W. Z.; Lu, P.; Chen, S.; Lam, J. W. Y.; Wang, Z.; Liu, Y.; Kwok, H. S.; Ma, Y.; Tang, B. Z. *Adv. Mater.* **2010**, *22*, 2159.
(5)Mei, J.; Leung, N. L. C.; Kwok, R. T. K.; Lam, J. W. Y.; Tang, B. Z. *Chem. Rev.* **2015**, *115*, 11718.
(6)Mei, J.; Hong, Y.; Lam, J. W. Y.; Qin, A.; Tang, Y.; Tang, B. Z. *Adv. Mater.* **2014**, *26*, 5429.
(7)Huang, J.; Tang, R.; Zhang, T.; Li, Q.; Yu, G.; Xie, S.; Liu, Y.; Ye, S.; Qin, J.; Li, Z. *Chem. - Eur. J.* **2014**, *20*, 5317.
(8)Nie, H.; Huang, J.; Zhao, Z.; Tang, B. Z. In *Aggregation-Induced Emission: Materials and Applications Volume 2*; American Chemical Society: 2016; Vol. 1227, p 173.
(9)Baggaley, E.; Weinstein, J. A.; Williams, J. A. G. *Coord. Chem. Rev.* **2012**, *256*, 1762.
(10)Chan, J.; Dodani, S. C.; Chang, C. J. *Nat. Chem.* **2012**, *4*, 973.
(11)Mauro, M.; Aliprandi, A.; Septiadi, D.; Kehr, N. S.; De Cola, L. *Chem. Soc. Rev.* **2014**, *43*, 4144.
(12)Kwok, R. T. K.; Leung, C. W. T.; Lam, J. W. Y.; Tang, B. Z. *Chem. Soc. Rev.* **2015**, *44*, 4228.
(13)Lee, S.; Yuen, K. K. Y.; Jolliffe, K. A.; Yoon, J. *Chem. Soc. Rev.* **2015**, *44*, 1749.
(14)Zhao, Q.; Li, F.; Huang, C. *Chem. Soc. Rev.* **2010**, *39*, 3007.
(15)Zhan, C.; You, X.; Zhang, G.; Zhang, D. *Chem. Rec.* **2016**, *16*, 2142.
(16)Dong, Y. Q.; Lam, J. W. Y.; Tang, B. Z. *J. Phys. Chem. Lett.* **2015**, *6*, 3429.
(17)Chi, Z.; Zhang, X.; Xu, B.; Zhou, X.; Ma, C.; Zhang, Y.; Liu, S.; Xu, J. *Chem. Soc. Rev.* **2012**, *41*, 3878.
(18)Zhao, Z.; He, B.; Tang, B. Z. *Chem. Sci.* **2015**, *6*, 5347.
(19)Hong, Y.; Lam, J. W. Y.; Tang, B. Z. *Chem. Soc. Rev.* **2011**, *40*, 5361.
(20)Ravotto, L.; Ceroni, P. *Coord. Chem. Rev.*, *in press*.
(21)Wang, W.; Lin, T.; Wang, M.; Liu, T.-X.; Ren, L.; Chen, D.; Huang, S. *J. Phys. Chem. B* **2010**, *114*, 5983.
(22)Zhao, Q.; Li, L.; Li, F.; Yu, M.; Liu, Z.; Yi, T.; Huang, C. *Chem. Commun.* **2008**, 685.
(23)Wu, H.; Yang, T.; Zhao, Q.; Zhou, J.; Li, C.; Li, F. *Dalton Trans.* **2011**, *40*, 1969.
(24)Tong, J.; Wang, Y. J.; Wang, Z.; Sun, J. Z.; Tang, B. Z. *J. Phys. Chem. C* **2015**, *119*, 21875.
(25)Dong, Y.; Lam, J. W. Y.; Qin, A.; Li, Z.; Sun, J.; Sung, H. H. Y.; Williams, I. D.; Tang, B. Z. *Chem. Commun.* **2007**, 40.
(26)Yuan, W. Z.; Shen, X. Y.; Zhao, H.; Lam, J. W. Y.; Tang, L.; Lu, P.; Wang, C.; Liu, Y.; Wang, Z.; Zheng, Q.; Sun, J. Z.; Ma, Y.; Tang, B. Z. *J. Phys. Chem. C* **2010**, *114*, 6090.
(27)Birks, J. B. *Photophysics of Aromatic Molecules*; Wiley-Interscience: London, 1970.
(28)Birks, J. B. *Nature* **1967**, *214*, 1187.
(29)Klessinger, M.; Michl, J. *Excited States in Photochemistry of Organic Molecules*; VCH: New York, 1995.
(30)Chen, J.; Law, C. C. W.; Lam, J. W. Y.; Dong, Y.; Lo, S. M. F.; Williams, I. D.; Zhu, D.; Tang, B. Z. *Chem. Mater.* **2003**, *15*, 1535.
(31)Shi, J.; Chang, N.; Li, C.; Mei, J.; Deng, C.; Luo, X.; Liu, Z.; Bo, Z.; Dong, Y. Q.; Tang, B. Z. *Chem. Commun.* **2012**, *48*, 10675.
(32)Parrott, E. P. J.; Tan, N. Y.; Hu, R.; Zeitler, J. A.; Tang, B. Z.; Pickwell-MacPherson, E. *Mater. Horiz.* **2014**, *1*, 251.
(33)Zhang, G.-F.; Chen, Z.-Q.; Aldred, M. P.; Hu, Z.; Chen, T.; Huang, Z.; Meng, X.; Zhu, M.-Q. *Chem. Commun.* **2014**, *50*, 12058.
(34)Leung, N. L. C.; Xie, N.; Yuan, W.; Liu, Y.; Wu, Q.; Peng, Q.; Miao, Q.; Lam, J. W. Y.; Tang, B. Z. *Chem. - Eur. J.* **2014**, *20*, 15349.
(35)Yin, S.; Peng, Q.; Shuai, Z.; Fang, W.; Wang, Y.-H.; Luo, Y. *Phys. Rev. B* **2006**, *73*, 205409.
(36)Wu, Q.; Deng, C.; Peng, Q.; Niu, Y.; Shuai, Z. *J. Comput. Chem.* **2012**, *33*, 1862.
(37)Wu, Q.; Zhang, T.; Peng, Q.; Wang, D.; Shuai, Z. *Phys. Chem. Chem. Phys.* **2014**, *16*, 5545.
(38)Zhang, T.; Jiang, Y.; Niu, Y.; Wang, D.; Peng, Q.; Shuai, Z. *J. Phys. Chem. A* **2014**, *118*, 9094.

(39)Zhang, T.; Peng, Q.; Quan, C.; Nie, H.; Niu, Y.; Xie, Y.; Zhao, Z.; Tang, B. Z.; Shuai, Z. *Chem. Sci.* **2016**, *7*, 5573.
(40)Yuan, W. Z.; Gong, Y.; Chen, S.; Shen, X. Y.; Lam, J. W. Y.; Lu, P.; Lu, Y.; Wang, Z.; Hu, R.; Xie, N.; Kwok, H. S.; Zhang, Y.; Sun, J. Z.; Tang, B. Z. *Chem. Mater.* **2012**, *24*, 1518.
(41)Shen, X. Y.; Yuan, W. Z.; Liu, Y.; Zhao, Q.; Lu, P.; Ma, Y.; Williams, I. D.; Qin, A.; Sun, J. Z.; Tang, B. Z. *J. Phys. Chem. C* **2012**, *116*, 10541.
(42)Gao, B.-R.; Wang, H.-Y.; Hao, Y.-W.; Fu, L.-M.; Fang, H.-H.; Jiang, Y.; Wang, L.; Chen, Q.-D.; Xia, H.; Pan, L.-Y.; Ma, Y.-G.; Sun, H.-B. *J. Phys. Chem. B* **2010**, *114*, 128.
(43)Hu, R.; Lager, E.; Aguilar-Aguilar, A.; Liu, J.; Lam, J. W. Y.; Sung, H. H. Y.; Williams, I. D.; Zhong, Y.; Wong, K. S.; Peña-Cabrera, E.; Tang, B. Z. *J. PHys. Chem. C* **2009**, *113*, 15845.
(44)Wang, J.; Mei, J.; Hu, R.; Sun, J. Z.; Qin, A.; Tang, B. Z. *J. Am. Chem. Soc.* **2012**, *134*, 9956.
(45)Tseng, N.-W.; Liu, J.; Ng, J. C. Y.; Lam, J. W. Y.; Sung, H. H. Y.; Williams, I. D.; Tang, B. Z. *Chem. Sci.* **2012**, *3*, 493.
(46)Tasso, T. T.; Furuyama, T.; Kobayashi, N. *Chem. - Eur. J.* **2015**, *21*, 4817.
(47)Liang, J.; Shi, H.; Kwok, R. T. K.; Gao, M.; Yuan, Y.; Zhang, W.; Tang, B. Z.; Liu, B. *J. Mater. Chem. B* **2014**, *2*, 4363.
(48)Tong, H.; Dong, Y.; Hong, Y.; Häussler, M.; Lam, J. W. Y.; Sung, H. H. Y.; Yu, X.; Sun, J.; Williams, I. D.; Kwok, H. S.; Tang, B. Z. *J. Phys. Chem. C* **2007**, *111*, 2287.
(49)Wang, Y.; Liu, T.; Bu, L.; Li, J.; Yang, C.; Li, X.; Tao, Y.; Yang, W. *J. Phys. Chem. C* **2012**, *116*, 15576.
(50)Tong, H.; Dong, Y.; Hau; Lam, J. W. Y.; Sung, H. H. Y.; Williams, I. D.; Sun, J.; Tang, B. Z. *Chem. Commun.* **2006**, 1133.
(51)Levitus, M.; Schmieder, K.; Ricks, H.; Shimizu, K. D.; Bunz, U. H. F.; Garcia-Garibay, M. A. *J. Am. Chem. Soc.* **2001**, *123*, 4259.
(52)An, B.-K.; Lee, D.-S.; Lee, J.-S.; Park, Y.-S.; Song, H.-S.; Park, S. Y. *J. Am. Chem. Soc.* **2004**, *126*, 10232.
(53)Ren, Y.; Dong, Y.; Lam, J. W. Y.; Tang, B. Z.; Wong, K. S. *Chem. Phys. Lett.* **2005**, *402*, 468.
(54)Kohmoto, S.; Tsuyuki, R.; Hara, Y.; Kaji, A.; Takahashi, M.; Kishikawa, K. *Chem. Commun.* **2011**, *47*, 9158.
(55)Qian, Y.; Li, S.; Zhang, G.; Wang, Q.; Wang, S.; Xu, H.; Li, C.; Li, Y.; Yang, G. *J. Phys. Chem. B* **2007**, *111*, 5861.
(56)Wei, R.; Song, P.; Tong, A. *J. Phys. Chem. C* **2013**, *117*, 3467.
(57)Maity, A.; Ali, F.; Agarwalla, H.; Anothumakkool, B.; Das, A. *Chem. Commun.* **2015**, *51*, 2130.
(58)Liu, Y.; Tao, X.; Wang, F.; Shi, J.; Sun, J.; Yu, W.; Ren, Y.; Zou, D.; Jiang, M. *J. Phys. Chem. C* **2007**, *111*, 6544.
(59)Qin, A.; Jim, C. K. W.; Tang, Y.; Lam, J. W. Y.; Liu, J.; Mahtab, F.; Gao, P.; Tang, B. Z. *J. Phys. Chem. B* **2008**, *112*, 9281.
(60)Zhao, Z.; Chen, S.; Lam, J. W. Y.; Wang, Z.; Lu, P.; Mahtab, F.; Sung, H. H. Y.; Williams, I. D.; Ma, Y.; Kwok, H. S.; Tang, B. Z. *J. Mater. Chem.* **2011**, *21*, 7210.
(61)Xu, F.; Yuan, M.-S.; Wang, W.; Du, X.; Wang, H.; Li, N.; Yu, R.; Du, Z.; Wang, J. *RSC Adv.* **2016**, *6*, 76401.
(62)Prlj, A.; Doslic, N.; Corminboeuf, C. *Physical Chemistry Chemical Physics* **2016**, *18*, 11606.
(63)Lenderink, E.; Duppen, K.; Wiersma, D. A. *J. Phys. Chem.* **1995**, *99*, 8972.
(64)Zijlstra, R. W. J.; van Duijnen, P. T.; Feringa, B. L.; Steffen, T.; Duppen, K.; Wiersma, D. A. *J. Phys. Chem. A* **1997**, *101*, 9828.
(65)Zhao, G.-J.; Han, K.-L.; Lei, Y.-B.; Dou, Y.-S. *J. Chem. Phys.* **2007**, *127*, 094307.
(66)Li, Q.; Blancafort, L. *Chem. Commun.* **2013**, *49*, 5966.
(67)Peng, X.-L.; Ruiz-Barragan, S.; Li, Z.-S.; Li, Q.-S.; Blancafort, L. *J. Mater. Chem. C* **2016**, *4*, 2802.
(68)Bolton, O.; Lee, K.; Kim, H.-J.; Lin, K. Y.; Kim, J. *Nat. Chem.* **2011**, *3*, 205.
(69)El−Sayed, M. A. *J. Chem. Phys.* **1963**, *38*, 2834.
(70)Yam, V. W.-W.; Au, V. K.-M.; Leung, S. Y.-L. *Chem. Rev.* **2015**, *115*, 7589.
(71)Yam, V. W.-W.; Cheng, E. C.-C. *Chem. Soc. Rev.* **2008**, *37*, 1806.
(72)Wong, K. M.-C.; Yam, V. W.-W. *Acc. Chem. Res.* **2011**, *44*, 424.
(73)Fermi, E. *Nuclear Physics, Chapter 5*; University of Chicago Press: Chicago, 1950.
(74)Peng, Q.; Yi, Y.; Shuai, Z.; Shao, J. *J. Am. Chem. Soc.* **2007**, *129*, 9333.

(75)Peng, Q.; Yi, Y.; Shuai, Z.; Shao, J. *J. Chem. Phys.* **2007**, *126*, 114302.
(76)Niu, Y.; Peng, Q.; Deng, C.; Gao, X.; Shuai, Z. *J. Phys. Chem. A* **2010**, *114*, 7817.
(77)Wu, Q.; Peng, Q.; Niu, Y.; Gao, X.; Shuai, Z. *J. Chem. Phys. A* **2012**, *116*, 3881.
(78)Zhang, T.; Ma, H.; Niu, Y.; Li, W.; Wang, D.; Peng, Q.; Shuai, Z.; Liang, W. *J. Chem. Phys. C* **2015**, *119*, 5040.
(79)Xie, Y.; Zhang, T.; Li, Z.; Peng, Q.; Yi, Y.; Shuai, Z. *Chem. - Asian J.* **2015**, *10*, 2154.
(80)Zheng, X.; Peng, Q.; Zhu, L.; Xie, Y.; Huang, X.; Shuai, Z. *Nanoscale* **2016**, *8*, 15173.
(81)Lin, S. H.; Chang, C. H.; Liang, K. K.; Chang, R.; Shiu, Y. J.; Zhang, J. M.; Yang, T. S.; Hayashi, M.; Hsu, F. C. In *Adv. Chem. Phys.*; John Wiley & Sons, Inc.: New York, 2002, p 1.
(82)Huang, K.; Rhys, A. *Proc. R. Soc. London, Ser. A* **1950**, *204*, 406.
(83)Kubo, R.; Toyozawa, Y. *Prog. Theor. Phys.* **1955**, *13*, 160.
(84)Bixon, M.; Jortner, J. *J. Chem. Phys.* **1968**, *48*, 715.
(85)Jortner, J.; Bixon, M. *Isr. J. Chem.* **1969**, *7*, 189.
(86)Englman, R.; Jortner, J. *Mol. Phys.* **1970**, *18*, 145.
(87)Lin, S. H. *J. Chem. Phys.* **1970**, *53*, 3766.
(88)Lin, S. H. *J. Chem. Phys.* **1966**, *44*, 3759.
(89)Thompson, M. *MRS Bull.* **2011**, *32*, 694.
(90)Yersin, H. *Highly Efficient OLEDs with Phosphorescent Materials*; WILEY-VCH: Weinheim, 2008.
(91)Zysman-Colman, E. *Iridium(III) in Optoelectronic and Photonics Applications*; John Wiley & Sons Ltd.: Chichester, UK, 2017.
(92)Hofbeck, T.; Yersin, H. *Inorg. Chem.* **2010**, *49*, 9290.
(93)Adachi, C.; Baldo, M. A.; Forrest, S. R.; Thompson, M. E. *Appl. Phys. Lett.* **2000**, *77*, 904.
(94)Sajoto, T.; Djurovich, P. I.; Tamayo, A. B.; Oxgaard, J.; Goddard, W. A.; Thompson, M. E. *J. Am. Chem. Soc.* **2009**, *131*, 9813.
(95)Jansson, E.; Minaev, B.; Schrader, S.; Ågren, H. *Chem. Phys.* **2007**, *333*, 157.
(96)Turro, N. J. *Modern Molecular Photochemistry*; University Science Books: Sausalito, CA, 1991.
(97)Salem, L. *Pure Appl. Chem.* **1973**, *33*, 317.
(98)Rausch, A. F.; Homeier, H. H. H.; Yersin, H. In *Photophysics of Organometallics*; Lees, A. J., Ed.; Springer Berlin Heidelberg: Berlin, Heidelberg, 2010, p 193.
(99)Szabo, A.; Ostlund, N. S. *Modern Quantum Chemistry: Introduction to Advanced Electronic Structure Theory*; Dover Publications Inc.: New York, 1996.
(100)Tamayo, A. B.; Alleyne, B. D.; Djurovich, P. I.; Lamansky, S.; Tsyba, I.; Ho, N. N.; Bau, R.; Thompson, M. E. *J. Am. Chem. Soc.* **2003**, *125*, 7377.
(101)Lamansky, S.; Djurovich, P.; Murphy, D.; Abdel-Razzaq, F.; Lee, H.-E.; Adachi, C.; Burrows, P. E.; Forrest, S. R.; Thompson, M. E. *J. Am. Chem. Soc.* **2001**, *123*, 4304.
(102)Chi, Y.; Chou, P.-T. *Chem. Soc. Rev.* **2010**, *39*, 638.
(103)Li, J.; Djurovich, P. I.; Alleyne, B. D.; Yousufuddin, M.; Ho, N. N.; Thomas, J. C.; Peters, J. C.; Bau, R.; Thompson, M. E. *Inorg. Chem.* **2005**, *44*, 1713.
(104)Rausch, A. F.; Thompson, M. E.; Yersin, H. *J. Phys. Chem. A* **2009**, *113*, 5927.
(105)You, Y.; Huh, H. S.; Kim, K. S.; Lee, S. W.; Kim, D.; Park, S. Y. *Chem. Commun.* **2008**, 3998.
(106)Huang, K.; Wu, H.; Shi, M.; Li, F.; Yi, T.; Huang, C. *Chem. Commun.* **2009**, 1243.
(107)Howarth, A. J.; Patia, R.; Davies, D. L.; Lelj, F.; Wolf, M. O.; Singh, K. *Eur. J. Inorg. Chem.* **2014**, *2014*, 3657.
(108)Parr, R. G.; Yang, W. *Density-Functional Theory of Atoms and Molecules*; Oxford University Press: New York, Oxford, 1989.
(109)Dreuw, A.; Head-Gordon, M. *Chem. Rev.* **2005**, *105*, 4009.
(110)Helgaker, T.; Jorgensen, P.; Olsen, J. *Molecular Electronic-Structure Theory*; Wiley & Sons Ltd.: West Sussex, England, 2014.
(111)Lee, C.; Yang, W.; Parr, R. G. *Phys. Rev. B* **1988**, *37*, 785.
(112)Becke, A. D. *J. Chem. Phys.* **1993**, *98*, 5648.
(113)Grimme, S. *J. Comput. Chem.* **2006**, *27*, 1787.
(114)Zhao, Y.; Truhlar, D. G. *Theor. Chem. Acc.* **2008**, *120*, 215.
(115)Yanai, T.; Tew, D. P.; Handy, N. C. *Chem. Phys. Lett.* **2004**, *393*, 51.
(116)Hehre, W. J.; Ditchfield, R.; Pople, J. A. *J. Chem. Phys.* **1972**, *56*, 2257.

(117)Hariharan, P. C.; Pople, J. A. *Mol. Phys.* **1974**, *27*, 209.
(118)Francl, M. M.; Pietro, W. J.; Hehre, W. J.; Binkley, J. S.; Gordon, M. S.; DeFrees, D. J.; Pople, J. A. *J. Chem. Phys.* **1982**, *77*, 3654.
(119)Clark, T.; Chandrasekhar, J.; Spitznagel, G. W.; Schleyer, P. V. R. *J. Comput. Chem.* **1983**, *4*, 294.
(120)Hay, P. J.; Wadt, W. R. *J. Chem. Phys.* **1985**, *82*, 299.
(121)Niehaus, T. A.; Hofbeck, T.; Yersin, H. *RSC Adv.* **2015**, *5*, 63318.
(122)Martin, R. L. *J. Chem. Phys.* **2003**, *118*, 4775.
(123)Reiher, M.; Wolf, A. *Relativistic Quantum Chemistry*; Wiley-VCH Verlag GmbH & Co. KGaA: Weinheim, 2009.
(124)Lenthe, E. v.; Baerends, E. J.; Snijders, J. G. *J. Chem. Phys.* **1993**, *99*, 4597.
(125)Smith, A. R. G.; Burn, P. L.; Powell, B. J. *ChemPhysChem* **2011**, *12*, 2429.
(126)Lenthe, E. v.; Baerends, E. J.; Snijders, J. G. *J. Chem. Phys.* **1994**, *101*, 9783.
(127)In *ADF2012, SCM, Theoretical Chemistry, Vrije Universiteit, Amsterdam, The Netherlands, http://www.scm.com*.
(128)te Velde, G.; Bickelhaupt, F. M.; Baerends, E. J.; Fonseca Guerra, C.; van Gisbergen, S. J. A.; Snijders, J. G.; Ziegler, T. *J. Comput. Chem.* **2001**, *22*, 931.
(129) http://cvrl.ioo.ucl.ac.uk/cmfs.htm.
(130)Schanda, J. *Colorimetry: Understanding the CIE System*; John Wiley & Sons Inc.: Hoboken, New Jersey, 2007.
(131)Frisch, M. J.; Trucks, G. W.; Schlegel, H. B.; Scuseria, G. E.; Robb, M. A.; Cheeseman, J. R.; Scalmani, G.; Barone, V.; Petersson, G. A.; Nakatsuji, H.; Li, X.; Caricato, M.; Marenich, A. V.; Bloino, J.; Janesko, B. G.; Gomperts, R.; Mennucci, B.; Hratchian, H. P.; Ortiz, J. V.; Izmaylov, A. F.; Sonnenberg, J. L.; Williams; Ding, F.; Lipparini, F.; Egidi, F.; Goings, J.; Peng, B.; Petrone, A.; Henderson, T.; Ranasinghe, D.; Zakrzewski, V. G.; Gao, J.; Rega, N.; Zheng, G.; Liang, W.; Hada, M.; Ehara, M.; Toyota, K.; Fukuda, R.; Hasegawa, J.; Ishida, M.; Nakajima, T.; Honda, Y.; Kitao, O.; Nakai, H.; Vreven, T.; Throssell, K.; Montgomery Jr., J. A.; Peralta, J. E.; Ogliaro, F.; Bearpark, M. J.; Heyd, J. J.; Brothers, E. N.; Kudin, K. N.; Staroverov, V. N.; Keith, T. A.; Kobayashi, R.; Normand, J.; Raghavachari, K.; Rendell, A. P.; Burant, J. C.; Iyengar, S. S.; Tomasi, J.; Cossi, M.; Millam, J. M.; Klene, M.; Adamo, C.; Cammi, R.; Ochterski, J. W.; Martin, R. L.; Morokuma, K.; Farkas, O.; Foresman, J. B.; Fox, D. J. In *Gaussian 09, Revisions B.01 and D. 01*; Gaussian, Inc.: Wallingford, CT, 2009.
(132)Barone, V.; Bloino, J.; Biczysko, M. In *Vibrationally-resolved electronic spectra in GAUSSIAN 09 (accessed april 2017)* http://www.fc.up.pt/pessoas/mjramos/EMTCCM-2016/EMTCCM_MalgorzataBiczysko_3.pdf, 2010.
(133)Duschinsky, F. *Acta Physicochim. URSS* **1937**, *7*, 551.
(134)Sharp, T. E.; Rosenstock, H. M. *J. Chem. Phys.* **1964**, *41*, 3453.
(135)Ruhoff, P. T. *Chem. Phys.* **1994**, *186*, 355.
(136)Mennucci, B.; Cancès, E.; Tomasi, J. *J. Chem. Phys. B* **1997**, *101*, 10506.
(137)Cancès, E.; Mennucci, B.; Tomasi, J. *J. Chem. Phys.* **1997**, *107*, 3032.
(138)Tomasi, J.; Mennucci, B.; Cammi, R. *Chem. Rev.* **2005**, *105*, 2999.
(139)Tsuzuki, S.; Fujii, A. *Phys. Chem. Chem. Phys.* **2008**, *10*, 2584.
(140)Tsuzuki, S. *Annu. Rep. Prog. Chem., Sect. C: Phys. Chem.* **2012**, *108*, 69.
(141)B. Aakeroy, C.; A. Evans, T.; R. Seddon, K.; Palinko, I. *New J. Chem.* **1999**, *23*, 145.
(142)Brammer, L.; Bruton, E. A.; Sherwood, P. *Cryst. Growth & Des.* **2001**, *1*, 277.
(143)Dapprich, S.; Komáromi, I.; Byun, K. S.; Morokuma, K.; Frisch, M. J. *J. Mol. Struct.: THEOCHEM* **1999**, *461–462*, 1.
(144)Vreven, T.; Byun, K. S.; Komáromi, I.; Dapprich, S.; Montgomery, J. A.; Morokuma, K.; Frisch, M. J. *J. Chem. Theory Comput.* **2006**, *2*, 815.
(145)Chen, L.; You, H.; Yang, C.; Ma, D.; Qin, J. *Chem. Commun.* **2007**, 1352.
(146)Fu, H.; Cheng, Y.-M.; Chou, P.-T.; Chi, Y. *Mater. Today* **2011**, *14*, 472.
(147)Alam, P.; Laskar, I. R.; Climent, C.; Casanova, D.; Alemany, P.; Karanam, M.; Choudhury, A. R.; Raymond Butcher, J. *Polyhedron* **2013**, *53*, 286.
(148)Du, B.-S.; Lin, C.-H.; Chi, Y.; Hung, J.-Y.; Chung, M.-W.; Lin, T.-Y.; Lee, G.-H.; Wong, K.-T.; Chou, P.-T.; Hung, W.-Y.; Chiu, H.-C. *Inorg. Chem.* **2010**, *49*, 8713.

(149)Chiu, Y.-C.; Lin, C.-H.; Hung, J.-Y.; Chi, Y.; Cheng, Y.-M.; Wang, K.-W.; Chung, M.-W.; Lee, G.-H.; Chou, P.-T. *Inorg. Chem.* **2009**, *48*, 8164.
(150)Alam, P.; Kaur, G.; Climent, C.; Pasha, S.; Casanova, D.; Alemany, P.; Roy Choudhury, A.; Laskar, I. R. *Dalton Trans.* **2014**, *43*, 16431.
(151)Alam, P.; Das, P.; Climent, C.; Karanam, M.; Casanova, D.; Choudhury, A. R.; Alemany, P.; Jana, N. R.; Laskar, I. R. *J. Mater. Chem. C* **2014**, *2*, 5615.
(152)Alam, P.; Climent, C.; Kaur, G.; Casanova, D.; Roy Choudhury, A.; Gupta, A.; Alemany, P.; Laskar, I. R. *Cryst. Growth Des.* **2016**, *16*, 5738.
(153)Zhang, X.; Chi, Z.; Zhang, Y.; Liu, S.; Xu, J. *J. Mater. Chem. C* **2013**, *1*, 3376.
(154)Ni, J.; Zhang, X.; Qiu, N.; Wu, Y.-H.; Zhang, L.-Y.; Zhang, J.; Chen, Z.-N. *Inorg. Chem.* **2011**, *50*, 9090.
(155)Kishimura, A.; Yamashita, T.; Yamaguchi, K.; Aida, T. *Nat. Mater.* **2005**, *4*, 546.
(156)Sagara, Y.; Kato, T. *Nat. Chem.* **2009**, *1*, 605.
(157)Hou, X.; Ke, C.; Bruns, C. J.; McGonigal, P. R.; Pettman, R. B.; Stoddart, J. F. *Nat. Commun.* **2015**, *6*, 6884.
(158)Albright, T. A.; Burdett, J. K.; Whangbo, M.-H. *Orbital Interactions in Chemistry*; John Wiley & Sons, Ltd: New York, 1985.
(159)Dirac, P. A. M. *Proc. R. Soc. London, Ser. A* **1927**, *114*, 243.
(160)Bixon, M.; Jortner, J. *Electron Transfer: From Isolated Molecules to Biomolecules, Part 1; Advances in Chemical Physics*; John Wiley & Sons, Inc: New York, 1999; Vol. 106.
(161)Jortner, J. *Faraday Discuss.* **1997**, *108*, 1.
(162)Kodama, Y.; Nishihata, K.; Nishio, M.; Nakagawa, N. *Tetrahedron Lett.* **1977**, *18*, 2105.
(163)Nishio, M.; Hirota, M.; Umezawa, Y. *The CH/π Interaction*; Wiley-VCH: New York, 1998.
(164)Janiak, C. *J. Chem. Soc., Dalton Trans.* **2000**, 3885.
(165)Alvarez, S. *Dalton Trans.* **2013**, *42*, 8617.
(166)Lo, K. K.-W. *Acc. Chem. Res.* **2015**, *48*, 2985.
(167)Yeh, Y.-S.; Cheng, Y.-M.; Chou, P.-T.; Lee, G.-H.; Yang, C.-H.; Chi, Y.; Shu, C.-F.; Wang, C.-H. *ChemPhysChem* **2006**, *7*, 2294.
(168)Lo, K. K.-W.; Zhang, K. Y.; Leung, S.-K.; Tang, M.-C. *Angew. Chem., Int. Ed.* **2008**, *47*, 2213.
(169)You, Y.; Han, Y.; Lee, Y.-M.; Park, S. Y.; Nam, W.; Lippard, S. J. *J. Am. Chem. Soc.* **2011**, *133*, 11488.
(170)Ladouceur, S.; Donato, L.; Romain, M.; Mudraboyina, B. P.; Johansen, M. B.; Wisner, J. A.; Zysman-Colman, E. *Dalton Trans.* **2013**, *42*, 8838.
(171)Howarth, A. J.; Davies, D. L.; Lelj, F.; Wolf, M. O.; Patrick, B. O. *Inorg. Chem.* **2014**, *53*, 11882.
(172)You, Y.; Cho, S.; Nam, W. *Inorg. Chem.* **2014**, *53*, 1804.
(173)Zhang, K. Y.; Liu, H.-W.; Tang, M.-C.; Choi, A. W.-T.; Zhu, N.; Wei, X.-G.; Lau, K.-C.; Lo, K. K.-W. *Inorg. Chem.* **2015**, *54*, 6582.
(174)Kumar, S.; Hisamatsu, Y.; Tamaki, Y.; Ishitani, O.; Aoki, S. *Inorg. Chem.* **2016**, *55*, 3829.
(175)Shi, H.; Sun, H.; Yang, H.; Liu, S.; Jenkins, G.; Feng, W.; Li, F.; Zhao, Q.; Liu, B.; Huang, W. *Adv. Funct. Mater.* **2013**, *23*, 3268.
(176)Yoshihara, T.; Murayama, S.; Tobita, S. *Sensors (Basel, Switzerland)* **2015**, *15*, 13503.
(177)Guo, T.; Zhong, W.; Zou, J.; Ying, L.; Yang, W.; Peng, J. *RSC Adv.* **2015**, *5*, 89888.
(178)Song, Z.; Liu, R.; Li, Y.; Shi, H.; Hu, J.; Cai, X.; Zhu, H. *J. Mater. Chem. C* **2016**, *4*, 2553.
(179)Star, A.; Han, T. R.; Joshi, V.; Gabriel, J. C. P.; Grüner, G. *Adv. Mater.* **2004**, *16*, 2049.
(180)Neethirajan, S.; Jayas, D. S.; Sadistap, S. *Food Bioprocess Technol.* **2009**, *2*, 115.
(181)Sasaki, S.; Drummen, G. P. C.; Konishi, G.-i. *J. Mater. Chem. C* **2016**, *4*, 2731.
(182)Dreuw, A.; Head-Gordon, M. *J. Am. Chem. Soc.* **2004**, *126*, 4007.
(183)Boys, S. F.; Bernardi, F. *Mol. Phys.* **1970**, *19*, 553.
(184)Alam, P.; Dash, S.; Climent, C.; Kaur, G.; Choudhury, A. R.; Casanova, D.; Alemany, P.; Chowdhury, R.; Laskar, I. R. *RSC Adv.* **2017**, *7*, 5642.
(185)Lo, K. K.-W.; Choi, A. W.-T.; Law, W. H.-T. *Dalton Trans.* **2012**, *41*, 6021.
(186)Zhao, Q.; Huang, C.; Li, F. *Chem. Soc. Rev.* **2011**, *40*, 2508.
(187)Rappe, A. K.; Casewit, C. J.; Colwell, K. S.; Goddard, W. A.; Skiff, W. M. *J. Am. Chem. Soc.* **1992**, *114*, 10024.